AD-A197 370

Department of AERONAUTICS and ASTRONAUTICS
STANFORD UNIVERSITY

SUMMARY REPORT TO THE
U.S. ARMY RESEARCH OFFICE

FOUNDATIONS OF THE BLADE-VORTEX INTERACTION PROBLEM: STRUCTURE AND BEHAVIOR OF TRAVELLING COMPRESSIBLE VORTICES

FOR THE PERIOD
October 1, 1983 - December 31, 1987

Submitted by

Professor Daniel Bershader

Department of Aeronautics and Astronautics

Stanford University

Stanford, California, 94305

April, 1988

DTIC
ELECT
JUL 1 8 1988
S   D
H

MASTER COPY   –   FOR REPRODUCTION PURPOSES

REPORT DOCUMENTATION PAGE

1a. REPORT SECURITY CLASSIFICATION	1b. RESTRICTIVE MARKINGS
Unclassified	

2a. SECURITY CLASSIFICATION AUTHORITY	3. DISTRIBUTION / AVAILABILITY OF REPORT
	Approved for public release; distribution unlimited.
2b. DECLASSIFICATION / DOWNGRADING SCHEDULE	

4. PERFORMING ORGANIZATION REPORT NUMBER(S)	5. MONITORING ORGANIZATION REPORT NUMBER(S)
	ARO 20670.2-EG

6a. NAME OF PERFORMING ORGANIZATION	6b. OFFICE SYMBOL (If applicable)	7a. NAME OF MONITORING ORGANIZATION
Stanford University		U. S. Army Research Office

6c. ADDRESS (City, State, and ZIP Code)	7b. ADDRESS (City, State, and ZIP Code)
Dept. of Aeronautics and Astronautics Stanford, California 94305	P. O. Box 12211 Research Triangle Park, NC 27709-2211

8a. NAME OF FUNDING / SPONSORING ORGANIZATION	8b. OFFICE SYMBOL (If applicable)	9. PROCUREMENT INSTRUMENT IDENTIFICATION NUMBER
U. S. Army Research Office		DAAG29-83-K-0146

8c. ADDRESS (City, State, and ZIP Code)	10. SOURCE OF FUNDING NUMBERS			
P. O. Box 12211 Research Triangle Park, NC 27709-2211	PROGRAM ELEMENT NO.	PROJECT NO.	TASK NO.	WORK UNIT ACCESSION NO.

11. TITLE (Include Security Classification)
Foundations of the Blade-Vortex Interaction Problem: Structure and Behavior of Travelling Compressible Vortices

12. PERSONAL AUTHOR(S)
Daniel Bershader

13a. TYPE OF REPORT	13b. TIME COVERED	14. DATE OF REPORT (Year, Month, Day)	15. PAGE COUNT
Final	FROM 10/1/83 TO 12/31/87	April, 1988	177

16. SUPPLEMENTARY NOTATION
The view, opinions and/or findings contained in this report are those of the author(s) and should not be construed as an official Department of the Army position, policy, or decision, unless so designated by other documentation.

17.	COSATI CODES		18. SUBJECT TERMS (Continue on reverse if necessary and identify by block number)
FIELD	GROUP	SUB-GROUP	Blade-Vortex Interaction, Rotary-Wing Flight, Rotor Wake, Vortex, Compressible Free Vortex, Fluid Velocity

19. ABSTRACT (Continue on reverse if necessary and identify by block number)

The structure of a compressible free vortex has been analyzed while undergoing convection in a quasi-uniform stream flow. Holographic interferograms reveal radial density profiles of the vortex at different stages of its development during convection. A general mathematical expression is found which closely describes the distribution of density inside the vortex. By use of experimental data and the governing equations in an empirical/theoretical analysis, an extended physical description of the

20. DISTRIBUTION / AVAILABILITY OF ABSTRACT	21. ABSTRACT SECURITY CLASSIFICATION	
☐ UNCLASSIFIED/UNLIMITED ☐ SAME AS RPT. ☐ DTIC USERS	Unclassified	
22a. NAME OF RESPONSIBLE INDIVIDUAL	22b. TELEPHONE (Include Area Code)	22c. OFFICE SYMBOL

DD FORM 1473, 84 MAR   83 APR edition may be used until exhausted.
All other editions are obsolete.

Con't'd

>vortex is developed. The time behavior of the density, determined from the experiments, allows the solution of the Continuity Equation and a distribution of the radial component of fluid velocity relative to the vortex center is obtained. The density information, supplemented by an independent determination of pressure is then used in the Radial Momentum Equation to obtain a distribution of the circumferential component of fluid velocity relative to the vortex center, thus completing the description of the radial dependence of the velocities inside the vortex. Futhermore, the calculated velocities are used to evaluate the magnitudes of the convective and diffusive terms of the Angular Momentum Equation, thus providing insight into the question of the relative effects of *compressibility* and *viscosity* on the internal structure and behavior of the vortex in terms of the distribution and transport of angular momentum. Keywords)

SUMMARY REPORT TO THE
U.S. ARMY RESEARCH OFFICE

FOUNDATIONS OF THE BLADE-VORTEX INTERACTION PROBLEM: STRUCTURE AND BEHAVIOR OF TRAVELLING COMPRESSIBLE VORTICES

FOR THE PERIOD
October 1, 1983 - December 31, 1987

Submitted by

Professor Daniel Bershader

Department of Aeronautics and Astronautics

Stanford University

Stanford, California, 94305

April, 1988

Preface

The blade-vortex interaction is a well-known central feature of rotary-wing flight. The rotor wake contains vorticity because of variations in the bound circulation. Lift and circulation peak near the tip of the rotor blade, and then decrease as the actual tip is approached. The vortex strength there is large, with the result that a strong tip vortex is formed by the roll-up of the sheet of shed vorticity. In forward flight, the vortex filaments are convected in a complex flow field; they take the form of distorted and skewed helices.

Interaction takes place between a rotating blade and the tip vortex from the preceding blade, both in hover and forward flight. The resultant blade loading is known to be the cause of unsteady pressure loading with higher harmonics. In turn, the pressure fluctuation is an important factor in helicopter vibration component fatigue and overall performance; and also in the generation of noise. The latter includes blade slap which is, because of its impulsive nature and high intensity, evidently the most disturbing of the noises radiated by rotary-wing aircraft.

Clearly, the phenomena just described are unsteady and take place typically at transonic flow conditions. Unsteady transonic flows are highly nonlinear, and the equations of motion cannot, in general, be linearized as they can in subsonic and supersonic flows. The complexities of such flows are indicated in the review articles by McCroskey[40] and by Tijdeman and Seebass[41]. A perspective of progress in our understanding of the underlying physical problems and the development of improved investigative methods, both analytical/numerical and experimental, is obtainable from the Summary Notes of the 1984 Workshop on Blade-Vortex Interactions[42].

Recent contributions to the study of BVI problems have been impressive, but difficulties in dovetailing results with suitable quantitative modeling to predict flight performance parameters are still severe. As an alternative and basic approach to a problem of this complexity, the present study isolates a "core" part of the phenomenon, namely the interaction of single, well-defined vortex with a chosen airfoil shape at a given angle of attack and with suitable choice of other parameters, e.g., lateral displacement of the vortex path from the head-on trajectory. A substantial part of the effort to date has been concerned with optimization of the technique to generate a single vortex, detach its

iii

"umbilical," and then have it proceed as a free vortex moving at constant velocity in a quasi-uniform flow toward a "target" airfoil. This experiment, performed in a shock tube, has been fully successful; indeed this now-proven technique offers capability for a variety of related studies. It is quantitative in that the internal structure of the vortex as well as that of the surrounding flow field is determined by a combination of pulsed holographic interferometry and point measurements with a fast-response pressure gauge. By adjusting the time-delay for laser discharge, the time-dependence of both vortex structure and interaction phenomena have been observed -- a necessary feature when dealing with unsteady flows.

Another substantial part of the effort to date has dealt with a detailed study of the structure of the free vortex, a subject which is the central topic of the Ph.D. thesis of research student Michael Mandella. The thesis forms the bulk of the present report.

The work to date has also included preliminary studies of the interaction of these vortices with models of airfoil shapes used in several current helicopters. Some very special features have already been observed, but a systematic study is now in order; it would constitute the logical subject for any follow-on work.

Included at the end of the report is a special addendum dealing with an assessment of recent literature on blade-vortex interactions. References cited in the addendum are included with the latter rather than forming part of the main bibliography.

Abstract

The structure of a compressible free vortex has been analyzed while undergoing convection in a quasi-uniform stream flow. Holographic interferograms reveal radial density profiles of the vortex at different stages of its development during convection. A general mathematical expression is found which closely describes the distribution of density inside the vortex. By use of experimental data and the governing equations in an empirical/theoretical analysis, an extended physical description of the vortex is developed. The time behavior of the density, determined from the experiments, allows the solution of the Continuity Equation and a distribution of the radial component of fluid velocity relative to the vortex center is obtained. The density information, supplemented by an independent determination of pressure is then used in the Radial Momentum Equation to obtain a distribution of the circumferential component of fluid velocity relative to the vortex center, thus completing the description of the radial dependence of the velocities inside the vortex. Futhermore, the calculated velocities are used to evaluate the magnitudes of the convective and diffusive terms of the Angular Momentum Equation, thus providing insight into the question of the relative effects of *compressibility* and *viscosity* on the internal structure and behavior of the vortex in terms of the distribution and transport of angular momentum.

Contents

List of Tables

List of Figures

Chapter 1

Introduction

"Of the eddies one is slower at the center than on the sides, another is swifter at the center than on the sides; others there are which turn back in the opposite direction to their first movement" *Leonardo Da Vinci*

Da Vinci's descriptions of the vortices he had observed in water reflect man's fascination from earliest times of the beauty and power of spinning and swirling vortex motions. Images of spirals are found in artworks dating back over thousands of years, perhaps inspired by the vigorous whirlpools found in streams or the violent eddies seen in flames. Vortices appear in nature on every scale starting from the spinning charge of the electron, to bathtub vortices, to tornadoes and hurricanes in the atmosphere, and finally to the rotating clusters of galaxies in the universe. Given the value of 2.8 femtometers for the classical electron radius [1] and 10 million light-years for the radius of a galaxy cluster [2], it can be said that vortex motion occurs over a range of 38 orders of magnitude. It is interesting to note that one's introductory approach to motion, as founded by Galileo and quantified by Newton's famous three laws, is based on straight-line motion, which is not observed in nature over such an incredible range of scales as vortex motion. A special case of vortex behavior is the subject of the present study.

1.1   Orientation

The study of vortices has been a central component of basic and applied research in fluid dynamics, and vortex theory forms part of the classical core of the subject. Of the many facets of this discipline, those of particular interest to aerodynamicists are the generation of vortices by aeronautical surfaces and the interaction of vortices with such surfaces. The former phenomenon has played an increasingly significant role as part of the three-dimensional flow field around flight vehicles at high angles of attack. The latter, on the other hand, is a principle feature of rotary-wing aircraft, where it is often referred to as the vortex-airfoil or blade-vortex interaction (BVI). It is this problem which has stimulated the present research. Better understanding of the phenomenon is especially motivated by the desire to reduce the noise generated as well as the transient pressure loading produced by the BVI.

The subject of vortex interactions is inherently a very complex one, and one that is further exacerbated by the fact that blade-tip speeds of current rotary-wing aircraft lie in the transonic range. Thus, *compressibility effects* must be considered in any realistic study. Most of the analytic work to date has ignored the effects of compressibility (see Lugt [3] for a historical perspective). The same is true of most of the experimental work reported in the literature.

In practical vortex interaction situations, the vortices are distorted and the vorticity is partially randomized soon after generation by the surrounding non-uniform wake. Of course, that behavior increases the complexity of the subsequent interaction. How, then, should one formulate a systematic research program to explore the basic nature of the BVI? The logical answer is to model the phenomenon by studying the interaction of a single vortex with a chosen airfoil surface under well-defined conditions. Here, we adopted an experimental approach by designing a suitable facility in which to perform such studies.

The experimental arrangement, described further in Chapter 2, produced the desired interaction by generation of a single vortex which was then convected by

a quasi-uniform 2-D compressible flow toward an airfoil model (Mandella and Bershader [4],[5]). The flow was energized by a traveling shock, with the vortex generation and interaction taking place in a test section specially designed for appropriate experimental diagnostics, including holographic interferometry. The early experiments (see Figures 1.1→1.4) confirmed that the density configuration of the vortex itself could be determined with considerable precision (later, non-optical diagnostics were employed to obtain an independent determination of the radial pressure distribution across the vortex). It was then decided that a necessary first step in the vortex-interaction study should consist of an extended analysis of the structure and behavior of the free-moving (convecting) vortex prior to interaction.

The Present Study

The objective of this thesis, then, is the measurement and calculation of the various physical properties associated with the compressible free vortex during its *convection stage* inside a special shock tube arrangement. The accomplishment of this objective is done in several stages:

1. A special test section which contains the *vortex generator* is constructed and attached to the open end of a shock tube. A compressible flow, which is provided by the shock tube, enters the test section and a free, two-dimensional, transverse vortex is generated by the arrangement. The vortex travels with the flow between large optical windows for a sufficient period of time to allow optical measurements to be made.

2. A double-pulsed laser holographic interferometric system is set up along with appropriate electronic timing and synchronization circuits for making interferograms of the vortex flow. The interferograms, when evaluated, provide quantitative density information about the vortex.

3. A pressure measurement technique is used to gain additional quantitaive information about the vortex, independent of the density measurements.

4. A numerical procedure for curve fitting of the density and pressure data is used to generalize the quantitative density and pressure information into empirical relationships.

5. Using the combination of experimentally derived empirical laws and the appropriate equations of motion, calculations reveal other physical properties of the vortex.

Figure 1.1: Interferograms Showing Generation of Vortex.

Sequence of four interferograms in the location of the generating airfoil taken at 20 micro-sec intervals during the *vortex generation stage* as the shock travels from left to right over the airfoil.

Figure 1.2: Interferogram Showing Vortex During the Convection Stage.

This wide field-of-view interferogram shows the whole flow field during the *vortex convection stage*. The generating airfoil and the target airfoil (for vortex-airfoil interaction studies) are both visible. The *age* of the vortex is $\approx$ 275 micro-sec and is traveling at $\approx$ 180 m/sec behind the Mach $\approx$ 1.4 shock. The vortex diameter is $\approx$ 1 cm.

Figure 1.3: Close-up Interferogram Showing Vortex Structure.

This is a close-up of the vortex in Figure 1.2, the dark lines represent *density contours* which indicate a density change of $\approx 1/20$ of atmospheric density from one contour to the next. The vortex is highly evacuated in the center (factor of ≈ 3 change from the ambient density surrounding vortex to the center). The contour lines closely resemble a system of concentric circles. This symmetry is utilized both in the analytic modeling of the vortex and in the search for empirical functions to fit the data.

Figure 1.4: Interferograms Showing Vortex-Blade Interaction.

Sequence of four interferograms taken at 25 micro-sec intervals during the *vortex interaction stage*. Rotation in the incident vortex is counterclockwise. As the vortex approaches the airfoil, there is an upward component of velocity across the airfoil nose, i.e., perpendicular to the chord of the airfoil. As a result, a secondary vortex is produced having clockwise rotation. There is a complex interaction between these two counter-rotating vortices and the surface of·the airfoil. Note: in the last frame, acoustic waves can be seen emanating from the interaction point.

1.2 Background

1.2.1 Theory of the 2-D Axisymmetric Compressible Free Vortex

The most striking, immediate observation of the free vortex (see Figure 1.3), is the remarkable symmetry about its axis. The density contour lines appear to closely resemble a system of concentric circles. It can also be observed that the vortex travels at a constant speed along a linear path during this *convection stage* (see Figure 1.2). Under these conditions the vortex motion can be described within an inertial frame with respect to the laboratory system and a Galilean transformation may be applied to the equations of motion. The vortex flow can thus be described by the Navier-Stokes equations in a reference frame that is stationary with respect to the center of the vortex. With the additional assumptions that the vortex is two-dimensional and axisymmetric (all physical quantities depend only on time t and the distance r from the axis), then the Navier-Stokes equations may take a form in a cylindrical coordinate system having the origin at the vortex center. Beginning with the general form in cylindrical coordinates as given by Thompson [6], the equations may be written in the following form:

$$Continuity:$$

$$\frac{\partial \rho}{\partial t} + \underbrace{\frac{1}{r}\frac{\partial}{\partial r}(r\rho v_r)}_{\substack{divergence \\ of\ mass\ flux}} = 0 \tag{1.1}$$

Radial Momentum :

$$\underbrace{\frac{\partial v_r}{\partial t}}_{\substack{\text{local} \\ \text{(unsteady)} \\ \text{acceleration}}} + \underbrace{v_r \frac{\partial v_r}{\partial r}}_{\substack{\text{convective} \\ \text{acceleration}}} + \underbrace{\frac{1}{\rho}\frac{\partial P}{\partial r}}_{\substack{\text{specific} \\ \text{pressure} \\ \text{force}}} - \underbrace{\frac{v_\phi^2}{r}}_{\substack{\text{centripetal} \\ \text{acceleration}}}$$

$$- \underbrace{\frac{2}{\rho}\left(\frac{\partial}{\partial r}\mu\frac{\partial v_r}{\partial r} + \frac{\mu}{r}\frac{\partial v_r}{\partial r} - \mu\frac{v_r}{r^2}\right)}_{\substack{\text{specific radial force} \\ \text{due to normal stress}}} = 0 \tag{1.2}$$

Angular Momentum :

$$\underbrace{\rho r^2 \frac{\partial}{\partial t}\left(\frac{v_\phi}{r}\right)}_{\substack{\text{local rate} \\ \text{of change of} \\ \text{angular momentum/vol.}}} + \underbrace{\rho v_r \frac{\partial}{\partial r}(r v_\phi)}_{\substack{\text{radial convection} \\ \text{of angular momentum/vol.}}}$$

$$- \underbrace{\frac{1}{r}\frac{\partial}{\partial r}\left[r^3\mu\frac{\partial}{\partial r}\left(\frac{v_\phi}{r}\right)\right]}_{\substack{\text{viscous torque/vol.} \\ \text{due to shear stress}}} = 0 \tag{1.3}$$

Energy :

$$\underbrace{\frac{\partial}{\partial t}\left[\rho\left(\frac{v_r^2 + v_\phi^2}{2} + c_v T\right)\right]}_{\substack{\text{local rate of change} \\ \text{of energy/vol.}}}$$

$$+ \underbrace{\frac{1}{r}\frac{\partial}{\partial r}\left[r\rho v_r\left(\frac{v_r^2 + v_\phi^2}{2} + c_p T\right)\right]}_{\text{rate of energy convection/vol.}}$$

$$+ \underbrace{\frac{1}{r}\frac{\partial}{\partial r}\left(kr\frac{\partial T}{\partial r}\right)}_{\substack{\text{divergence of} \\ \text{heat flux}}} + \underbrace{\frac{1}{r}\frac{\partial}{\partial r}\left[v_\phi r^2\mu\frac{\partial}{\partial r}\left(\frac{v_\phi}{r}\right)\right]}_{\substack{\text{rate of work/vol.} \\ \text{by shear stress}}} = 0 \, . \tag{1.4}$$

These governing equations include the effects of viscosity, compressibility and heat conduction. Physical interpretations of the various terms have been provided beneath each term. In this coordinate system, the velocity is separated

into two time-dependent components. These are the radial and circumferencial components given by v_r and v_ϕ respectively. The time-dependent quantities ρ, P, T, k and μ are also dependent on the coordinate r which is the radial distance from the center of the vortex. The system of equations is completed by the *Equation of State* for a perfect gas

$$P = \rho RT \tag{1.5}$$

where R is the gas constant per unit mass.

1.3   Review of Previous Work

In the next two sections, the history of the development of special vortex models from the governing equations given in Section 1.2.1 is outlined, followed by a history of previous experimental work in this area.

1.3.1   Previous Theoretical Work

Vortices occur in a wide variety of conditions. There has been a great deal of practical interest in the vortices that are produced in flows past bodies. These vortices generally involve a large-scale flow field surrounding a central core region that is three-dimensional in nature [7]. The three-dimensional vortices studied by Hall [8] and solved by numerical integration methods, have an appreciable axial component of motion and there is an interaction between the axial and circumferential components of velocity. This axial motion, and the wide range of possible core structures, distinguish the three-dimensional vortex from the two-dimensional case. Another study [9] reported a special inviscid case where the Navier-Stokes equations for a steady three-dimensional conical vortex could be transformed into those for an unsteady two-dimensional vortex flow, and thus a correspondence is found between *three-dimensional*

cores growing in space and *two-dimensional cores growing in time*. This conically symmetric solution of the Eulerian equations of an incompressible fluid was thought to be descriptive of the flow properties of leading-edge vortices which are observed in flows over slender delta wings. Brown [10] presented an extension of Hall's theory to include the effects of compressibility. The results of this study indicated that the only solutions acceptable on physical grounds have vanishing density on the axis. The corresponding two-dimensional time-dependent flow (two-dimensional self-similar core growing in time) was observed in a shock tube by Howard and Matthews [11] by passing a shock over a vertical wedge. A system of 2-D axisymmetric self-similar isentropic equations were assumed valid in describing an inviscid outer core region of the vortex. Interferograms were made of the vortex at different times during the growth period and the numerical solutions obtained were found to be in good agreement with the experiment. Merzkirch [12] treated the same 2-D problem using the equations in Section 1.2.1 along with the additional assumption of self-similar behavior and found a solution for the inner viscous core. Unfortunately, these similarity solutions inherently describe a vortex core growing in size and are not consistent with experimental observations of free compressible vortices. In 1948, Burgers [13] found a closed-form solution of a steady-state 3-D axisymmetric incompressible viscous vortex. Burger's steady vortex has an inward radial convection of angular momentum which just balances the outward diffusion. To preserve continuity in this incompressible vortex, there is an axial flow moving fluid out at the same rate as it is brought into the vortex by the inward radial flow. In 1958, a general time-dependent closed-form solution of this vortex was discovered by Rott [14] which describes the unsteady development of a vortex flow into the final steady configuration given by Burgers. Rott also investigated the temperature profile of this vortex [15]. Even though compressibility has been largely ignored, the information provided by these 3-D and 2-D studies is useful for developing some basic generalizations that distinguish the 3-D vortex from the 2-D vortex under various conditions and lead to the conclusion that a study of

the effects of compressibility should begin with the simpler two-dimensional case. This discussion will continue with a review of previous work done on the two-dimensional vortex as described by the equations in Section 1.2.1.

In general, solutions of the basic equations in Section 1.2.1 can be found only by numerical integration. Some closed-form solutions of these 2-D equations exist in a limited number of special cases which give information on the characteristics of vortices. The system of equations in Section 1.2.1 involve seven quantities (v_r, v_ϕ, ρ, P, T, k and μ) which in a real gas are all functions of r and t. The most common method of dealing with this problem is to assume that some of the quantities have constant values independent of r and/or t. This approach gives information on some special types of vortices with varying degrees of *compressibility*, *viscosity* and *real gas effects*.

Incompressible Inviscid vortex

The compressibility may be neglected by setting $\rho = constant$ and $v_r = 0$. By also neglecting the radial dependence of viscosity ($\mu = constant$) and assuming steady-state conditions, Equation 1.3 can be put into the form:

$$\frac{\partial}{\partial r}\left[r^3 \frac{\partial}{\partial r}\left(\frac{v_\phi}{r}\right)\right] = 0 \ .$$

Note that under the assumptions given in this model, the solution

$$v_\phi = \frac{a}{r} + br \ ,$$

with a and b constant and determined by the boundary conditions, is completely independent of the viscosity. On the axis, the boundary condition $v_\phi(r = 0) = 0$ is required by the symmetry of the problem. Another boundary condition $v_\phi(r = \infty) = 0$ may be used. For $a = 0$ this solution describes a solid body rotation which satisfies the boundary condition on the axis and for which b is the angular velocity. For $b = 0$ this solution represents the *potential vortex*

$$v_\phi = \frac{K}{r} \ ,$$

where $a = K$, with K being the vortex strength which is related to the circulation Γ by

$$\Gamma = 2\pi K \ .$$

For the potential vortex, the flow is irrotational except for a singularity at the origin; i.e.,

$$\nabla \times v = 0 \ .$$

The two solutions can be combined to describe a potential vortex that is modified near the axis, i.e., a potential vortex which has a solid body core. The velocity increases linearly from zero at the center to a maximum value $v_{\phi\,peak}$ (where the solid body rotation ends and where the potential velocity field begins).

Under the same assumptions, Equation 1.2 becomes:

$$\frac{\partial P}{\partial r} = \frac{\rho v_\phi^2}{r} \ ,$$

with ρ being a constant. Substituting $\frac{K}{r}$ for v_ϕ gives:

$$\frac{\partial P}{\partial r} = \frac{\rho K^2}{r^3} \ .$$

Integrating [16], gives:

$$P(r) = P_\infty - \frac{1}{2}\frac{\rho K^2}{r^2} \ ,$$

where P_∞ is the pressure at $r = \infty$. This describes the pressure field of the potential vortex outside of the core region.

Incompressible Viscous Vortex

In 1918, G. I. Taylor [17] found a time-dependent closed form solution of Equation 1.3 by assuming

$$v_r = 0$$

and

$$\frac{\mu}{\rho} = \nu \ ,$$

where $\nu = constant$ (dynamic viscosity), thereby treating the problem as incompressible, and ignoring the radial dependence of μ. The solution for v_ϕ reveals the effects of viscous dissipation and is given by

$$v_\phi = \frac{mr}{4\pi\nu t^2}e^{-\frac{r^2}{4\nu t}} \, ,$$

where m is a constant which, multiplied by ρ, represents the angular momentum

$$\int_0^\infty 2\pi\rho r\, v_\phi\, r\, dr = \rho m \, .$$

This model describes a vortex which is decaying with time t and has a finite total kinetic energy and energy dissipation. Near the axis the vortex behaves like a solid body where the circumferential velocity increases linearly with radial distance

$$v_\phi = \frac{mr}{4\pi\nu t^2} \, ,$$

and reaches a maximum value $v_{\phi\,peak}$ at $r = r_c$. The temporal behavior of this vortex is basically a dying down and spreading out of the core under the influence of viscosity. The core radius r_c increases with time as the peak velocity $v_{\phi\,peak}$ decreases with time. The vortex can be said to *increase in size and grow weaker in strength*. Such behavior is not precisely what is observed in the present experimental study of compressible vortices. The compressible vortices in this study do not appreciably increase in size as they grow weaker in strength (see Chapter 3 *Results*).

A similar type of solution is given by Lamb [18] which has some different properties. Lamb's solution is given by

$$v_\phi = \frac{K}{r}\left(1 - e^{-\frac{r^2}{4\nu t}}\right) \, ,$$

where K is the strength of the vortex. Lamb's vortex has the same characteristic solid body core, but the velocity decay with increasing radial distance is weaker than that of Taylor's vortex, approaching that of the potential vortex and thereby resulting in an infinite kinetic energy, angular momentum and energy dissipation in an unbounded flow region.

Compressible Inviscid Vortex

If the vortex is considered inviscid, then there are no entropy gradients and the flow will be homentropic. In 1930, G. I. Taylor [19] considered the problem of an isentropic potential vortex. Beginning with the $1/r$ velocity field of the potential vortex, and the given condition that the streamlines are circles, then in each circle there is the same circulation $2\pi K$. Suppose q represents the speed at radius r then

$$r = \frac{K}{q} .$$

Taylor then uses the isentropic relation

$$q = \left[\frac{1}{M^2} + \frac{1}{2}(\gamma - 1)\right]^{-\frac{1}{2}} ,$$

so that

$$r = K \left[\frac{1}{M^2} + \frac{1}{2}(\gamma - 1)\right]^{\frac{1}{2}} ;$$

and r will have a minimum value r_{min} when $M = \infty$ given by

$$r_{min} = K \left[\frac{1}{2}(\gamma - 1)\right]^{\frac{1}{2}} .$$

The ratio r/r_{min} is given by

$$\frac{r}{r_{min}} = \left[1 + \frac{2}{(\gamma - 1) M^2}\right]^{\frac{1}{2}} ,$$

a relation which reveals some interesting features. Note first the existence of a *minimum radius* where the Mach number of the flow becomes infinite. At any radius smaller than r_{min} there could not be any fluid, which describes an empty core. There is also a value of r where $M = 1$ and thus where the vortex becomes supersonic. By setting $M = 1$, the radius of the sonic circle is given by

$$r_{sonic} = r_{min} \left[\frac{\gamma + 1}{\gamma - 1}\right]^{\frac{1}{2}} .$$

This vortex has three regions. In the central region lies the empty core which has a radius given by r_{min}. The annular region between r_{min} and r_{sonic} contains the supersonic flow. The flow is subsonic everywhere outside of the sonic circle.

Compressible Viscous Heat-Conducting Vortex

In 1960, L. M. Mack [20] attempted to answer the question of whether or not an *isentropic vortex* is possible in a real gas. Mack used the model of a vortex that is driven by a circular cylinder rotating in a compressible viscous heat-conducting fluid of infinite extent initially at rest. This vortex is to be distinguished from a *free vortex*, i.e., one driven by a radial flow carrying angular momentum inward. Under these steady-state conditions there exists temperature, pressure and density variations across the vortex which are dependent on the rotational speed of the driving cylinder. At a low rotational speed the temperature variation across the vortex is small and the viscosity coefficient is assumed constant. At higher rotational speeds of the driving cylinder the temperature variation across the vortex is large and the temperature dependence of the viscosity coefficient is taken into account.

In this treatment $v_r = 0$ and $\partial \rho / \partial t = 0$, so the Continuity Equation (see Equation 1.1) cannot be used. The Radial Momentum Equation (see Equation 1.2) becomes

$$\frac{\partial P}{\partial r} = \frac{\rho v_\phi^2}{r} ,$$

which shows the pressure gradient providing the required centripetal force. The Angular Momentum Equation (see Equation 1.3) becomes

$$\frac{\partial}{\partial r} \left[r^3 \mu \frac{\partial}{\partial r} \left(\frac{v_\phi}{r} \right) \right] = 0 ,$$

where the coefficient of viscosity μ is dependent on r. It can be seen from this equation that when μ varies along the radius, an *irrotational* solution is no longer possible. The shear stress is

$$\tau = \mu r \frac{\partial}{\partial r} \left(\frac{v_\phi}{r} \right) ;$$

and the Energy Equation (see Equation 1.4) becomes

$$\frac{\partial}{\partial r} \left[kr \frac{\partial T}{\partial r} + \mu r^2 v_\phi \frac{\partial}{\partial r} \left(\frac{v_\phi}{r} \right) \right] = 0 ,$$

where T is the temperature and k is the coefficient of thermal conductivity. k also is a function of the temperature and therefore is dependent on r. This equation relates the *work done by the shear stress* and the *heat transferred by conduction*. In general. an amount of heat must be withdrawn per second just equal to the power required to maintain the flow in this steady-state process. Mack solves these equations by a numerical integration method using the Sutherland viscosity law [21] to model the radial dependence of μ. The calculations show that under these conditions the vortex is not irrotational and is not isentropic.

Summary of Models

The theoretical models reviewed in this section comprise the bulk of that aspect of vortex theory which addresses the question of the *internal structure* of the vortex. Each model has contributed new information on the internal characteristics of vortices under different combinations of special conditions. The 2-D models are of special interest because of their relative simplicity compared to the 3-D case. In these simpler models the internal structure and general behavior of the vortex are revealed. These models were discussed in chronological order of their development and are listed below:

- Incompressible Inviscid Vortex (Steady).

- Incompressible Viscous Vortex (UnSteady).

- Compressible Inviscid Vortex (Steady).

- *Driven* Compressible Viscous Heat-Conducting Vortex (Steady).

This set of models is extended by this Thesis which investigates the following case:

- *Free* Compressible Viscous Heat-Conducting Vortex (Unsteady).

1.3.2   Previous Experimental Work

The theory of unsteady motion around two-dimensional airfoils developed by Von Karman and Sears [22] predicts the existence of a *starting vortex* which develops as the airfoil is put into motion. The vortex subsequently separates from the airfoil, carrying angular momentum away and leaving a net circulation around the airfoil, which creates lift. Hollingsworth and Richards (1955 [23]) utilized this idea as a method of generating 2-D free compressible vortices in a study of vortex-shock interactions. The vortex was generated in a rectangular shock tube which had optical windows mounted along the walls of the tube to preserve the two-dimensional nature of the flow and provide optical access for flow visualization. A starting vortex is generated as the shock wave passes over an airfoil which is set at incidence between the inside walls of the shock tube. As the fully developed vortex moves away from the trailing edge of the airfoil with the velocity of the free stream, the shock wave is then reflected from a plane wall at the far end of the tube, and moves back towards the approaching vortex. The resultant vortex-shock interaction is viewed by a conventional twin-mirror Schlieren system, utilizing a spark discharge in air as the light source. The photographic results reveal a system of reflected and diffracted waves (and their respective triple points) which emanate from the vertices of the airfoil and which can be traced throughout the remainder of the flow. Also, a system of slipstreams are seen which emanate from the triple points and roll up into the vortex. This multiply-reflected weak shock system does not appear to affect the vortex. The photographs very clearly show an acoustic wave emanating from the interaction of the vortex with the strong back-reflected shock. A theoretically derived distribution of intensity in the sound wave resulting from the interaction between a vortex and a shock wave is compared with a Schlieren photograph in a follow-up study [24]. Unfortunately, the Schlieren photographs in these studies do not reveal anything quantitative about the structure of the vortex and its core. Dosanjh and Weeks (1965 [25]) extended this study by using the same type of shock

tube arrangement for the vortex generation and interaction, but used a Mach-Zehnder interferometer to record the flow field. The interferograms provide quantitative information about the spatial density distribution of the vortex at different times during the flow. Since the vortex is observed to be convected at almost the free stream velocity, and since there is no drift flow behind the returning reflected shock, the translational motion of the vortex is halted after the interaction with the shock. This stationary position of the vortex with respect to the laboratory made it very convenient for a study of the decay behavior since it was always in the field-of-view of the interferometer. The slipstreams that were identified by Hollingsworth and Richards were observed by Dosanjh and Weeks to exhibit self-similar behavior for an extended period of time. The vortex itself decays to the point of vanishing after 3 milli-sec. The vortex flow field was examined for several values of delay time both before and after the interaction with the shock. Both the core-center density behavior with time and the spatial density distribution of the vortex at several different times were plotted. The temporal behavior of the vortex was modeled and a calculation of the circulation Γ was achieved by use of a combination of incompressible and compressible models. Lamb's case of an incompressible viscous circular vortex

$$v_\phi = \frac{K}{r}\left(1 - e^{-\frac{r^2}{4\nu t}}\right)$$

was used as an approximation to the circumferential velocity distribution; and v_ϕ (defined as above) was then substituted into the viscous compressible form of the Radial Momentum Equation

$$\frac{\partial P}{\partial r} = \frac{\rho v_\phi^2}{r}$$

to yield a relationship between the density ρ and vortex strength K. An additional assumption of polytropic behavior in the radial direction

$$P = c\rho^\gamma$$

is used to complete the set of equations. After integration of the equations, the resulting expression had three free parameters: a time reference t_o, γ and a

third parameter which is a function of the vortex strength K. The expression was plotted and compared with the experimental density data in order to deduce values of the parameters for a best-fit. It was found that γ was very nearly equal to 1.4 and the circulation Γ was found to be around 3 m^2/sec with the airfoil set at 12.5 degrees incidence and a shock strength of $P_2/P_1 = 2$.

Using this same method of vortex generation in a shock tube, Meier (1984 [26]) studied the *transonic* interaction of a similar shock-generated *starting vortex* with a second airfoil placed downstream. A Mach-Zehnder interferometer was used to record the flow field at several different times both during the vortex convection period and the subsequent interaction period. A most significant result from Meier's experiments was the visualization of an acoustic wave which emanated from the interaction. Although there was no detailed study of the vortex structure itself, follow-up studies (Timm 1985 [27] and Lent 1986 [28]) using Meier's apparatus, examined the acoustic fields and the vortex trajectories associated with the vortex-airfoil interactions.

The experimental program of this Thesis utilizes this same basic method of generating a single free compressible vortex inside a shock tube at the Stanford High Pressure Shock Tube Laboratory (Mandella and Bershader 1984 [29]). This study uses an open ended shock tube with an enlarged test section designed to minimize reflected shocks back into the flow. Large acrylic windows are used to maximize optical access to the flow and a holographic interferometric technique is used to record *instantaneous* (10 nano-sec) interferograms of the flow at different delay times. The density information provided by the holograms is also supplemented by pressure measurements made on the side walls of the test section along the vortex path.

1.4   Outline of Thesis

In Chapter 2, the experiments are described. A general description of the experimental apparatus, procedures and reduction of data is given. More detailed information is given in the various appendices.

In Chapter 3, a general description of the experimental results (including some illustrative samples from the complete data set) is given and discussed. The complete data set and error analysis is located in the appendices.

In Chapter 4, a detailed analysis is given for the free compressible vortex utilizing both the equations of motion and the experimental results. Various physical properties of free compressible vortices under the test conditions are calculated (including temperature and velocity profiles). The distribution and transport of angular momentum inside the vortex, and the competing processes of diffusion and convection in the compressible vortex are investigated in order to gain insight into the roles of viscosity and compressibility.

In Chapter 5, the conclusions of the combined experimental and analytic study are summarized, including a discussion of the roles of the viscosity and the compressibilty in the problem. Also, suggestions for further research are given.

Chapter 2

Experiments

The primary measurement technique used in the present study is the method of *Double Pulsed Holographic Interferometry* [30] *applied to the shock-generated* flow field. One obtains in this case (2-D flow) a fringe pattern representing a series of density contour lines. This form of data not only provides a means of visualizing the flow, but also provides quantitative global information about the whole density field of the flow. The light source is provided by a ruby laser with a 10 nano-sec pulse duration; thus, each exposure constitutes an instantaneous *snapshot*. A special test section was designed which utilizes the flow emerging from the end of a rectangular shock tube. The test section preserves the two-dimensional nature of the flow with the placement of two opposing large acrylic windows which serve as extensions of the shock tube walls. The vortex generator consists of an airfoil mounted between the windows at a large angle of attack; it produces a starting vortex resulting from passage of the shock. Each time the shock tube is fired, an interferogram is made of the flow at some predetermined time. The technique of repeated experiments, with sequential advance of time delays for firing the laser, provides a time history of the different stages of development of the flow. This technique requires a timing system for synchronizing the laser pulse with specific flow

23

events and for monitoring the shock speed (which indicates the repeatability of the experiments). Supplementary (non-optical) measurements of the vortex pressure are also made. The density and pressure data are then evaluated and presented in the form of radial distributions through the vortex center. This chapter will give a general description of the experimental apparatus, procedures and data reduction. More detailed information is contained in the appendices.

2.1   Apparatus

2.1.1   Shock Tube and Test Section

The studies were performed with a conventional shock tube arrangement modified by an enlarged test section at the downstream end which is open to the atmosphere. The shock tube and test section have a rectilinear cross section designed to produce a two-dimensional flow. Figure 2.1 shows a sectional view of the test section and the portion of the shock tube to which it is attached (the driver section is not shown). Appendix A contains a complete description of the shock tube and the experimental operating conditions. The dimensions in Figure 2.1 are given in centimeters (cm).

Shock Tube

The shock tube has a square cross section of 5 cm on a side. The full length between the driver section and the test section is 6 m (meters). This configuration delivers a uniform flow of air behind a Mach 2 shock for a duration of ≈ 5 milli-sec (see Appendix A). A specially prescribed aluminium diaphram separates the pressurized driver section from the rest of the shock tube (which is open to the atmosphere). The driver section is 1.8 m long. The shock is initiated when a sufficient pressure difference bursts the diaphram. The shock
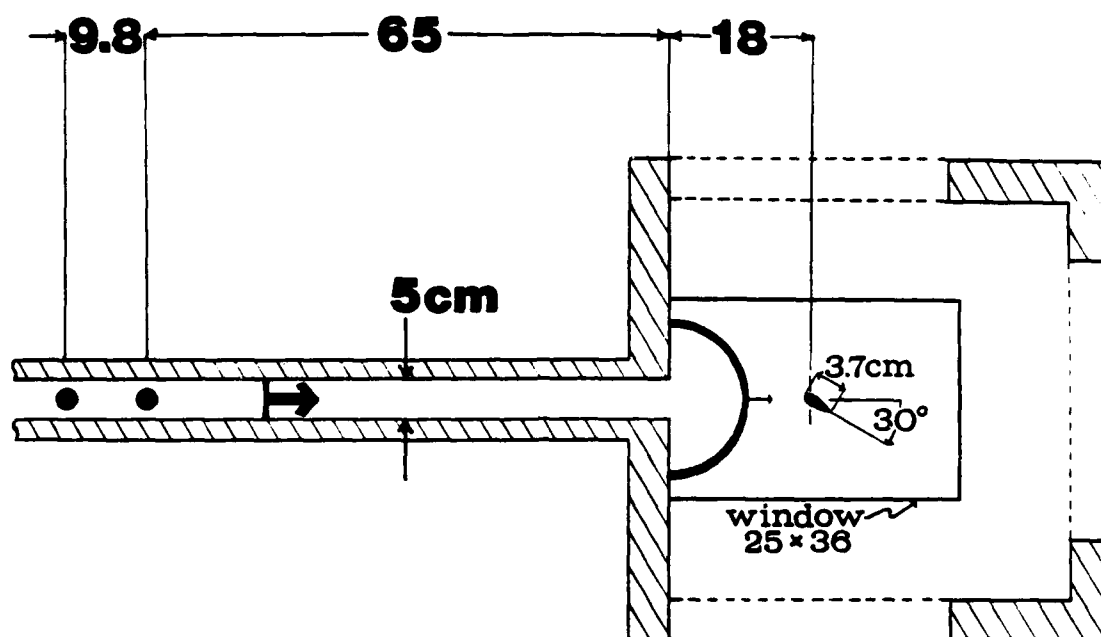
Figure 2.1: Shock Tube and Test Section.

then travels down the tube into the test section. In Figure 2.1 the shock is represented by a heavy straight line with an attached arrow showing the direction of travel. In these experiments the downsteam pressure was atmospheric; under these conditions the shock front is highly planar before entering the test (expansion) section.

Test Section

The test section has a rectangular cross section which allows the shock to diffract only in a cylindrical fashion, as illustrated by the heavy curved line in Figure 2.1; thus, the 2-D feature of the flow-field is retained. Also shown in Figure 2.1 is the 25 cm × 36 cm opening for the insertion of acrylic windows which are mounted parallel to each other on opposite sides of the test section. The inside surface of each window is flush with the inside surface of the shock tube, thus providing for a two-dimensional flow configuration. The windows permit optical access over a rather sizable region of the flow field. Two

additional opposing sets of small windows (shown in Figure 2.1 as darkened circles) are mounted into the shock tube walls about 65 cm upstream from the area-change station. These small windows permit shock *time-of-flight* measurements to be made with the aid of two laser beams and suitable optical detectors. Shock passage deflects each laser beam in turn. A microsecond counter is used to record the interval of time between the two signals from the detectors. Given the knowledge of the precise distance between the two beams (9.8 cm), this type of measurement yields the shock velocity, which is used to calculate other properties of the flow behind the shock (see Appendix A). The second of these signals is also used to start a timing sequence which fires a ruby laser at a predetermined delay time for the purpose of recording a hologram of the flow in the test section. The test section as shown in Figure 2.1 is integral to the shock tube and is open to the atmosphere by way of the top, bottom and end ports identified by the dashed lines. These ports allow the expanding shock and flow to continue into the laboratory room and thereby eliminate a major portion of shock reflections back into the test section.

Vortex Generator

A NACA 0018 airfoil is mounted between the two large acrylic windows of the test section 18 cm downstream of the shock tube end. The expanding shock passes over this airfoil and generates a vortex. This airfoil is mounted such that its quarter-chord-point (identified by Von Karman and Sears [22] as the center-of-lift of the airfoil) is positioned along the centerline of the flow. It is held in position by means of 1/16 inch diameter alignment pins and corresponding holes which are drilled into the windows and the airfoil. Additional sets of pins and holes are used to keep the airfoil in a fixed inclination of 30 degrees as shown in Figure 2.1.
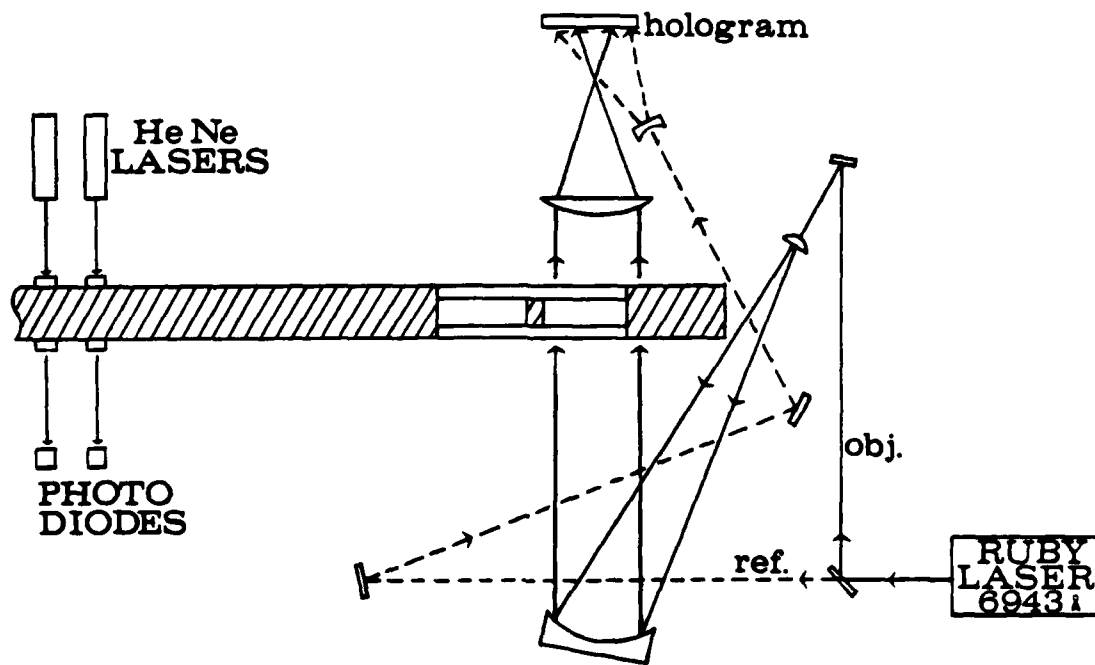
Figure 2.2: Optical Arrangement for Double Pulsed Holographic Interferometry.

2.1.2 Optical System

The method of double pulsed holographic interferometry (see Vest [30]) is the primary diagnostic tool used in these experiments. The optical arrangement is shown schematically in Figure 2.2 which includes a top view of the shock tube and test section. The time-of-flight measurement system consisting of two He-Ne lasers and two optical detectors is also shown in Figure 2.2.

Light Source

The light source for recording the holograms is provided by a pulsed ruby laser which is designed to produce a sufficiently coherent pulse of light having an energy of ≈ 100 milli-joules and duration of ≈ 10 nano-sec when triggered by an external signal. The ruby laser is designed for *single mode* operation and produces a 2 mm (millimeter) diameter beam at 6943 Å (see Appendix B for a complete description of the ruby laser and its operation).

Object Beam

In general, a hologram is made by mixing two coherent beams on a photographic plate. The first optical element downbeam of the laser is the *beam splitter* which divides the emerging beam (from the ruby laser) into two coherent beams (referred to in Figure 2.2 as the *object beam* and the *reference beam*). The object beam first encounters a dielectric folding mirror which directs the beam through a short focal-length (f=15 mm) plano-convex lens. The latter expands the beam for subsequent collimation by a long focal-length (f=300 cm) spherical front-surface mirror (whose distance from the lens is equal to its own focal-length). The collimated object beam is 25 cm in diameter, permitting a sufficiently large area of the flow to be recorded. The beam is then directed through the test section windows as shown in Figure 2.2. Care is taken to assure that the light is perpendicular to the test section windows, a feature that is important for accurate evaluation of the holographic interferograms (see Vest [30]). The inside surface of the second window (adjacent to the lens) has a centimeter grid scribed on it. A 35 cm diameter imaging lens (shown in Figure 2.2) is used to reduce the diameter of the object beam in order to collect all the information of the flow on a smaller holographic plate. This imaging lens has a 52 cm focal length and is positioned 158 cm from the scribed surface of the window, resulting in a demagnified image (a factor of 1/2) of the scribed grid at the position of the holographic plate (which is 79 cm from the lens). The resultant interferogram (showing the flow density contours) will then include a superimposed image of the grid to serve as an aid for scaling and orientation of the flow for later analysis. The demagnification of this imaging system allows a large area of the flow in the test section to be imaged onto a smaller (4 × 5 in) holographic plate.

Reference Beam

As illustrated in Figure 2.2, the reference beam does not pass through the flow in the test section. In order to maximize the quality of the holographic

recording process, the reference beam (which passes through the beam splitter in Figure 2.2) must travel the same distance as the object beam before being remixed on the holographic plate. The difference in the optical path lengths between the reference and object beams must be less than the coherence length of the laser [30], which in this case is about 10 cm (see Appendix B). The two dielectric folding mirrors shown in Figure 2.2 direct the reference beam towards the holographic plate and are positioned such that this *optical-path-length* matching condition is satisfied. The reference beam is expanded by a negative-focal-length lens before it remixes with the object beam on the plate.

Holographic Plate

The object and reference beams both have diverging wavefronts at the plate. The angle between these beams at the center of the plate is 15 degrees but varies slightly at different positions on the plate because of the divergence of the beams. Off-axis holography requires a high-resolution recording medium. A recording medium with too low a *cutoff spatial frequency* has detrimental effects on the quality of the hologram. The spatial frequency required in this case can be estimated by considering the interference of two plane waves at a 15 degree incidence. The period d of the sinusoidal intensity distribution is given by [31]

$$2d \sin \frac{\alpha}{2} = \lambda \, ,$$

where d is the spatial period and α is the angle between the plane waves. The spatial frequency given by $1/d$ is less than 400 cycles/mm in this case. The holographic plates used for the experiments are made by *Agfa-Gevaert* (Type: 10E75 NAH). They are 4×5 inch glass, coated with a silver-halide emulsion that is specially sensitized for the ruby laser wavelength. The plates have an upper spatial frequency cutoff at 3000 cycles/mm [32], which is more than sufficient for this application. The development of the plates after exposure is accomplished by a three-step developing procedure (developer bath (D-19),

followed by a stop bath and then a fixer bath), typical of that used in standard black and white photography.

Double Exposure Method

A first exposure of the holographic plate by the object and reference beams is made before the shock tube is fired. This creates a hologram that contains the phase information of the whole optical system (including the windows). A second exposure (which creates a second superimposed hologram on the same plate) is then made a predetermined time after the shock tube has fired. This second hologram contains the same phase information of the optical system as the first hologram, but also includes additional phase information due to the presence of the flow between the windows. Different regions of the object beam wavefront are shifted in phase according to the distribution of the density of the flow. The specific refractivity k_o of the air relates the refractive index n and the mass density ρ in the relation

$$n - 1 = k_o \rho .$$

For air k_o is relatively constant over the visible portion of the spectrum, equal to $2.3 \times 10^{-4} \ m^3/kg$ [33]. The process as just described results in two super-imposed holograms on one plate which may be reconstructed simultaneously with a single continuous light source (sodium lamp) that is positioned at the same angle relative to the plate as the original reference beam. (The exposed plate is first developed before this reconstruction process.) Upon reconstruction, the mixed holographic images are photographed and the resulting image is a set of phase contour lines (fringes) which represent the phase difference between the wavefronts of the two object beams (see Figures 1.1→1.4). As-suming nothing has changed in the optical system between the first and second exposures (except for the addition of the flow in the second exposure), then the phase difference that is represented by the fringes on the photograph is due only to the presence of the flow during the second exposure; thus, the fringes

allow visualization of the flow. These fringes can then be directly related to density contours of the flow. (See Appendix C for a complete description of Double Pulsed Holographic Interferometry.)

2.1.3 Timing Electronics

The timing electronics provide a dual function of synchronizing the laser pulse with a specific flow event and also recording the time of flight of the shock.

Laser Pulse Synchronization

The double pulsed holographic method requires precise synchronization between the firing of the laser's second pulse and the desired *event* to be recorded during the flow. The flashlamp of the Ruby Laser must be turned on abⵇ ᵗt 1000 micro-sec before the laser pulse is needed (see Appendix B). A trigger signal simultaneously turns on the flashlamp current and starts a 1000 micro-sec delay circuit, which then triggers the Q-switch power supply, resulting in a 10 nano-sec laser pulse. An adjustable digital delay generator (DDG) is used between the shock wave detector and the laser power supply. The total delay of this configuration is the sum of the preset DDG setting ($0 \rightarrow 1000$ micro-sec) plus the fixed Q-switch delay (1000 micro-sec). Figure 2.3 shows a schematic diagram of this set up including the clock circuit for measuring the speed of the shock.

Shock Speed Measurement

Information about the shock speed is used mainly to monitor the repeatability of shock strength and flow conditions for each run of the shock tube. Since it is only possible to make one interferogram per shock, then it is necessary to repeat the same conditions a number of times. By use of the technique of repeated experiments with sequential advance of time delays for firing the
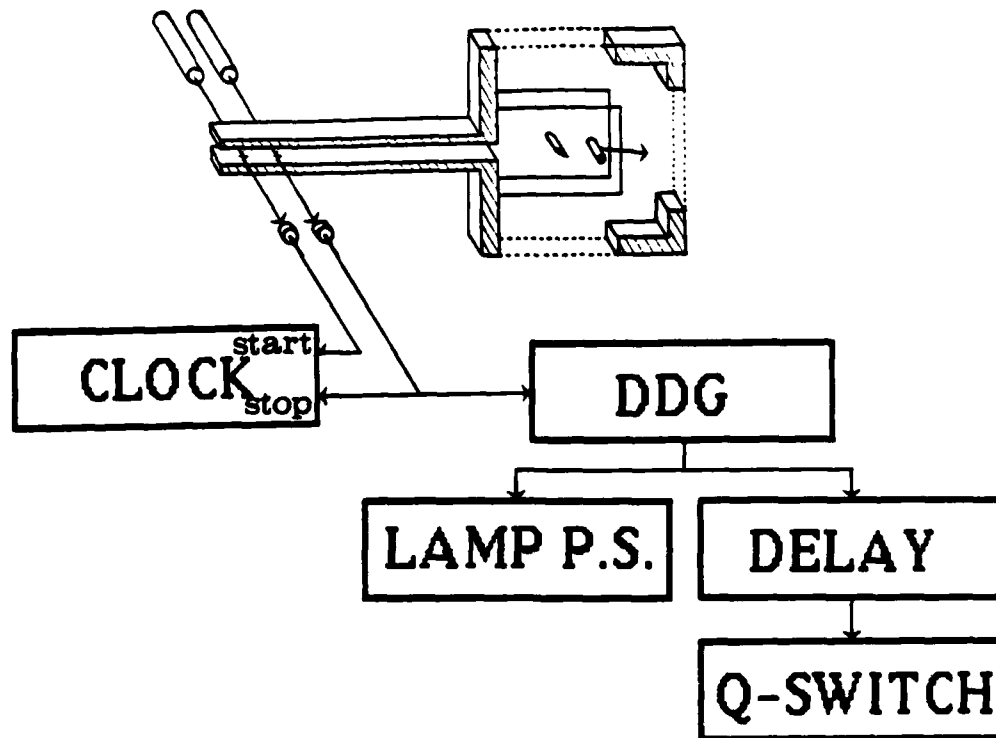
Figure 2.3: Timing Electronics for Measurement of Shock Speed and Synchronization of Laser Pulse.

laser, a time history of the flow events is obtained. The two HeNe laser beams used for this purpose have a diameter of .5 mm and are 98 mm apart. The errors in the speed measurement are due to the finite diameters of the beams and the resolution of the counter (clock). The finite size of the beams introduce a systematic error with an upper limit of 1%. Here, systematic error is less significant than random error. In this connection the resolution of the counter is .1 micro-sec and the typical time of flight of the shock between the beams is 143 micro-sec; the resulting random error is less than .1%. The latter can be decreased further by increasing the distance between the beams.

Operation of Timing Circuit

The x-t plot in Figure 2.4 describes the sequence of events in a typical experiment, along with the corresponding operation of the timing circuit. Superimposed on the x-t plot is a diagram of the shock tube and test section.
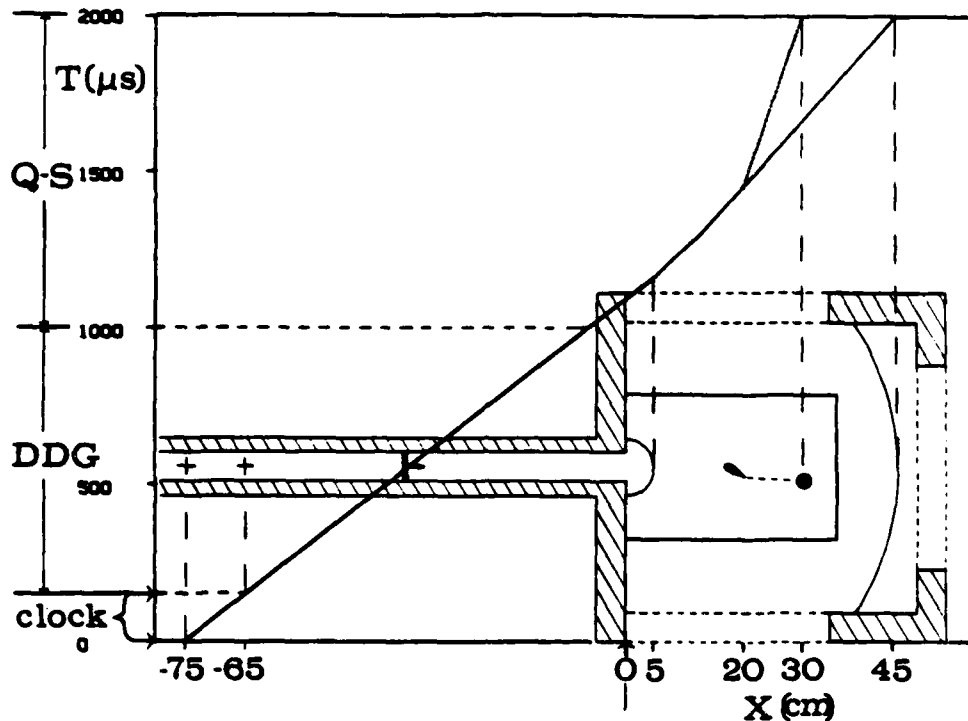
Figure 2.4: x-t Plot of Shock Wave and Vortex.

The two crosses represent the approximate positions of the HeNe beams for measuring the shock speed. The end of the shock tube (where the flow enters the test section) is used as the zero reference point in the x direction. The zero time reference is taken when the shock is at the position of the first HeNe beam (which is shown to be $\approx$ 75 cm from the end of the shock tube). The x-t plot of the shock in Figure 2.4 is a straight line before it reaches the end of the shock tube. As the shock wave passes by the first HeNe beam at t=0, a signal from the corresponding detector triggers the clock to start counting. As the shock passes the second HeNe beam (which is 65 cm from the end of the shock tube), the corresponding signal triggers the clock to stop and also simultaneously triggers the DDG. The time interval measured on the clock is about 143 micro-sec for a Mach 2 shock wave. The preset delay on the DDG in this illustrative case (Figure 2.4) is about 857 micro-sec so that its output pulse occurs at t=1000 micro-sec. The output pulse from the DDG then

turns on the flashlamp current and simultaneously triggers the 1000 micro-sec Q-switch delay (see Figure 2.3). In the case illustrated in Figure 2.4, it is shown that the flashlamp current is turned on and the Q-switch delay is triggered just before the shock enters the test section (at t= 1000 micro-sec). As the shock enters the test section, it is diffracted and begins to slow down at $x \approx 5$ cm where the section of the shock near the centerline of the flow begins to respond to the geometrical transition between the shock tube and test section. This delay in response of the shock to the geometrical changes of the tube walls is due to the supersonic velocity of the shock (Mach 2). At this point ($x \approx 5$ cm), the slope of the x-t plot of the shock slowly increases, which represents a proportional decrease in the shock speed along the centerline of the flow.

The x-t plot also shows the generation of the vortex at $x \approx 20$ cm, the coordinate of the trailing edge of the airfoil. The corresponding x-t plot of the vortex is shown in Figure 2.4 as a *branch* which is connected to the shock wave plot at the generation point of the vortex. This branch, has a larger slope than the shock wave plot. This difference in slope is expected because of the relative difference in the speeds of the vortex and the shock wave. The shock at this point is traveling at about 465 m/sec and the vortex is traveling at about 180 m/sec which is approximately the fluid velocity behind the shock (see Appendix D). Finally, the Q-switch is energized which pulses the laser at t=2000 micro-sec. The resulting interferogram contains flow-field density data for the case when the vortex and shock are at the locations shown in Figure 2.4 (the vortex is at $x \approx 30$ cm and the shock is at $x \approx 45$ cm). As shown in Figure 1.1, the DDG setting may then be increased by 20 micro-sec and the experiment repeated, resulting in a new interferogram of the vortex and shock in new positions corresponding to the increased delay time. If the shock tube flow is repeatable, then the new interferogram would accurately represent the flow at a time which is 20 micro-sec later than the previous interferogram. This technique of repeated experiments with sequential advance of time delays for firing the laser provides a time history of the density distribution in the

flow field, including the density distribution within the vortex.

2.1.4 Pressure Transducer

With the aid of the superimposed reference grid, the coordinates of the center of the vortex are located in each interferogram. A series of sequential interferograms as described yields the vortex trajectory. A pressure transducer mounted in the window with its pressure-sensitive end mounted flush at the inside window surface records the static pressure of the vortex as it travels along its trajectory (see Appendix E for a complete description of the pressure transducer and the associated electronics for data acquisition). This is a temporal pressure response of the traveling vortex at one point fixed relative to the laboratory and is used to estimate the spatial pressure distribution in the vortex by means of a Galilean transformation of the data. The latter is performed under the physical assumption that the spatial distribution of the vortex does not change appreciably during the time interval when the vortex travels a distance equal to its own diameter, i.e., the duration of time required to make the pressure measurement across the diameter of the vortex. The velocity of the vortex (≈ 180 m/sec) is measured in several ways (see Appendix D for a complete description of the vortex velocity measurements) and is clearly important for obtaining radial pressure profiles across the vortex. The diameter of a vortex is not well defined, but for this purpose the diameter of interest is defined across the region where the density and pressure gradient of the vortex is observable (see Figures 1.2 and 1.3). The diameter of the vortex by this convention is about 1 cm; and, given the vortex velocity (180 m/sec), the duration of the pressure measurement turns out to be about 50 micro-sec. The time-response of the pressure transducer must be better than 20 kilocycles/sec in order to accurately follow the temporal pressure changes of the traveling vortex.

Another factor affecting the accuracy of the pressure data is the magnitude of the actual pressure sensitive area of the transducer which is .028 inches in

diameter. The transducer diameter is then about 7% of the vortex diameter. The combined effects of the limited time-response and the finite size of the transducer results in a *spreading out* of the pressure distribution. These effects can be partially corrected for when evaluating the data (see Section 2.3.2 *Evaluation of Pressure Data*). The pressure data is originally recorded with an oscilloscope and then a photograph of the trace is later digitized for further processing.

2.2   Experimental Procedures

The two experimental methods, namely holographic interferometry and pressure transducer response measurements yield quantitative information about the density distribution and the pressure distribution of a free vortex that is generated under a specific set of repeatable conditions. As was noted, the method of holographic interferometry is used repeatedly at different delay times and thus provides the two-dimensional density distribution of the vortex at different positions along its path, corresponding to different ages of the vortex. Thus, these measurements constitute a time-dependent study of the vortex. The method used to obtain pressure information provides the pressure distribution of the vortex at a single position along the vortex trajectory, which corresponds to a vortex of a specific age. The following two sections will describe the conditions under which the interferometric and pressure data are obtained for this study.

2.2.1   Holographic Interferometry Data

For this study, the time interval used between successive experiments is about 50 micro-sec. A total of 21 interferograms are made for a complete study of the flow. These 21 successive experiments, in 50 micro-sec intervals, covering a total range of 1000 micro-sec, are required in order to follow the development

of the flow from the time the shock enters the test section to the time when the traveling free vortex reaches the downstream edge of the window and thus exits from the field-of-view. The faster moving shock passes the downstream edge of the window much sooner than the vortex and is therefore visible in only the first 12 interferograms. In the actual experiments, the DDG setting (see Section 2.1.3) is advanced by 50 micro-sec for each successive experiment. Since the speed of the shock is not exactly the same in each experiment, an error occurs in the timing of the flow events (see Appendix C for a complete description of the timing errors) and the actual time intervals are either slightly less or more than the 50 micro-sec DDG setting. Figure 2.5 shows the 25 × 36 cm window of the test section along with the positions of the shock at the centerline of the flow corresponding to ≈ 50 micro-sec intervals (indicated by the numbers 1→12) as recorded on the first 12 interferograms. Also shown in Figure 2.5 is the vortex trajectory (vortex positions at ≈ 50 micro-sec intervals) which is recorded on Interferograms #6→#21. The x-y coordinate system in Figure 2.5 has the centerline of the flow (centerline of shock tube) as the zero reference for the y coordinates and the end of the shock tube (beginning of test section) as the zero reference for the x coordinates. Figure 2.6 is a *close-up* of Figure 2.5 showing the trajectory of the vortex in more detail (the position of the center of the vortex as recorded in Interferograms #6→#21 is plotted with respect to the same coordinate system as shown in Figure 2.5).

2.2.2 Pressure Data

Pressure transducer response measurements of the vortex are obtained during several shock tube *runs* in order to check repeatability. Figure 2.6 indicates the location of the pressure transducer with respect to the vortex trajectory. The pressure measurement requires a time duration corresponding to the time it takes for the full vortex diameter to travel past this point (≈ 50 micro-sec). One of the physical assumptions used in the evaluation of the
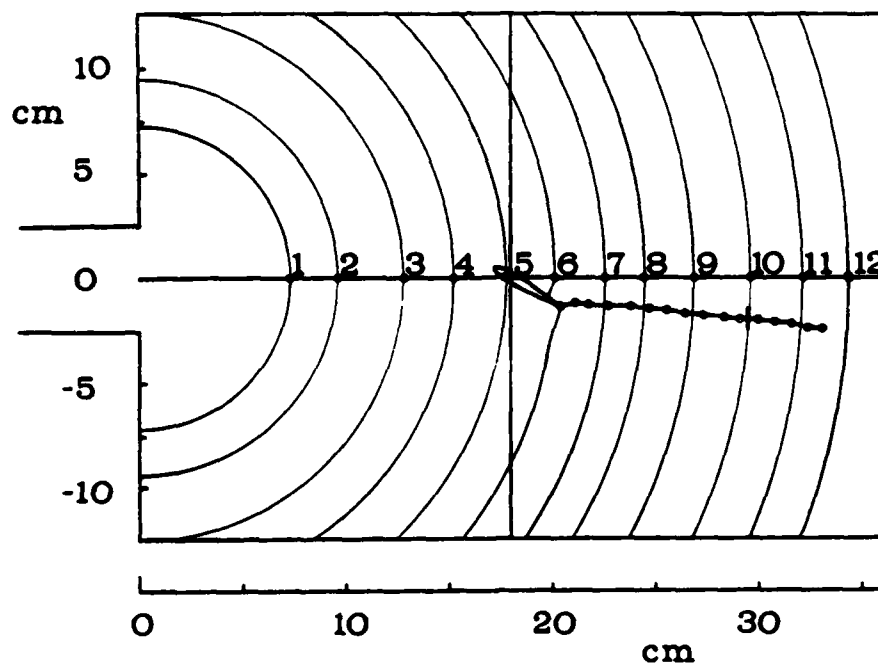
Figure 2.5: Positions of Shock and Vortex at $\approx$ 50 Micro-Sec Intervals.
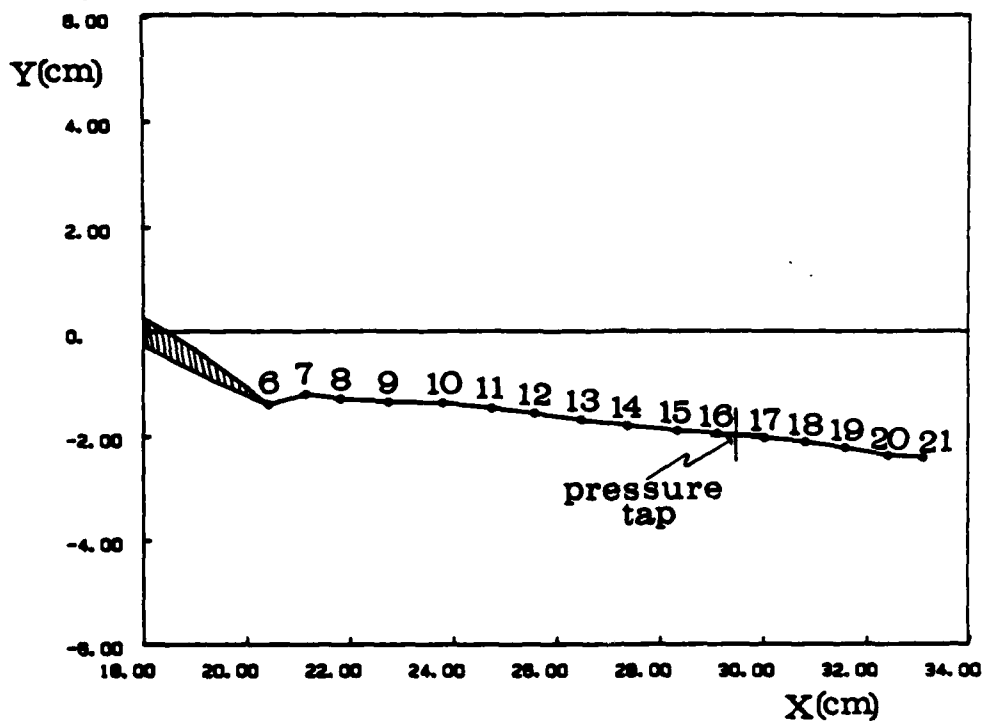
Figure 2.6: Position of the Center of the Vortex as Recorded in Interferograms #6→#21.

pressure data is that a relatively small change in the vortex structure takes place during the 50 micro-sec time interval of the pressure measurement. This *slow-change* assumption allows the time-response of the pressure transducer to be transformed into a radial pressure distribution of the vortex by means of a Galilean transformation, as mentioned earlier. The pressure transducer is located between the two vortex positions #16 and #17 as shown in Figure 2.6. Interferogram #16 gives the density profile of the vortex immediately before the pressure measurement and Interferogram #17 gives the density profile immediately after the pressure measurement. These two density profiles can then be compared (see Appendix H, Figure H.15) in order to check the validity of the *slow-change assumption* which is used in the evaluation of the pressure data.

2.3 Data Reduction Procedures

2.3.1 Evaluation of Interferograms

Physical Considerations

Interferometry of plane flow fields utilizes a straightforward relation to determine the density $\rho(x, y)$ as a point function measurement of the fringe shift $S(x, y)$. If L denotes the distance spanned by the light beam in the direction of the ignorable coordinate z, then

$$\rho(x, y) - \rho_o = \frac{\lambda}{k_o L} S(x, y) ,$$

where ρ_o is a reference density related to the no-flow fringe pattern, λ is the light wavelength, and k_o is the specific refractivity of the air (see Section 2.1.2). The value of L is given by the distance between the windows (5 cm). In this study the *density reference* ρ_o corresponds to the density of the air directly behind the shock wave along the centerline of the flow. This is calculated using

the shock relations and the known value of shock Mach number. The fringe shift in this case corresponds to a density change of .060 kg/m^3 (from one dark line to the next adjacent line in the interferogram), which is approximately 1/20 of atmospheric density at sea level.

The interferograms are evaluated by means of the above relation which is valid under the following conditions:

- The flow is two-dimensional.
- The light beam is not refracted as a result of the density gradients.

The test section is designed to rotate 90 degrees about the axis of the shock tube. Interferograms made from this angle allow the two-dimensional flow assumption to be checked by observation (see Appendix C for further details on the testing of the two-dimensionality of the flow and the calculation of errors due to the density gradients of the vortex).

Evaluation Procedure

Figure 2.6 shows the positions of the vortex in Interferograms #6→#21 which represent ≈ 750 micro-sec of the vortex lifetime as it travels a distance of about 12 cm. After an initial growth and adjustment period during the first 100 micro-sec (see #6, #7 & #8 in Figure 2.6), the vortex follows a reasonably linear path at a constant velocity during the latter ≈ 650 micro-sec. It is this latter period which is of interest in this study and thus a careful evaluation of Interferograms #8→#21 is neccessary. The evaluation of these 14 interferograms reveals the radial density distribution of the vortex during this period of time. The density data is derived directly from the interferograms by the following procedure:

(a) The fringes in each interferogram are identified and numbered with respect to the reference fringe directly behind the shock wave.

(b) The image of the vortex from each interferogram is enlarged (see Interferograms in Appendix C).

(c) The center of the vortex is identified.

(d) A horizontal line (x direction) is drawn through the center of the vortex.

(e) The center of each fringe is identified along the line.

(f) The radial distance of each numbered fringe (along the line) from the center of the vortex is measured by hand several times with a micrometer and an average value is calculated. These values of r are given negative and positive values depending upon which side of the vortex center they were measured from. These negative and positive values of r distinguish the two different regions of the vortex on either side of its center; a convention followed throughout this study.

(g) Using the known value of the air density directly behind the shock as a reference (see Appendix E, Section E.5), the density represented by each fringe and the corresponding radial distance is tabulated for the ≈ 25 fringes in each of the 14 interferograms yielding 14 separate radial density data sets (see *Vortex Density Tables* in Appendix I).

(h) The corresponding age of the vortex is recorded for each radial density data set. This value of t is used to identify each radial density profile and is used to characterize the time-dependence of the data.

(i) The data is entered into a computer for further reduction (see Section 2.3.3).

Although the radial density distribution of the vortex is assumed to be axisymmetric throughout most of this study (under this assumption it would be only neccessary to sample the radial density profile along any one radius), the above procedure samples the density across the whole diameter of the vortex ($-r \rightarrow r = 0 \rightarrow +r$), which allows a check of this assumption. The errors found in the subsequent curve fitting of the data to a radially symmetric function (see Section 2.3.3) give an indication of the validity of the axisymmetric assumptions used in this study.

2.3.2   Evaluation of Pressure Data

Physical Considerations

The fast-response Silicon Diaphram Pressure Transducer has a small measuring area and is flush-mounted in the acrylic window at a single location along the path of the vortex (see Figure 2.6). The gauge measures the pressure at the wall surface as the vortex travels by, and a time history of the pressure at that point on the wall is recorded. The temporal pressure information can then be transformed into a radial pressure profile of the vortex under the following conditions:

- The flow is two-dimensional.

- The vortex convection speed is linear, constant and known.

- The center of the vortex passes over the gauge.

- The vortex does not change appreciably as it travels one vortex diameter.

- The pressure-sensitive area is small compared to the size of the vortex.

- The time-response and sensitivity of the gauge is sufficient to track the pressure profile as it passes over.

Along with the need of a well-characterized flow, the accuracy of the pressure measurements are dependent on the careful positioning of the gauge and the specifications of the device itself. These considerations must be accounted for in the evaluation of the pressure data. In this study, the pressure data is deconvolved to correct for the limited time-response and physical size of the device, and the proper positioning of the gauge is verified (see Appendix E). Also, the flow conditions above are sufficiently met (see Appendix C).

Evaluation Procedure

The pressure response of the transducer is recorded by photographing the oscilloscope traces during each shock tube run. For this study, two oscilloscopes

were used simultaneously at different scan rates and triggered at different delay times in order to capture both the time-response of the whole flow and the time-response of only the vortex. The pressure data is evaluated by the following procedure:

(a) The photographed traces are digitized by hand with a digital tablet and the information is stored in a computer.

(b) The stored information, which represents the voltage vs. time-response at a fixed sampling rate is then transformed into pressure vs. time information by means of a calibration factor.

(c) The pressure vs. time curve for the passing shock is used as an approximation of the *step-response* of the system. This information is used along with the aid of a Fast Fourier Transform (FFT) program to deconvolve the pressure signal (of the vortex) which has undergone a spreading effect as described in Section 2.1.4.

(d) The deconvolved data is then transformed from a pressure vs. time curve to a radial pressure distribution by means of a Galilean transformation using the known convection velocity of the vortex found by the time-of-flight measurements described in Appendix D.

A complete description of the digitizing/sampling, calibration, deconvolution and transformation processes is given in Appendix E.

2.3.3 Curve Fitting of Data

The evaluation of the interferograms and pressure measurements results in data that represent the radial distributions of these properties inside the vortex. It is desired to use this information to calculate other additional physical properties of the vortex. For this purpose it is convenient to approximate the density and pressure distributions of the vortex by fitting curves to the data. A least squares curve fitting method is used to find compact mathematical

representations of the density and pressure data. These empirical formulas
are then used in the governing equations of a theoretical model of the vortex
(see Section 1.1.2, Chapter 1) to calculate other physical properties. A de-
scription of the curve fitting method is given in Appendix F. Descriptions of
the results, including an analysis of errors, are given in the following chapter
and in the appendices.

Chapter 3

Experimental Results and Physical Interpretation

3.1 Vortex Density

Evaluations of the interferograms supplemented by the curve fitting procedures (as described in Chapter 2) result in 14 individual density distributions of the vortex, corresponding to incremental changes in the vortex location and age. These distributions describe the vortex as measured at Stations #8→#21 shown in Figure 3.2 which indicate the measured locations of the vortex center along the convected path. The results of the interferogram evaluations are given in the tables in Appendix I (*Vortex Density Tables*). The graphical results of both the density evaluations and the respective curve fitting investigations are given in the figures in Appendix H (*Vortex Density Curves*). A sample of these results is shown in Figure 3.1. The curve and points plotted in Figure 3.1 represent the density distribution of the vortex at Station #16. This particular density profile (#16) is significant because it represents the density of the vortex at a location and time which corresponds

45

to that of the pressure measurements. This correspondence can be observed in Figure 3.2. The crossed lines in Figure 3.2 indicate the position of the pressure transducer along the convected path of the vortex center. The results of the pressure measurements (see Section 3.2) show that the pressure variations (associated with the vortex) generally extend ≈ 5 mm from the vortex center. The location of the vortex center in Experiment #16 (as shown in Figure 3.2) is ≈ 5 mm upstream of the pressure transducer; and thus, pressure measurements of the vortex begin at this time. The corrected vortex age in this location is t=496 micro-sec, which is determined by methods given in Appendix C. The density distribution shown in Figure 3.1 is used along with the corresponding pressure results for further calculations of other vortex properties (see Chapter 4). The density is given in units of kg/m^3 and is plotted as a function of the radius r. The density is evaluated across the diameter of the vortex and by convention, the independent variable r in the density plots is allowed to take on negative and positive values on the opposite sides of r=0. The 38 data points in this plot represent the positions of the central region of each fringe in Interferogram #16 (see Interferogram #16 in Appendix C). Table I.9 in Appendix I gives the results of the evaluation of Interferogram #16. Figure H.9 in Appendix H shows the results of the curve fitting to the data in Table I.9. The solid line in Figure 3.1 represents the *best-fit curve* to the data. The curve chosen for this purpose is a modified Cauchy distribution given by

$$\rho(r,t) = \rho_\infty(t) - \frac{\Delta\rho(t)}{1 + \left(\frac{r}{\Delta r(t)}\right)^2},$$

where the three parameters $\rho_\infty(t)$, $\Delta\rho(t)$ and $\Delta r(t)$ represent, respectively, the ambient density of the flow, the *well-depth* of the curve and the *half-width* (half width at half maximum) of the curve respectively. Each of these three parameters are functions of time and represent three different characteristics which define the shape of the density curve; thus, the time dependence of these parameters describe the structure and behavior of the vortex. The values of $\rho_\infty(t)$, $\Delta\rho(t)$ and $\Delta r(t)$ corresponding to the time t=496 micro-sec,

EXP.#16 $t = 496\,\mu s$

VORTEX RADIAL DENSITY PROFILE

$$\rho(r) = \rho_\infty - \frac{\Delta\rho}{1 + \left(\frac{r}{\Delta r}\right)^2}$$

$$\rho_\infty = 1.787\,\frac{kg}{m^3}$$

$$\Delta\rho = 1.076\,\frac{kg}{m^3}$$

$$\Delta r = .166\,cm$$
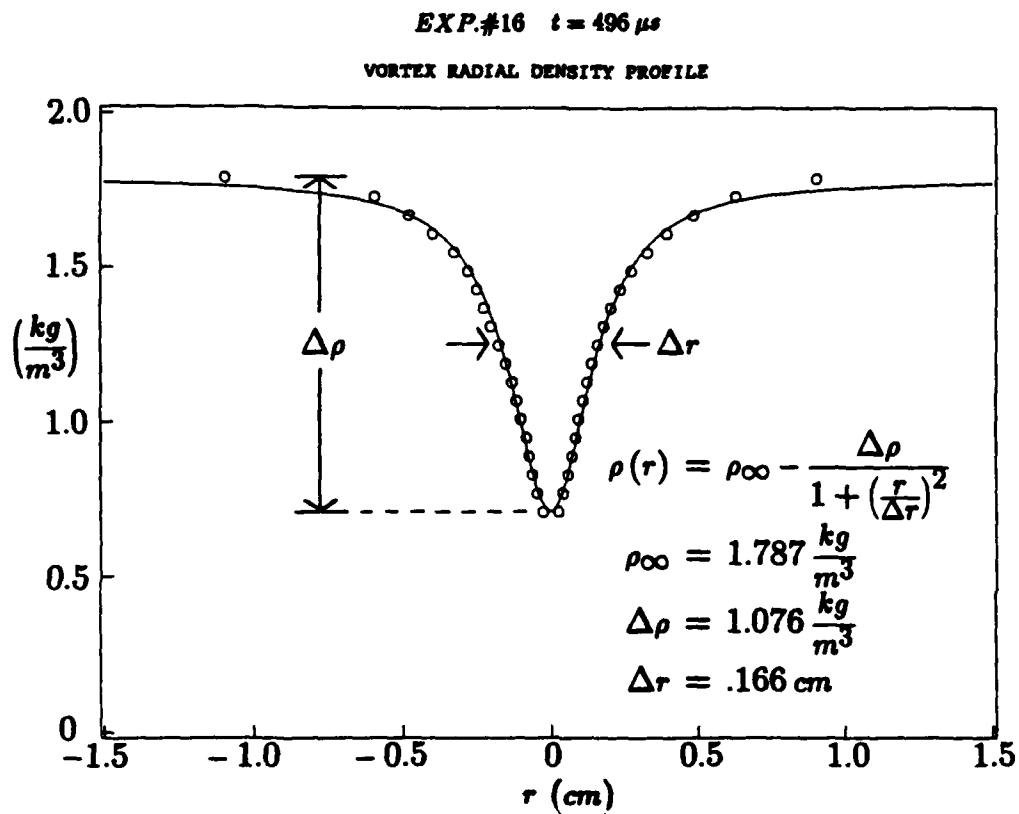
Figure 3.1: Vortex Radial Density Profile (from Interferogram #16, t=496 micro-sec)

are given in Figure 3.1. This figure also shows a plot of both the data and the *fitted* curve. A closeness-of-fit analysis of the curve in Figure 3.1 reveals an RMS deviation of the residuals to be .021 kg/m^3 (see Appendix J, Table J.1), which when normalized with respect to the well-depth $\Delta\rho$, becomes 2.1%. The fringe location error associated with the digitization process is found to have an RMS value of .024 cm (see Appendix J, Table J.2). This type of random error is found to be largest at the outer boundaries of the vortex where the fringe widths become large. The general error in the fringe shift due to the digitization process is found by normalizing this RMS value with respect to the average value of radii measured (.241 cm), which gives a value of 10%. Another type of error, namely the error in fringe position due to the refraction of the light rays as they pass through the vortex, is approximated by a simple ray bending analysis (see Appendix C). By using the density parameters given in Figure 3.1 (Experiment #16), a value of .0066 cm is calculated as the maximum transverse displacement of a ray due to bending by the density gradient of the vortex (see Table C.1, Appendix C). This maximum bending occurs in the region of the vortex near $r = \Delta r$ where the distance between the fringes in the interferogram are about .015 cm (see Table I.9, Appendix I); thus, the maximum resultant error in fringe shift caused by this refraction is about 44%. This ray bending causes the system of fringes to move systematically, resulting in a spreading of the density profile.

The values of the parameters $\rho_\infty(t)$, $\Delta\rho(t)$ and $\Delta r(t)$ are found for each case (Experiments #8→#21), using a least squares curve fitting method (described in Appendix F), and correspond to a particular time t associated with the vortex age. These results are shown in Appendix H (*Vortex Density Curves*) and tabulated in Table I.15 (Appendix I). The general behavior of the vortex density can be observed from this information and is summarized below:

- The ambient density ρ_∞ characterizes the density of the flow outside of the vortex. This parameter decreases slowly with time due to the nature of the expanding flow behind the curved shock. Only a 12% change

occurs in this parameter during the time period under investigation (750 micro-sec).

- The well-depth $\Delta\rho$ characterizes the *intensity* of the vortex. It is the whirling motion of the vortex flow which contributes to the large density drop in the center due to the centrifugal reactions. A 45% change occurs in this parameter during the time period investigated.

- The half-width Δr characterizes the *size* of the vortex by identifying the radial distance at which the density drop in the vortex is at half the peak value. The time behavior of this parameter is a measure of the relative growth of the vortex and is found to be a slow function of time compared to the rapidly decreasing well-depth. A 6% change occurs in this parameter during the time period investigated.

The well-depth and the half-width parameters are basic factors in characterizing the structure and behavior of the vortex. It is convenient to normalize this distribution with respect to the ambient density, ρ_∞, resulting in a function with only two parameters

$$\rho^*(r,t) = 1 - \frac{\Delta\rho^*(t)}{1 + \left(\frac{r}{\Delta r(t)}\right)^2},$$

where $\Delta\rho^*(t)$ is now the normalized well-depth. The normalized distributions for the 14 experiments are given in Appendix H.

The three density distributions taken from Experiments #10, #14 and #18 are representative of the vortex at three locations which are approximately 4 cm apart spatially and 200 micro-sec apart in time. These locations are identified in Figure 3.2 by the heavy arrows and the results from the interferograms are shown in Figures 3.3, 3.4 and 3.5. The normalized results from these three experiments are plotted together in Figure 3.6, which illustrates the time behavior of the shape of the density curves. In this form there are only two time-dependent parameters which characterize the shape of the curve: $\Delta\rho^*(t)$ and $\Delta r(t)$. The best-fit values for these parameters are plotted
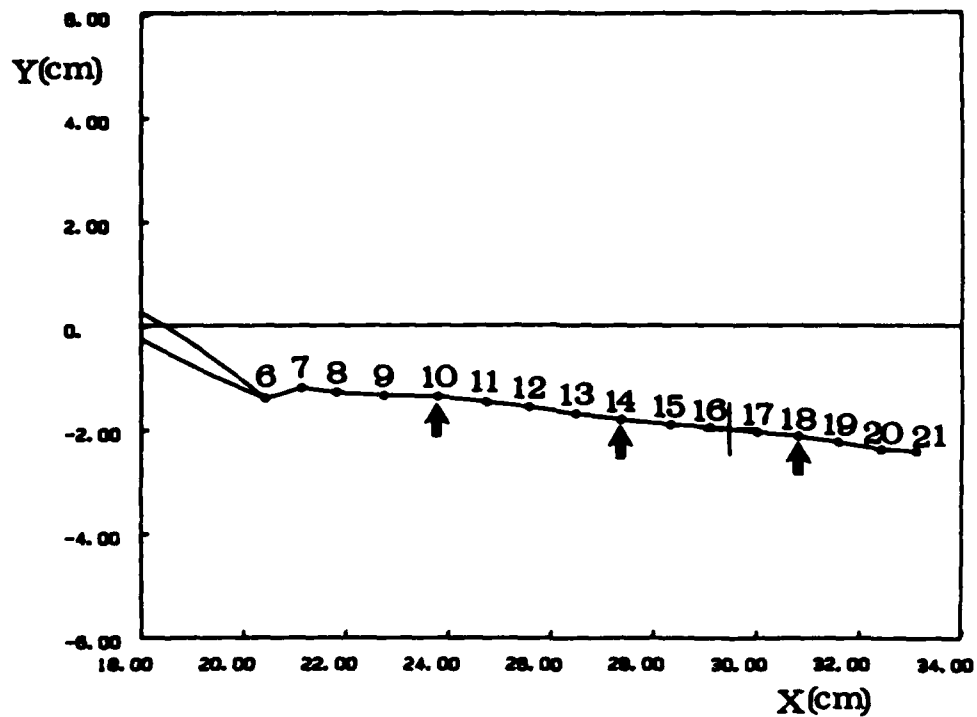
Figure 3.2: Trajectory of Vortex Showing Locations of Vortex Center in Experiments #6→#21.
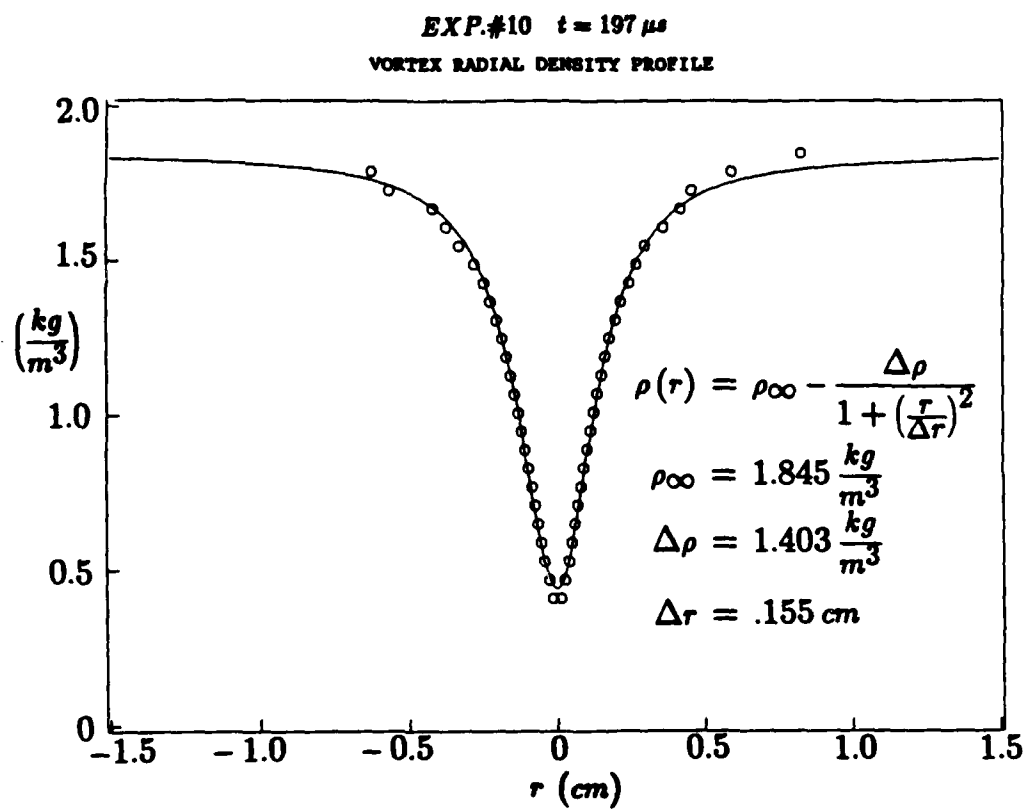
Figure 3.3: Vortex Radial Density Profile (from Interferogram #10, t=197 micro-sec).

EXP.#14 $t = 401\,\mu s$

VORTEX RADIAL DENSITY PROFILE

$$\rho(r) = \rho_\infty - \frac{\Delta\rho}{1+\left(\frac{r}{\Delta r}\right)^2}$$

$$\rho_\infty = 1.766\,\frac{kg}{m^3}$$

$$\Delta\rho = 1.168\,\frac{kg}{m^3}$$

$$\Delta r = .163\,cm$$
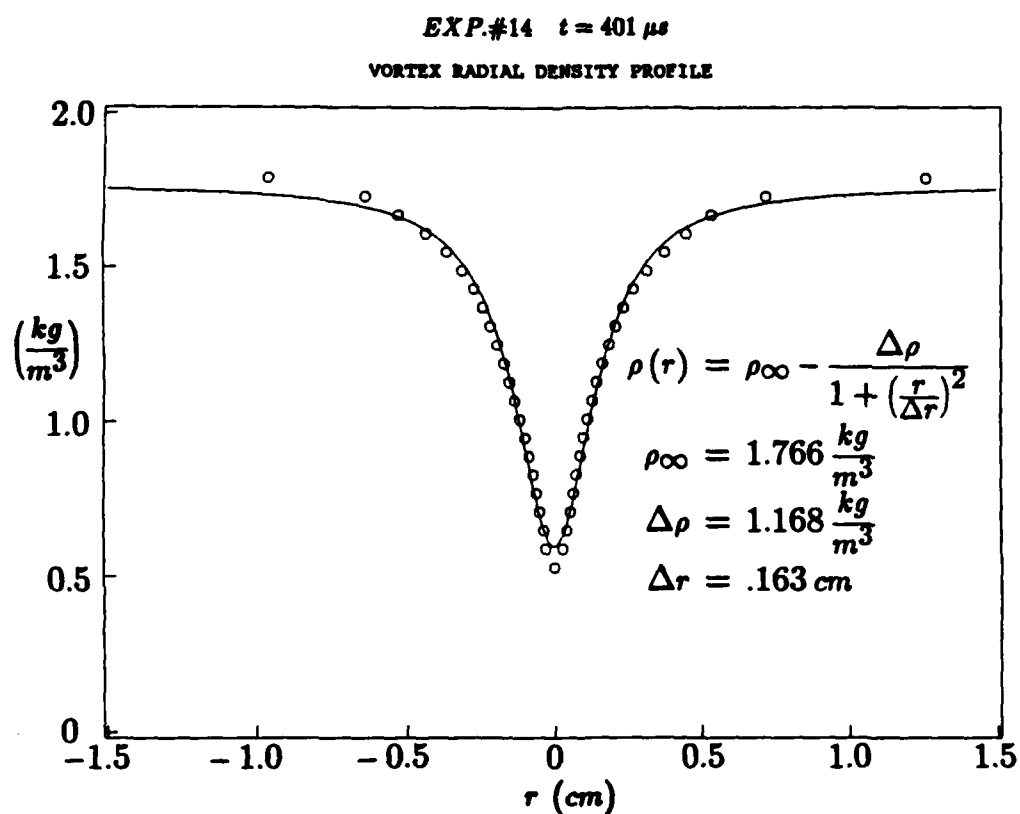
Figure 3.4: Vortex Radial Density Profile (from Interferogram #14, t=401 micro-sec).

EXP.#18 $t = 598\,\mu s$

VORTEX RADIAL DENSITY PROFILE

$$\rho(r) = \rho_\infty - \frac{\Delta\rho}{1 + \left(\frac{r}{\Delta r}\right)^2}$$

$$\rho_\infty = 1.778\,\frac{kg}{m^3}$$

$$\Delta\rho = 1.014\,\frac{kg}{m^3}$$

$$\Delta r = .178\,cm$$
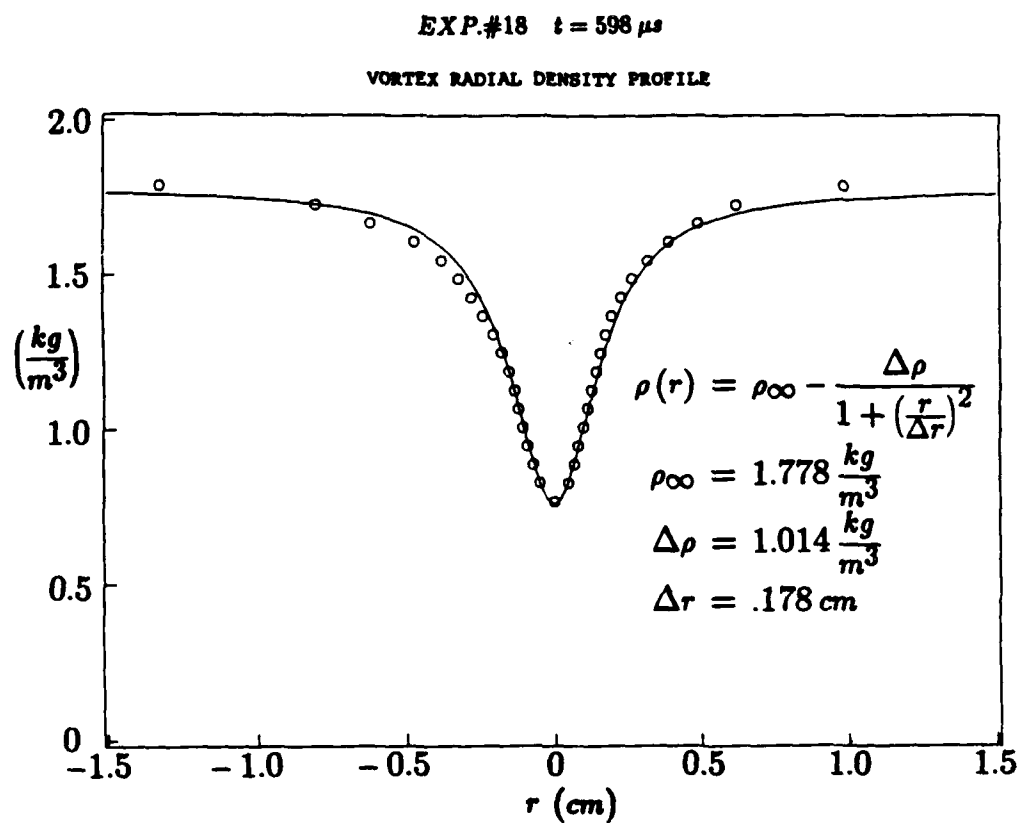
Figure 3.5: Vortex Radial Density Profile (from Interferogram #18, t=598 micro-sec).

with respect to time t in Figures 3.7 and 3.8. The solid line in Figure 3.7 is a best-fit curve to values. The curve is a two parameter exponential decay function given by

$$\Delta\rho^*(t) = \Delta\rho_o^* e^{-\frac{t}{\tau}} ,$$

where the parameter $\Delta\rho_o^*$ represents the initial value of the normalized well-depth $\Delta\rho^*$ at t=0 and the parameter τ represents a characteristic decay time of $\Delta\rho_o^*$. It is observed that the time period defined by $t = 0 \rightarrow t = \tau$ is one in which the vortex is in a highly compressible state. This curve was fit to the 14 equally weighted values of $\Delta\rho^*$ as given in the figures in Appendix H. The 14 points are shown in the plot and are superimposed over the plot of the curve in order to illustrate the closeness-of-fit. The points from Experiments #10, #14 and #18 are indicated by the arrows in Figures 3.7 and 3.8. Use of the exponential decay function as an empirical formula to describe the unsteady well-depth is consistent with the following logic:

- It has an initial finite value at t=0.

- It asymptotically approaches zero with increasing time.

- This function has a minimal number (2) of free parameters.

The values of Δr with respect to time are not quite as well-behaved as seen in Figure 3.8, but after an initial decrease in value during the first three experiments, the parameter Δr slowly increases. It was decided to neglect the first two points of each set for the curve fitting. A slowly increasing linear function was found to fit the set of points from Experiments #10→#21. This function and the values of the parameters for a best-fit line are shown in Figure 3.8. The parameter Δr_o represents the initial value of Δr at t=0 and the parameter Θ represents the rate of growth of the parameter Δr. The points are seen to have a small oscillatory component about the fitted line. The equations and constant values given in Figures 3.7 and 3.8 substituted

VORTEX RADIAL DENSITY PROFILE

$$\rho^*(r,t) = 1 - \frac{\Delta\rho^*(t)}{1 + \left(\frac{r}{\Delta r(t)}\right)^2}$$
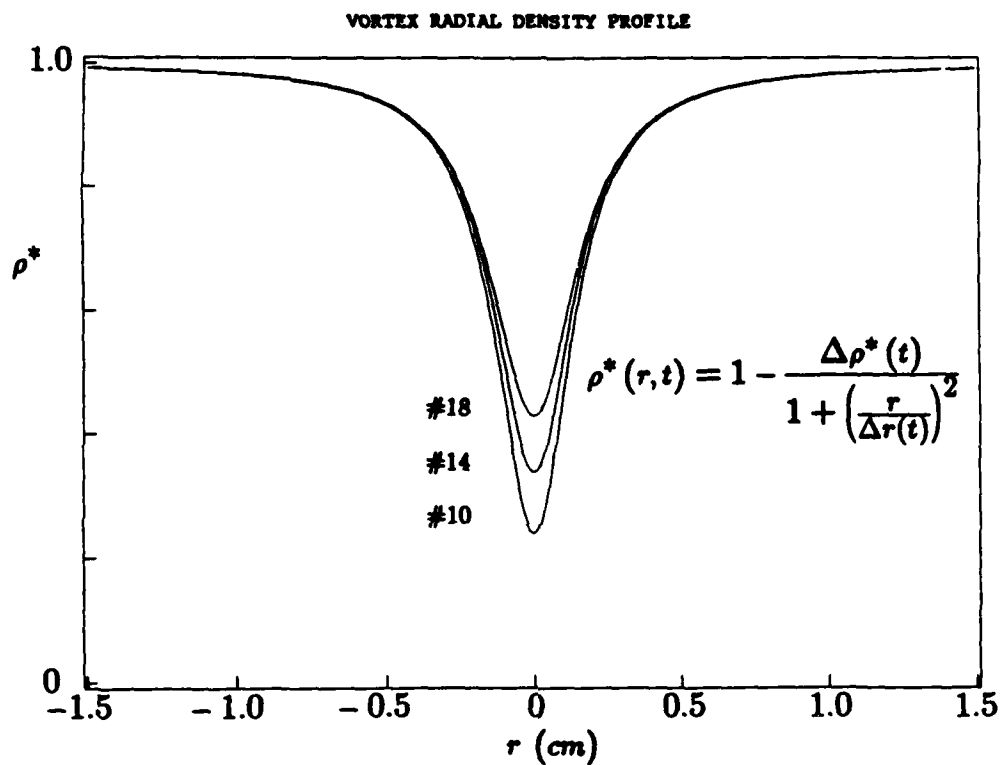
Figure 3.6: Normalized Vortex Radial Density Profiles (from Interferograms #10, #14 and #18).
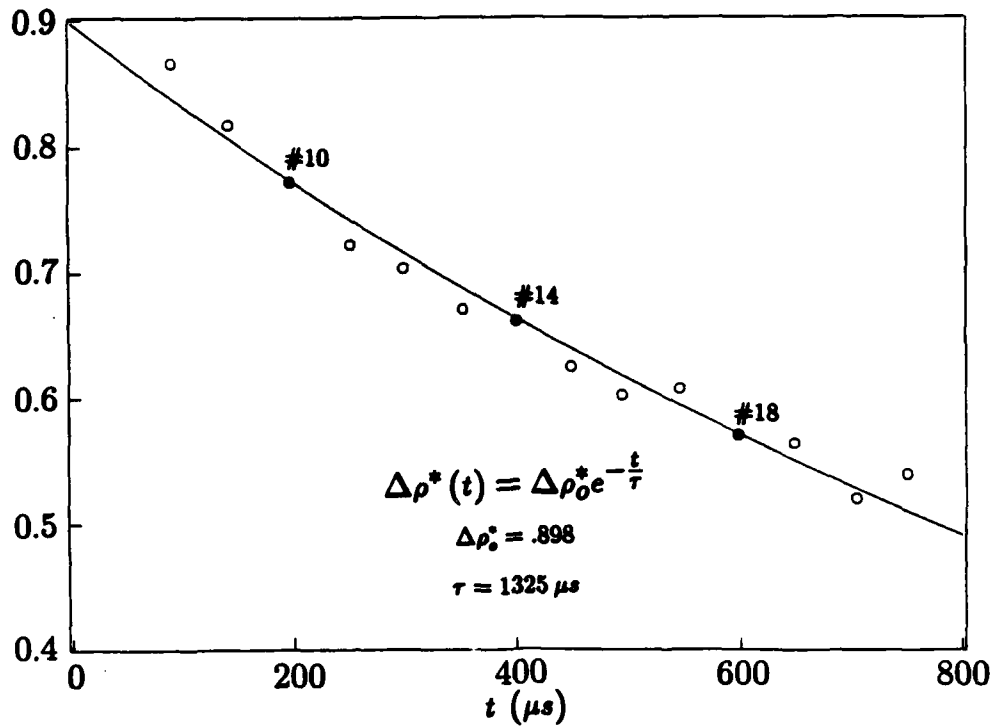
Figure 3.7: Results of Curve Fitting to Time Sequence of Vortex Well-Depth Parameters.

into the equation given in Figure 3.6 yield

$$\rho^*(r,t) = 1 - \frac{\Delta\rho_o^* e^{-\frac{t}{\tau}}}{1 + \left(\frac{r}{\Delta r_o + \Theta t}\right)^2}$$

$$\Delta\rho_o^* = .898$$

$$\Delta r_o = .143 \ cm$$

$$\tau = 1325 \ \mu s$$

$$\Theta = 57.2 \ cm/s \ ,$$

which is an approximate representation of the normalized density data from the 12 experiments #10→#21. A closeness-of-fit test of this formula to the data set reveals an RMS deviation of the residuals to be .0388 kg/m^3, which when normalized with respect to $\Delta\rho = 1.076 kg/m^3$, becomes 3.6% (see Appendix J, Tables J.3→J.12). Each of the 4 constants in this relation is evaluated by the curve fitting procedure, and characterizes a different aspect of
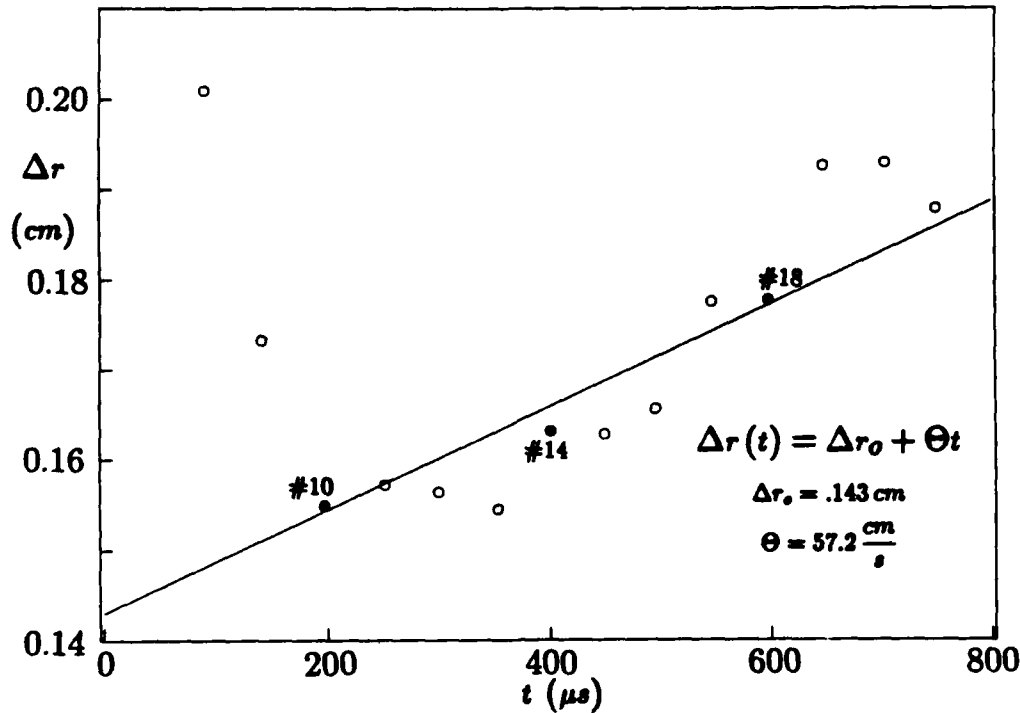
Figure 3.8: Results of Curve Fitting to Time Sequence of Vortex Half-Width Parameters.

the vortex behavior. The first two constants $(\Delta\rho_o^* = .898$ and $\Delta r_o = .143\ cm)$ represent the radial density distribution at t=0. At time t, the density ratio across the vortex is given by

$$\frac{\rho_\infty}{\rho_\infty - \Delta\rho} = \frac{1}{1 - \Delta\rho_o(t)}\ ,$$

which has an initial value at t=0 of 9.8. The halfway point of this change is given by $\Delta r_o = .143$ cm. The last two constants $(\tau = 1325$ micro-sec and $\Theta = 57.2$ cm/sec) describe the time behavior of the vortex. A characteristic lifetime of the vortex given by $\tau = 1325$ micro-sec represents the time it takes for the well-depth of the vortex density profile to go from its initial value to the value given by

$$\Delta\rho = \left(\frac{1}{2.7}\right)\Delta\rho_o\ .$$

In this latter case, the density ratio across the vortex is 1.5, which is greatly reduced from the initial factor of 9.8. The vortex can be said to be *in a state*

of high compressibility during this first 1325 micro-sec. The growth rate of Δr is given by $\Theta = 57.2$ cm/sec which describes the behavior of the density half-width. The density half-width Δr increases by only a factor of 1.5 during the first 1325 micro-sec of the vortex lifetime, whereas during this same time period, the density ratio decreases to 1/7 of its initial value. Thus, the width of the vortex density profile does not increase rapidly as compared to the rate of the decreasing well-depth.

3.2 Vortex Pressure

The complete results of the pressure experiments and a description of the processing of the data are detailed in Appendix E. The following is a description of the final form of the pressure data and the results of the curve fitting procedure.

Results of Curve Fitting

Figure 3.9 shows the vortex pressure data in their final digitized form and the results of the curve fitting of a modified Cauchy function to the data. Appendix E contains a complete description of the digitization and further processing of the pressure data. There are 84 equally spaced points plotted in units of N/m^2 (or pascals) as a function of radial distance from the center. The superimposed solid line in Figure 3.9 represents the best-fit-curve of the same form as that used for the density distribution (modified Cauchy distribution). This pressure distribution is given by

$$P(r,t) = P_\infty - \frac{\Delta P}{1 + \left(\frac{r}{\Delta r_P}\right)^2}$$

$$P_\infty = 152100 \frac{N}{m^2}$$

$$\Delta P = 107300 \frac{N}{m^2}$$

$$\Delta r_P = .117 \; cm \; ,$$

in which the three constant parameters characterize the profile in parallel with that discussed in the preceeding section. A closeness-of-fit test comparing this formula to the data reveals an RMS deviation of the residuals to be 6,001 N/m^2 which when normalized with respect to the well-depth $\Delta P = 107,300 \; N/m^2$, becomes 5.6% (see Appendix E, Tables E3→E4). It is shown in Figure 3.9 that most of the fitting error is a result of forcing an asymmetric set of data points to fit a symmetrical formula. The noise associated with this type of measurement is another cause of fitting error. The noise can be seen in the figure as an oscillation superimposed on the signal and is believed to be a resonant *ringing* of the transducer which is set off by the passage of the shock wave approximately 300 micro-sec before the vortex arrives (see Appendix E). The asymmetry of the pressure signal is possibly due to the changing conditions of the vortex during the time interval ≈ 50 micro-sec during which the signal is recorded. If this is the case, then the curve fitting would then result in finding a pressure distribution which represents an average condition during this time interval. In order to check the degree-of-change of the vortex structure during this 50 micro-sec time interval, the cubic-spline-fit interpolations of the density data from Experiments #16 and #17 are plotted together for comparison and the RMS value of the deviation Δ between the two density curves is given by (see Appendix H, Figure H.15)

$$\Delta = \frac{\rho_{17}(r) - \rho_{16}(r)}{\rho_{16}(r)} = 2.0\% \; .$$

Suitability of Modified Cauchy Function to Represent Pressure Data

The asymptotic behavior of the modified Cauchy function given by

$$P(r) = P_{\infty} - \frac{\Delta P}{1 + \left(\frac{r}{\Delta r_P}\right)^2}$$

is found by taking the limit as $r \to \infty$, and can be written in the form

$$P(r) = P_{\infty} - \frac{G}{r^2} \; ,$$

where G is a constant given by

$$G = \Delta P \left(\Delta r_P\right)^2 .$$

If G is defined by

$$G = \Delta P \left(\Delta r_P\right)^2 \equiv \frac{1}{2}\rho K^2 ,$$

where K is the vortex strength (defined in Chapter 1), then the pressure in this limit becomes

$$P\left(r\right) = P_\infty - \frac{1}{2}\frac{\rho K^2}{r^2} ,$$

which is identical to the theoretical pressure field of the incompressible inviscid vortex calculated in Section 1.3.1, Chapter 1. At large values of r, the vortex density gradient vanishes and thus, the compressible vortex resembles an incompressible vortex in this region. By this logic, the pressure distribution of the compressible vortex is expected to behave similarly to that of an incompressible vortex in the asymptotic limit of large r; and thus, the modified Cauchy function has been chosen as a suitable formula for representing the radial pressure distribution. A curve fitting procedure is used (see Appendix E) to find the values of the arbitrary constants of the formula to satisfy a best-fit condition to the data.

Test of Pressure Data for Homentropic Relationship

The vortex is highly evacuated at the center and the pressure and density ratios at ($t \approx 500$ micro-sec) are given by

$$\frac{P_\infty}{P_\infty - \Delta P} = 3.4$$

and

$$\frac{\rho_\infty}{\rho_\infty - \Delta\rho} = 2.5 .$$

It is of interest at this point to find a simple relationship between the pressure and the density inside the vortex.
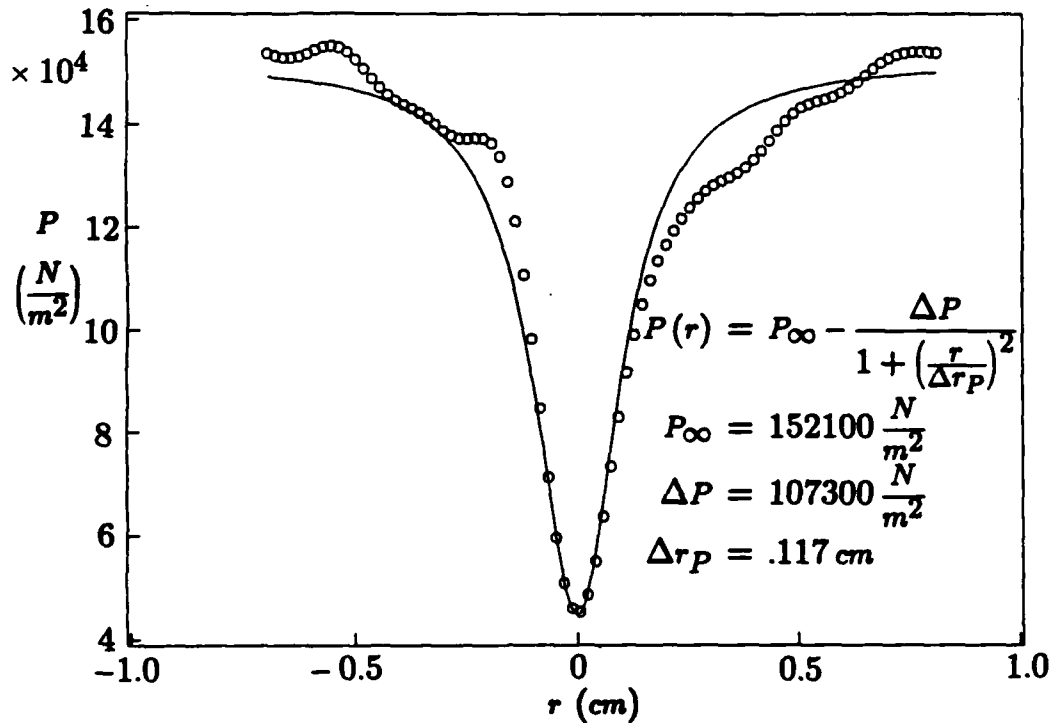
Figure 3.9: Radial Pressure Distribution of Vortex (Best-Fit Curve to Deconvolved Pressure Data).

The solid curve shown in Figure 3.10 represents the best-fit of a curve of a different form to the same pressure data. Here, the density distribution from Experiment #16 (shown in Figure 3.1) is used to define the power-law relationship

$$P(r) = c\rho^{\gamma} ,$$

where $\gamma = 1.4$. This particular relationship represents the well-known homentropic relation between ρ and P. A closeness-of-fit test reveals an RMS deviation of the residuals to be 11107 N/m^2, which when normalized with respect to the well-depth parameter $\Delta P = 107,300$ N/m^2, becomes 10.4% (see Appendix E, Tables E5→E6). The fit in this case is not as good as the modified Cauchy function fit shown in Figure 3.9, which suggests that a homentropic condition does not exist inside the vortex.
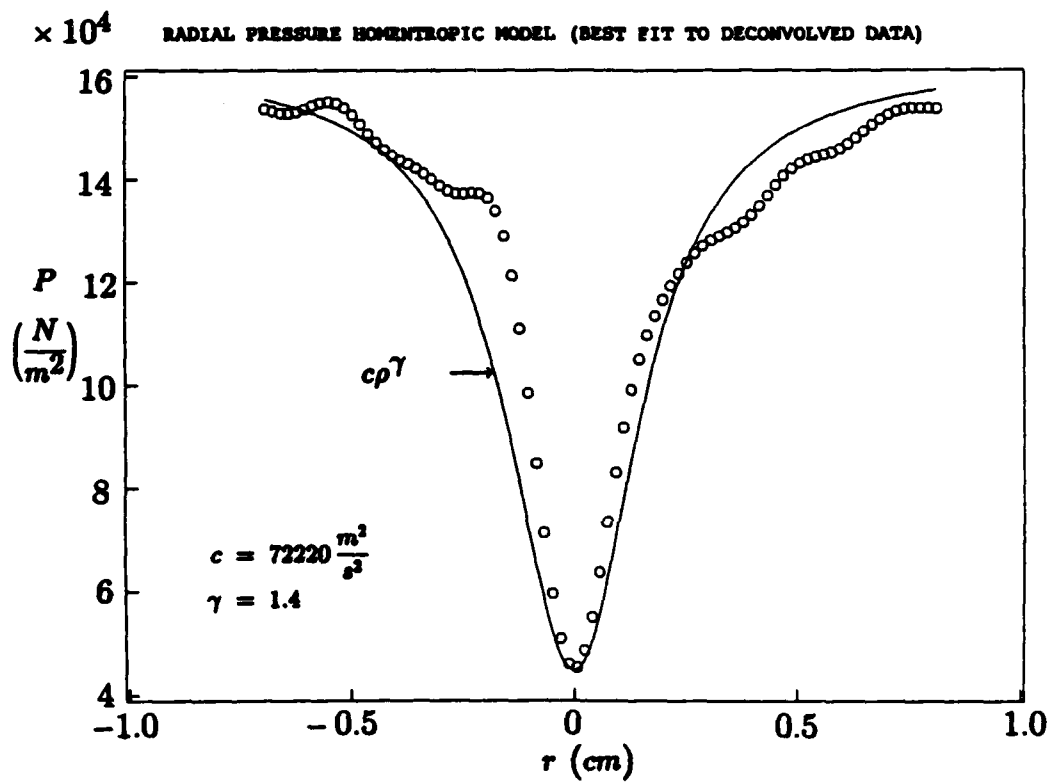
Figure 3.10: Testing of Pressure Data for Homentropic Condition.

Chapter 4

Empirical/Theoretical Analysis

4.1 Analytical Procedures

4.1.1 The Empirical Models

The empirical results from Chapter 3 are utilized, along with the Thermal Equation of State, the Continuity Equation and the equations of motion, to calculate other physical properties of the vortex. The empirical information, as described in Chapter 3, is available in several forms which are summarized below:

- *Raw Density Data:* A sequence of 14 independent *instantaneous* radial density profiles of vortex at $\approx$ 50 micro-sec intervals. Each of these profiles are made up of $\approx$ 35 data points representing discrete values of density at different locations along the diameter of the vortex which correspond to the interferogram fringe locations. This is the raw form of the density measurements which are obtained by the evaluation of the interferograms.

- *Raw Pressure Data:* A single independent radial pressure profile of the vortex. This profile contains 85 data points sampled at equally spaced time intervals from the pressure-time response signal. The measured velocity of the vortex center allows the transformation of the data into a radial pressure profile of the vortex corresponding to a vortex age of ≈ 500 micro-sec. These 85 discrete values of pressure, equally spaced across the diameter of the vortex (at $t \approx 500$ micro-sec), constitute the raw form of the pressure data (see Appendix E).

- *Time-Independent Empirical Density Models:* 14 best-fit curves to the 14 independent raw density data sets as described above. This provides a compact mathematical expression to represent each radial density profile of the vortex at the discrete intervals of time defined by the vortex age in each interferogram (≈ 50 micro-sec apart).

- *Time-Dependent Empirical Density Model:* A single mathematical expression which represents the continuous time and radial dependence of the vortex density. This is a best-surface fit to the complete time-dependent density data set provided by the interferograms.

- *Time-Independent Empirical Pressure Model:* A single best-fit curve to the pressure data after it has been corrected by the deconvolution process. This provides a compact mathematical expression to represent the radial pressure profile of the vortex at $t \approx 500$ micro-sec.

4.1.2   The Calculations

Additional physical properties of the vortex can be investigated in a straightforward manner by use of the information described above in the governing equations. The distribution of the temperature and of both components of the internal velocities inside the vortex is first calculated. Knowledge of both the radial and circumferential components of velocity inside the vortex, along with the density information, allows magnitude calculations of the terms of

the equations of motion (Equations 1.2 and 1.3) to be performed. The investigation of the relative importance of diffusive and convective terms under these flow conditions leads to more general conclusions about the effects of viscosity and compressibility on the vortex internal physical structure and behavior. The following procedures are used for the calculations:

- The single pressure profile that has been measured corresponds to a vortex of a specific age ($t \approx 500$ micro-sec) and this information along with the corresponding density profile (Experiment #16) is used to calculate additional properties of the vortex for this particular time. The pressure and density data at $t \approx 500$ micro-sec is used in both the raw discrete form and the analytical form as described above to calculate the following:

  (a) The radial temperature profile $T(r)$ for $t \approx 500$ micro-sec is calculated with the aid of the Thermal Equation of State

  $$P(r) = \rho(r) RT(r) . \qquad (4.1)$$

  (b) The radial distribution of circumferential velocities $v_\phi(r)$ for $t \approx 500$ micro-sec is calculated with the aid of the modified form of the Radial Momentum Equation

  $$\frac{1}{\rho(r)} \frac{\partial P(r)}{\partial r} = \frac{v_\phi(r)^2}{r} , \qquad (4.2)$$

  in which the unsteady term, the radial convective acceleration term and the normal stress term have been neglected (see Section 4.2.4).

  By use of both forms of the data, the results of the above calculations are then compared to check the validity of the empirical models.

- The time-dependent empirical density model is used alone to calculate the time-dependent radial distribution of the radial velocities $v_r(r, t)$ with the aid of the Continuity Equation

  $$\frac{\partial \rho(r, t)}{\partial t} + \frac{1}{r} \frac{\partial}{\partial r} (r \rho v_r(r, t)) = 0 , \qquad (4.3)$$

where the center of the vortex is considered an inertial frame of reference. A solution for $v_r(r,t)$ is in turn found with the aid of MACSYMA, a symbolic computer program which solves differential equations (see Appendix G).

4.2 Analytical Results

4.2.1 Calculation of $T(r)$

Raw Data Calculation of $T(r)$

From the results for the pressure and the density at a point, Equation 4.1 allows the calculation of a corresponding temperature. The pressure information used in this initial calculation of temperature is shown in Figure 4.1. The figure shows a solid line, the latter is a spline-fit to the sampled data points taken from the original time response of the pressure gauge, in order to interpolate pressure values at the same radial distances corresponding to those of the density data shown in Figure 4.2. This density data and the corresponding interpolated pressure data (just described) is tabulated in Appendix K, Tables K.1 and K.2. These data represent the pressure and density profiles of the vortex at $t \approx 500$ micro-sec. In order to test for an isothermal (linear) relationship between the density and the pressure inside the vortex, it is necessary to find a scale factor which allows the two data sets ($\rho(r)$ and $P(r)$) to collapse into a single curve. A *best-fit* evaluation of a scale factor c_1 is summarized in Appendix K (Table K.1), and gives the RMS value of the residuals

$$RMS\,[P - c_1\rho] = 7582\,N/m^2\ ,$$

which characterizes the degree of overlap between the values of the pressure and the rescaled density. When normalized with respect to the well-depth ΔP

$\times 10^4$
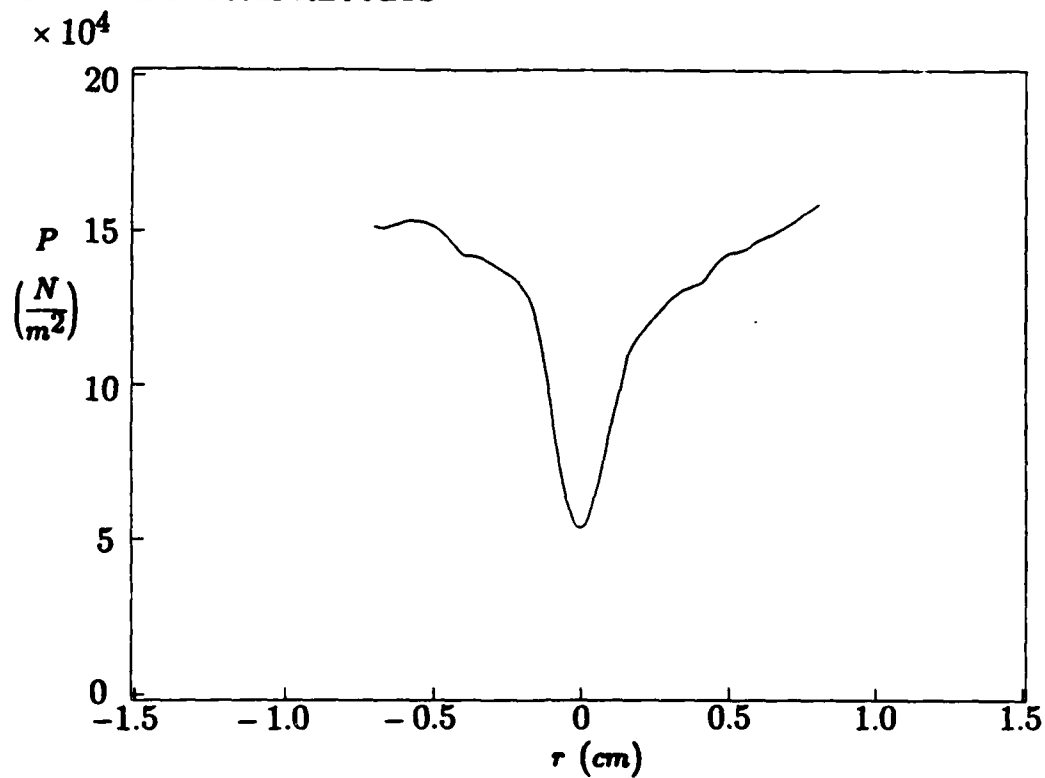
Figure 4.1: Spline-Fit to Raw Pressure Data ($t \approx 500$ micro-sec).
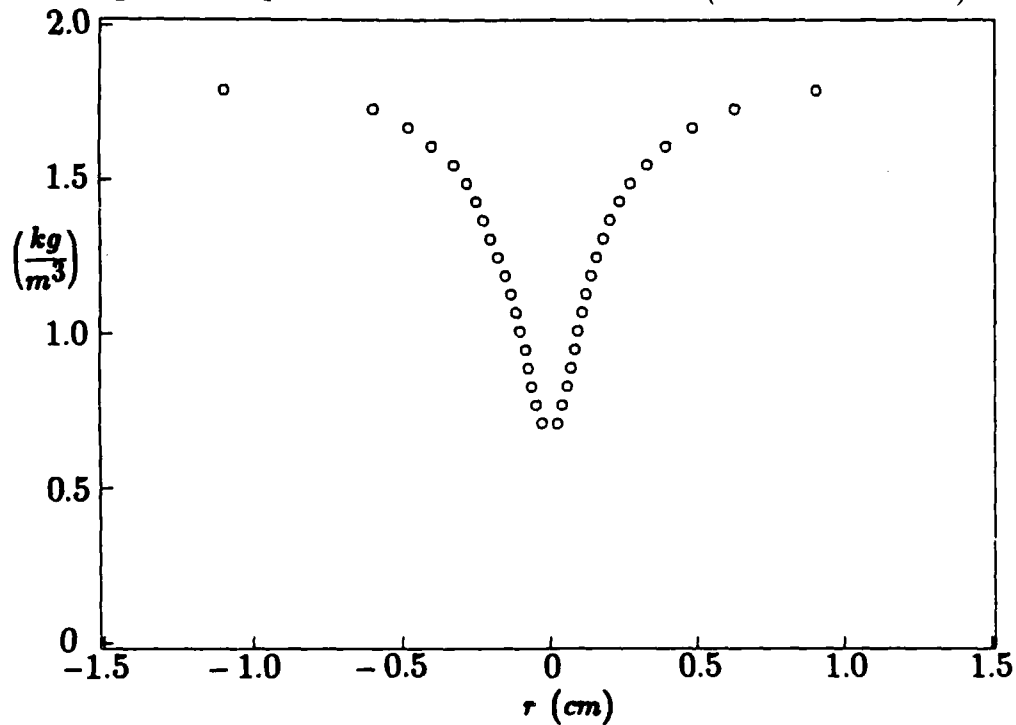
Figure 4.2: Density Data from Interferogram #16 ($t \approx 500$ micro-sec).
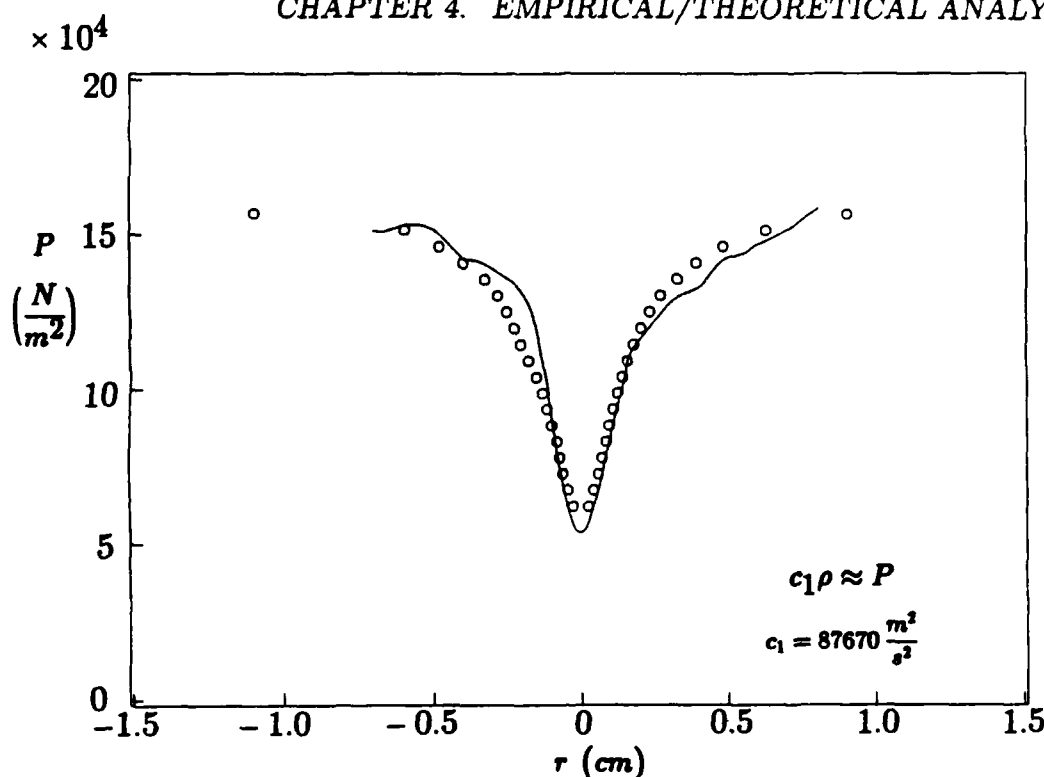
Figure 4.3: Rescaled Density Data Superimposed on Pressure Plot.

(see Figure 3.9, Chapter 3), the RMS deviation becomes 7.1%. The scale factor c_1 permits the density data to be superimposed on the same pressure plot as shown in Figure 4.3. Note that if these data overlapped completely, then the vortex would be isothermal, in accordance with the Thermal Equation of State.

The calculation of the temperature is represented by the discrete values plotted in Figure 4.4 at locations corresponding to those of the density measurements. The temperature values are given in Appendix K, Table K.2.

Calculation of $T(r)$ Using Time-Independent Empirical Models

The empirical models used for the calculation of a continuous temperature distribution are shown in Figures 4.5 and 4.6. The values of the three free parameters that constitute a best-fit condition to the data in each case are given in Figures 3.1 and 3.9 in Chapter 3. Again, Equation 4.1 is used to calculate the temperature, but in this case the result is a mathematical

VORTEX RADIAL TEMPERATURE PROFILE CALCULATED FROM RAW DATA

$$T = \frac{P}{\rho R}$$

$T(r = -.59\ cm)\ =\ 308\ degrees\ K$

$T(r = -.10\ cm)\ =\ 357\ degrees\ K$

$T(r = 0)\ =\ 278\ degrees\ K$

$T(r = .140\ cm)\ =\ 304\ degrees\ K$

$(r = .628\ cm)\ =\ 298\ degrees\ K$
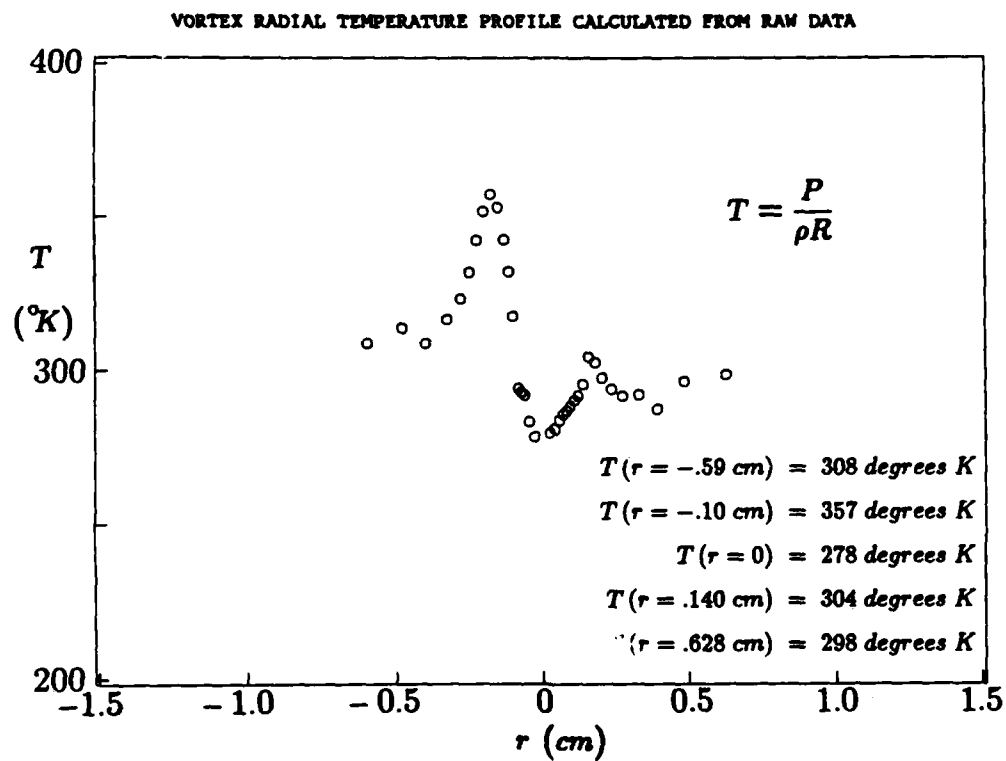
Figure 4.4: Vortex Radial Temperature Calculated From ρ and P ($t \approx 500$ micro-sec).
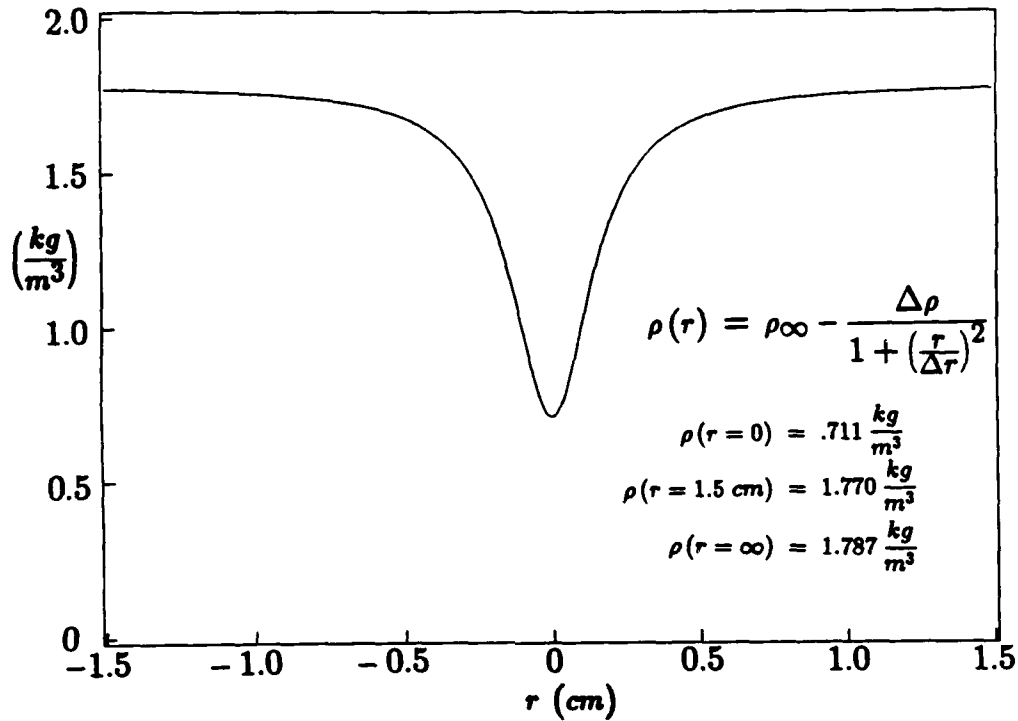
Figure 4.5: Vortex Density Empirical Model $\rho(r)$ ($t \approx 500$ micro-sec).

expression instead of the discrete numerical values obtained in the previous calculation. The results of this calculation are given in Figure 4.7.

Comparison and Discussion of Temperature Results

The results from the two previous calculations of temperature are superimposed on the same plot in Figure 4.8 for the purpose of comparison. The calculation using the symmetrized curve fit models results in an axially-symmetric temperature distribution, whereas, in the raw-data calculation, the asymmetry of the original density and pressure data shows up in the calculation of temperature. As can be seen in Figure 4.8, the results of both calculations reveal the same characteristic temperature peak at $r \approx 1.5$ mm. Also both calculations show a sharp temperature drop at the center of the vortex ($r = 0$). Note how the asymmetry in the temperature points appears to be *magnified* relative to the original density and pressure asymmetries. This is an effect of combining the asymmetrical components of both the density and pressure in

$\times 10^4$

P $\left(\dfrac{N}{m^2}\right)$

$P(r) = P_\infty - \dfrac{\Delta P}{1 + \left(\frac{r}{\Delta r_P}\right)^2}$

$P(r = 0) = 44800 \dfrac{N}{m^2}$

$P(r = 1.5\ cm) = 151447 \dfrac{N}{m^2}$

$P(r = \infty) = 152100 \dfrac{N}{m^2}$

$r\ (cm)$
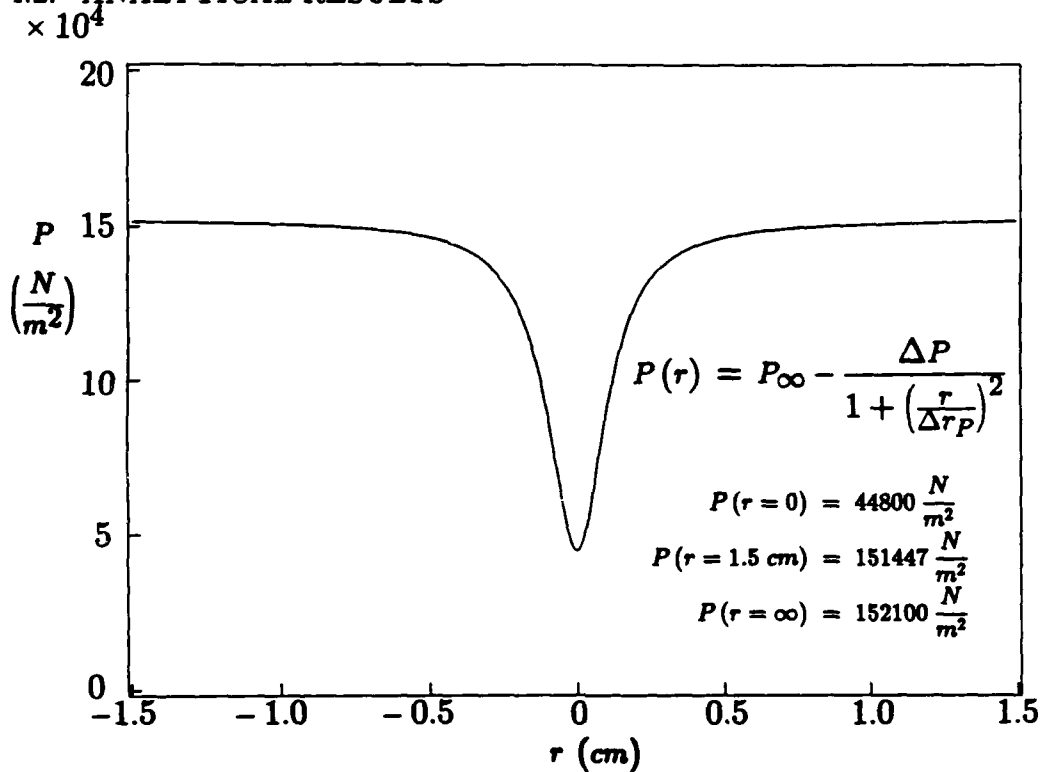
Figure 4.6: Vortex Pressure Empirical Model $P(r)$ ($t \approx 500$ micro-sec).

T $(°K)$

$T(r) = \dfrac{1}{R}\left[\dfrac{P_\infty - \frac{\Delta P}{1+\left(\frac{r}{\Delta r_P}\right)^2}}{\rho_\infty - \frac{\Delta \rho}{1+\left(\frac{r}{\Delta r}\right)^2}}\right]$

$T(r = 0) = 220\ degrees\ K$

$T(r = .15\ cm) = 325\ degrees\ K$

$T(r = 1.5\ cm) = 297\ degrees\ K$

$r\ (cm)$
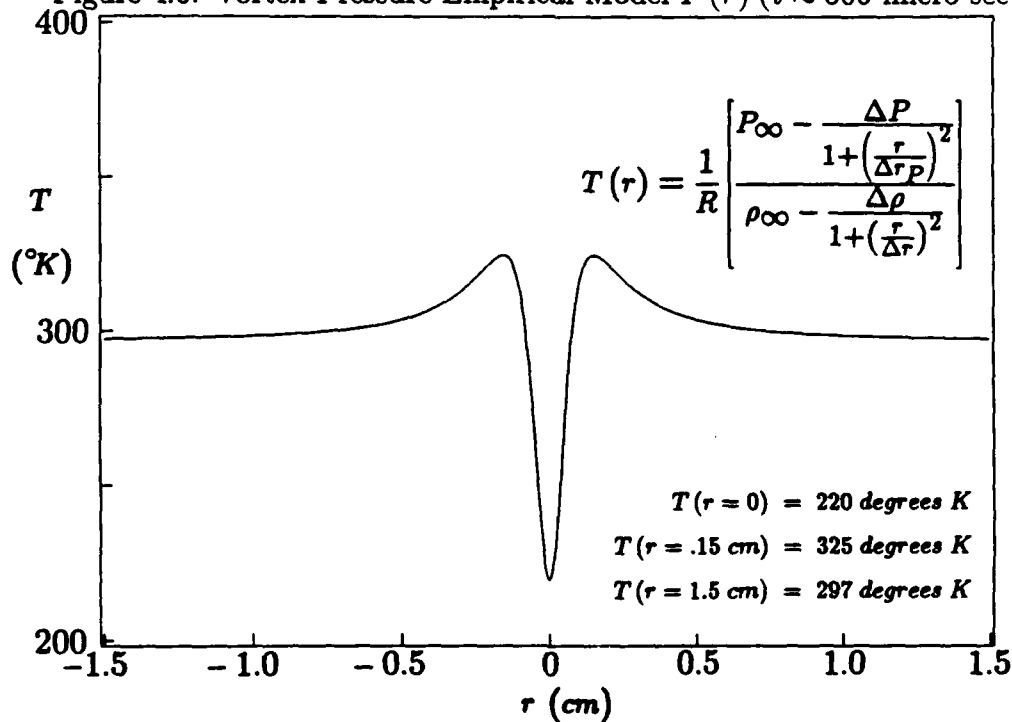
Figure 4.7: Vortex Temperature $T(r)$ Calculated From Empirical Models ($t \approx 500$ micro-sec).
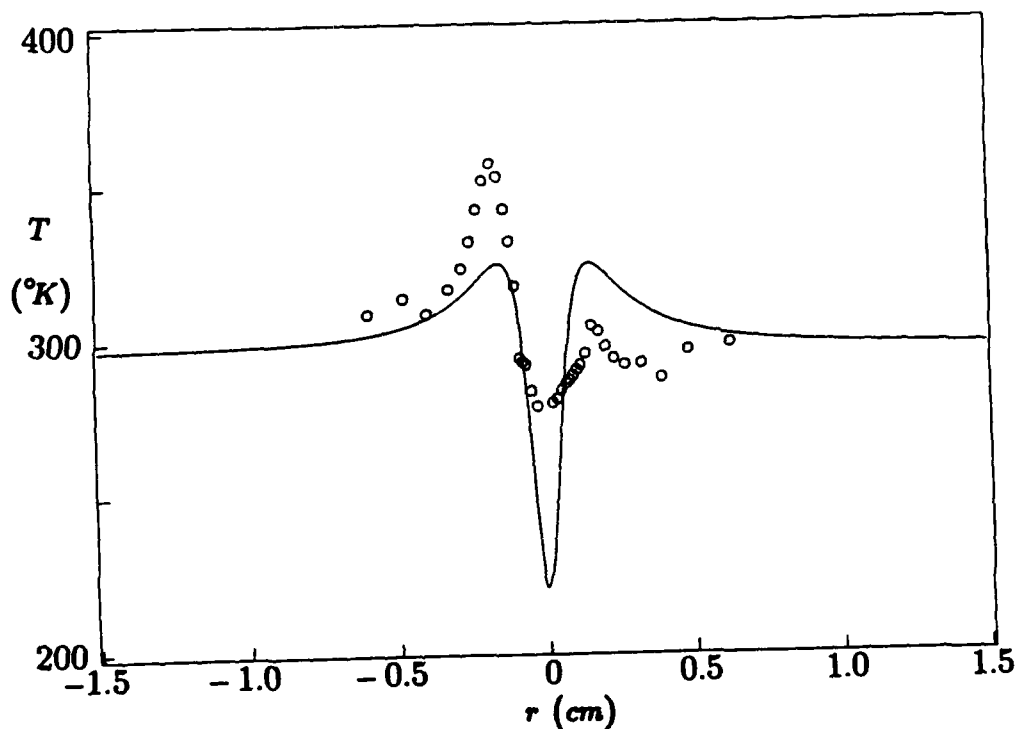
Figure 4.8: Comparison of Vortex Temperature Results $T(r)$.

the calculation of temperature.

4.2.2   Calculation of $v_\phi(r)$

Raw Data Calculation of $v_\phi(r)$

The calculation of $v_\phi(r)$ using Equation 4.2 in the form

$$v_\phi(r) = r \left[\frac{1}{\rho(r)r} \frac{\partial P(r)}{\partial r} \right]^{\frac{1}{2}} , \qquad (4.4)$$

obviously requires numerical values for the pressure gradient $\partial P(r)/\partial r$. By use of the discrete values of pressure data in the form that are equally spaced in r (see Appendix K, Table K.2), a numerical finite difference operation yields suitable approximations of $\partial P(r)/\partial r$. This was done by calculating the first-difference values $\Delta P_i = P_{i+1} - P_i$ and then dividing by the spatial interval Δr which is the same for all the points. The results of this approximation are
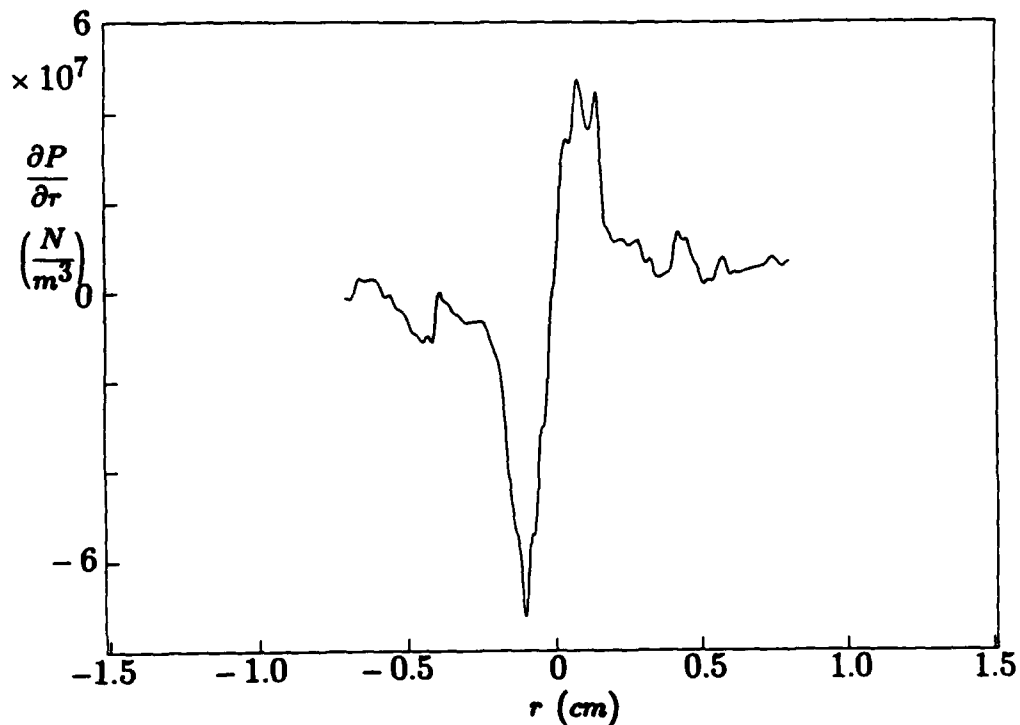
Figure 4.9: Approximation of Vortex Radial Pressure Gradient $\partial P(r)/\partial r$.

given in Appendix K, Table K.2 and are plotted in Figure 4.9. The solid line in Figure 4.9 is a spline-fit curve to the calculated values which are also equally spaced points (note: points not shown in figure). As in the temperature calculation, this spline-fit to the equally spaced points permits interpolated values of the function to be found which correspond to the discrete density data points (which are not equally spaced). In this way, the r-coordinates of the data-pairs: density and pressure gradient, correspond to the radial positions of the fringes of Interferogram #16 and the calculation of $v_\phi(r)$ at these same points can be performed using Equation 4.4. The results of this calculation are given in Appendix K, Table K.2; and in Figure 4.10.

Calculation of $v_\phi(r)$ Using Time-Independent Empirical Models

Figure 4.11 shows the results of the calculation of $v_\phi(r)$ by substitution of the time-independent empirical models of density and pressure as given in Figures 4.5 and 4.6 into Equation 4.4. This calculation reveals a maximum velocity
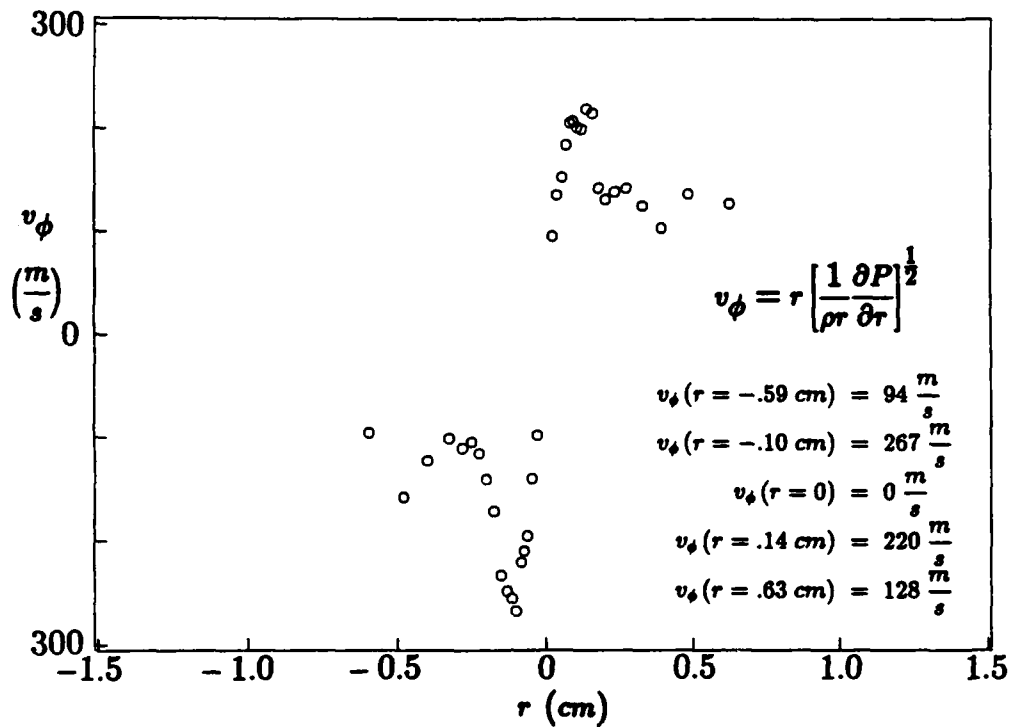
Figure 4.10: Vortex Circumferential Velocity Distribution $v_\phi(r)$ As Calculated From Raw Data.

$v_{\phi max} = 229$ m/sec at a radius of .93 mm. Note, that v_ϕ is with respect to the vortex center. The velocity increases almost linearly from zero (at r=0) to this maximum value; a behavior which closely resembles that of *rigid body rotation*. This region of the vortex is defined as the *core* and has an associated core radius given by $r_{core} = .93$ mm. In Figure 4.12, the results are given of a calculation of the curl of the circumferential velocity, which is defined as the vorticity. This vorticity distribution rapidly drops to zero outside the core of the vortex which shows the irrotational character of the vortex in this outer region.

Calculation of $v_\phi(r)$ Using Incompressible Model

At this point it is instructive to attempt to fit the curve of Lamb's incompressible viscous model of a vortex to the present compressible results as given in

$$v_\phi = \frac{\left(\frac{r}{\Delta r_p}\right)}{1 + \left(\frac{r}{\Delta r_p}\right)^2}\left[\frac{2\Delta P}{\rho_\infty - \frac{\Delta\rho}{1+\left(\frac{r}{\Delta r_\rho}\right)^2}}\right]^{\frac{1}{2}}$$

$$v_\phi(r = 0) = 0\,\frac{m}{s}$$
$$v_\phi(r = .09\,cm) = 229\,\frac{m}{s}$$
$$v_\phi(r = 1.5\,cm) = 27\,\frac{m}{s}$$
$$v_\phi(r = \infty) = 0\,\frac{m}{s}$$
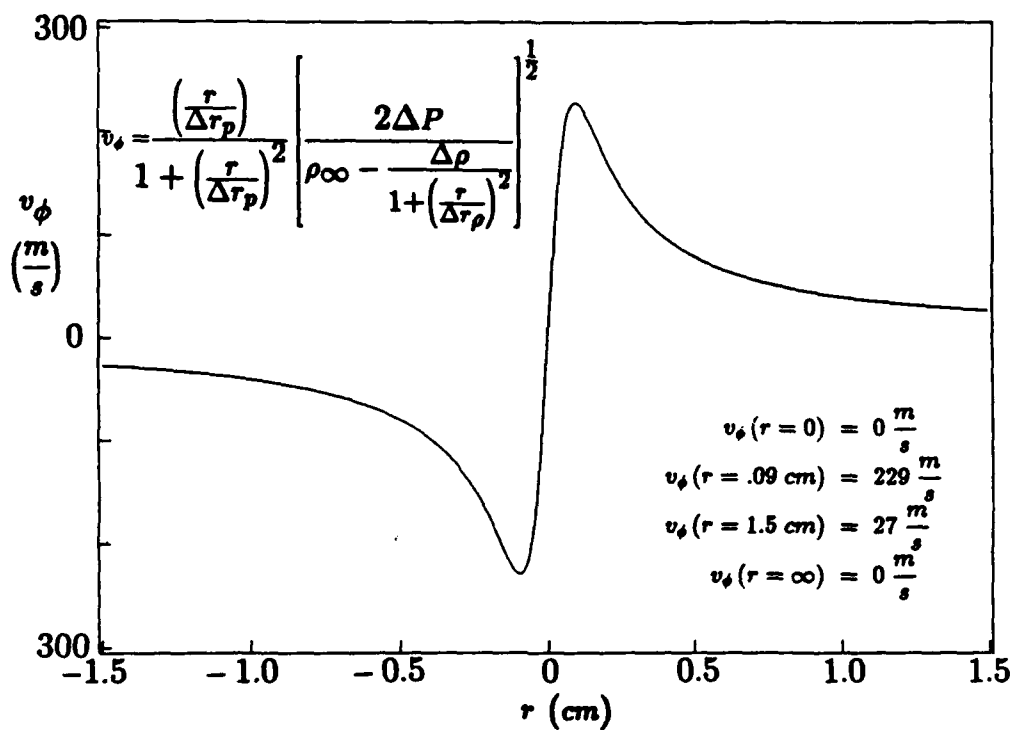
Figure 4.11: Vortex Circumferential Velocity Distribution $v_\phi(r)$ As Calculated From The Time-Independent Empirical Models.

$$\Omega(r) = \frac{1}{r}\frac{\partial}{\partial r}[v_\phi r]$$
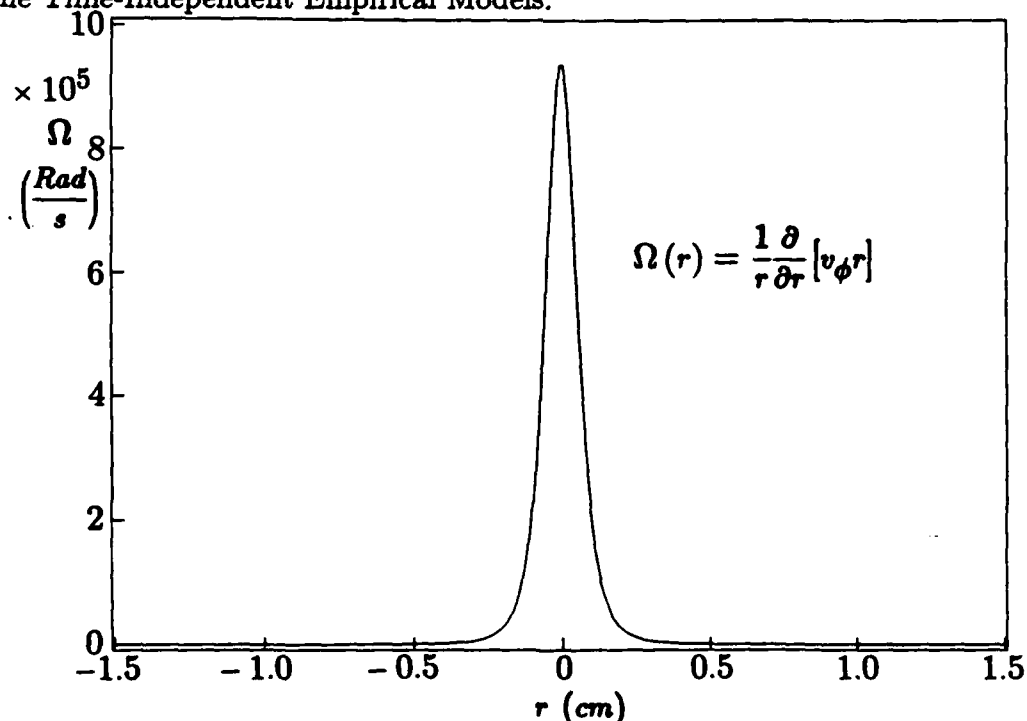
Figure 4.12: Vortex Vorticity Distribution $\Omega(r)$ As Calculated From $v_\phi(r)$.
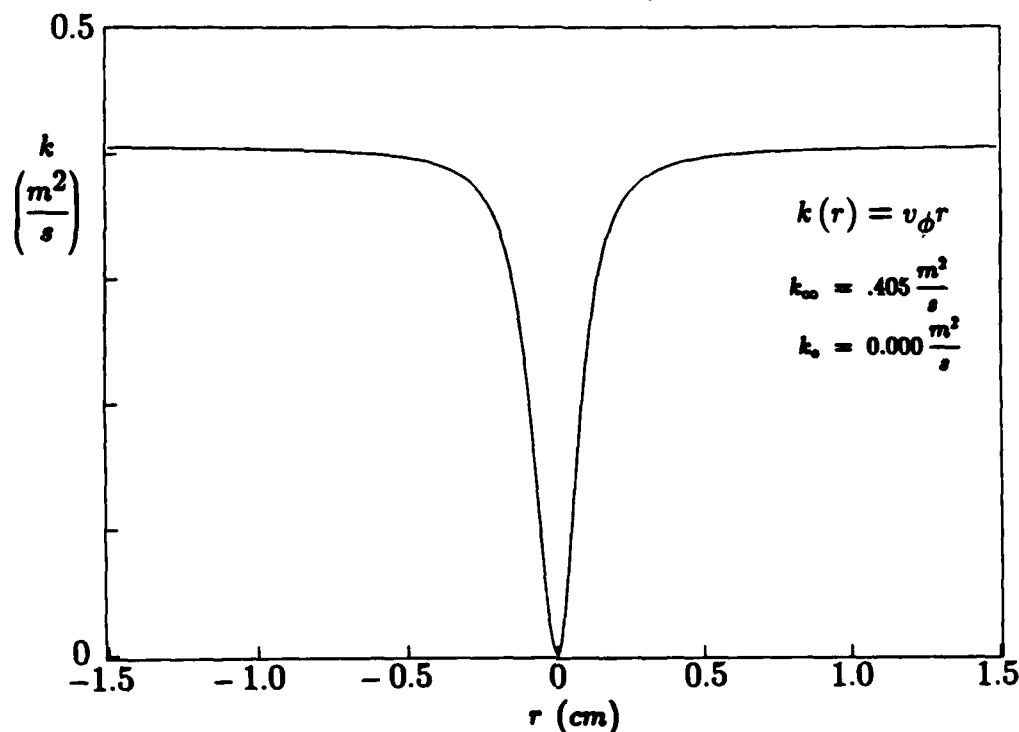
Figure 4.13: Radial Distribution of Vortex Strength $k(r)$ at t=500 micro-sec.

Figures 4.10 and 4.11. Lamb's model (see Section 1.3.1) is given by

$$v_\phi(r,t) = \frac{k}{r}\left(1 - e^{-\frac{r^2}{4\nu t}}\right) , \qquad (4.5)$$

where k (the vortex strength) and ν (the kinematic viscosity) are considered constant parameters. In this case, both the vortex strength and the kinematic viscosity are functions of t and r, and must be redefined as follows:

$$k(r,t) = rv_\phi(r,t) \qquad (4.6)$$

$$\nu(r,t) = \frac{\mu(r,t)}{\rho(r,t)} . \qquad (4.7)$$

The time t for Equations 4.6 and 4.7 is fixed at t=500 micro-sec using the values of $v_\phi(r, t = 500\,\mu s)$ and $\rho(r, t = 500\,\mu s)$ as given in Figures 4.6 and 4.11. Figures 4.13 and 4.14 show the results of the calculations giving the distributions of vortex strength and kinematic viscosity of the vortex at t=500 micro-sec. Each of the plots in Figures 4.13 and 4.14 are characterized by the values of the functions at $r = 0$ and $r = \infty$ given by k_o, k_∞, ν_o and
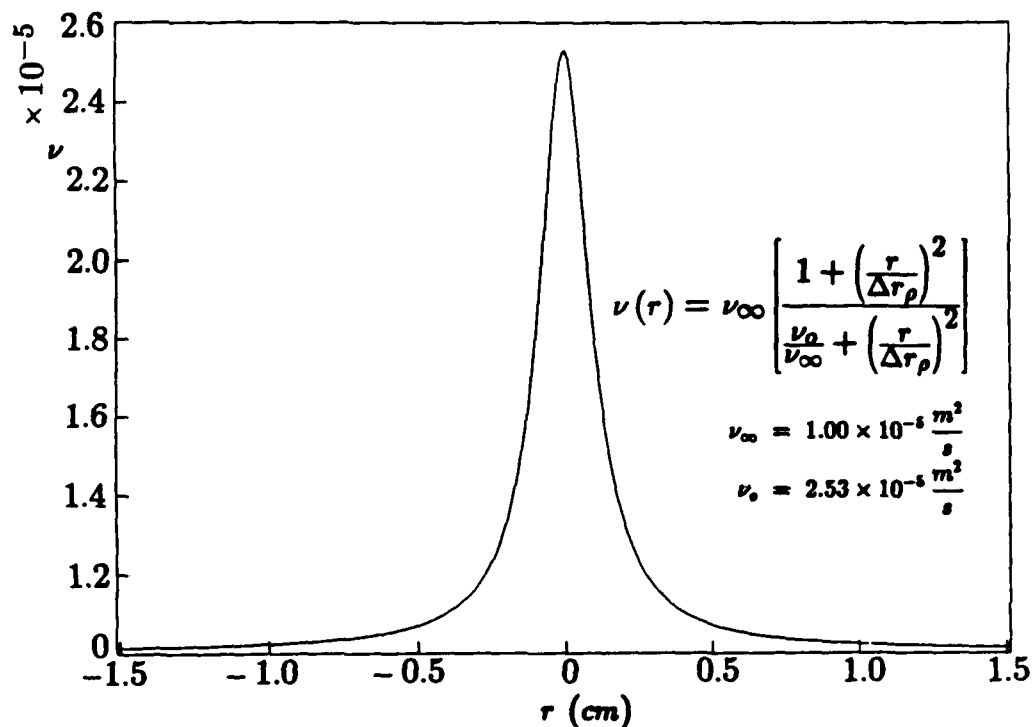
Figure 4.14: Radial Distribution of Kinematic Viscosity $\nu(r)$ at t=500 micro-sec.

ν_∞. Near the center of the vortex, the density gradient is large; and thus, compressibility effects are present in this region. Far from the center of the vortex, the effects of compressibility are negligible; and so the values picked to be used for the constants k and ν in Equation 4.5 are k_∞ and ν_∞. This leaves only one free parameter t in Equation 4.5 which must be determined for the best match to the results in Figure 4.11, i.e., a value of t is to be determined in order to match the maximum velocity of the calculated Lamb model curve with that of the empirically derived curve in Figure 4.11. The solution of Equation 4.5 for t, given the values

$$k_\infty = .405 \, \frac{m^2}{sec}$$

and

$$\nu_\infty = 1.00 \times 10^{-5} \, \frac{m^2}{sec} \, ,$$

yields the value

$$t = 30,000 \, \mu s \, .$$
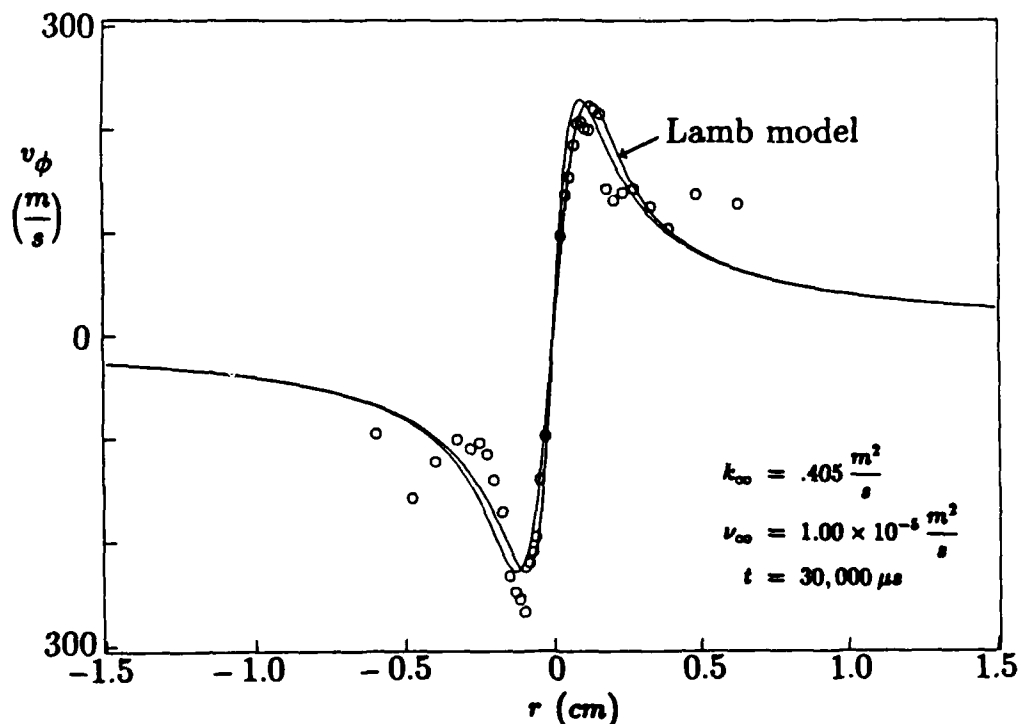
Figure 4.15: $v_\phi(r)$: Comparison of Raw Data Calculation, Empirical Model Calculation and Lamb Model Fit at t=500 micro-sec.

Comparison and Discussion of Circumferential Velocity Results

Figure 4.15 shows the superposition of the results of the three different circumferential velocity calculations as just described in the previous sections. The initial condition of the Lamb vortex is defined by a concentration of the vorticity along the line of the axis, whereas the initial distribution of vorticity of the experimental compressible vortex is determined by the generation process. This difference in initial conditions accounts for the large value of t required in the Lamb model to match the experimental data. The relaxation time t required for the Lamb vortex to decay by diffusion from an irrotational line vortex to one with a viscous core matching that of the experimental conditions, is found to be approximately 30,000 micro-sec. It can be seen in Figure 4.15 that the incompressible Lamb model very closely fits the conditions of the vortex outside the core region (for $r \geq 5$ mm), which is where the effects of compressibility, as determined by inspection of the density function (see

Figure 4.5), are very small. Except for the small component of asymmetry and the scatter (associated with the noise of the pressure signal), there is good overlap of the results of the raw data calculation with the other models.

4.2.3 Calculation of $v_r(r,t)$

The Normalized Continuity Equation

It is convienient to write the Continuity Equation (Equation 4.3) in the following normalized form:

$$\frac{\partial v_r}{\partial r} + v_r \left[\frac{\partial}{\partial r} (\ln \rho^*) + \frac{1}{r} \right] + \left[\frac{\partial}{\partial t} (\ln \rho^*) \right] = 0 . \tag{4.8}$$

This is the form of a first order linear differential equation and can be solved for $v_r(r,t)$ when the function $\rho^*(r,t)$ is known.

The Normalized Empirical Density Formula

From Section 3.1, the normalized density function which describes the radial and time dependence of the normalized vortex density distribution is given by

$$\rho^*(r,t) = 1 - \frac{\Delta \rho_o^* e^{-\frac{t}{\tau}}}{1 + \left(\frac{r}{\Delta r_o + \Theta t}\right)^2} , \tag{4.9}$$

where the constants are defined by

$$\Delta \rho_o^* = .898$$

$$\Delta r_o = .143 \; cm$$

$$\tau = 1325 \; \mu s$$

$$\Theta = 57.2 \; cm/s .$$

This density function is substituted into Equation 4.8, and then a solution of this equation yields the time-dependent radial distribution of the radial component of velocity $v_r(r,t)$.

$$v_r(r,t) = -\frac{(f_1(t)r^2 + f_2(t) + c_1)\ln(r^2 + f_3(t)) + c_2 r^2 + f_4(t)}{f_5(t)r^3 + f_6(t)r}$$
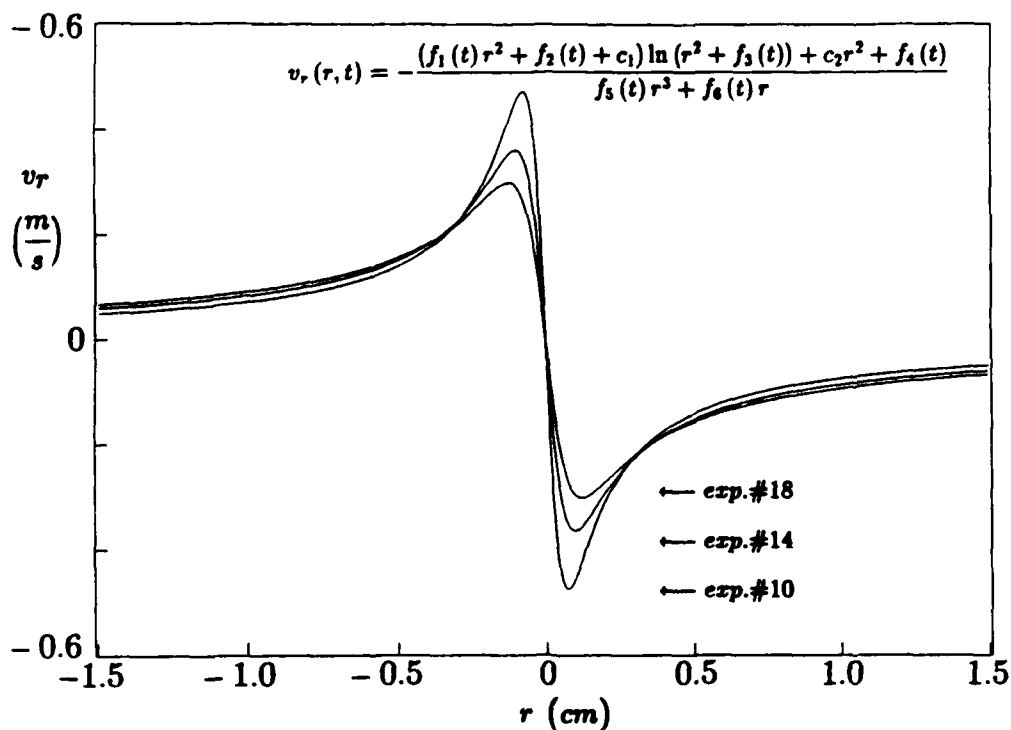
Figure 4.16: Vortex Radial Velocity Profiles $v_r(r,t)$ at Stations #10, #14 and #18 ($\Delta t \approx 200$ micro-sec intervals).

Calculation of $v_r(r,t)$: Solution of the Continuity Equation Using MACSYMA

A solution of Equation 4.8 is found using MACSYMA, a computer program which is capable of finding symbolic solutions of certain forms of ordinary differential equations (see Appendix G). A sample of the results of the MAC-SYMA calculation is given in Figure 4.16, which shows the functional form of the solution $v_r(r,t)$ and also shows three curves generated by this function at specific values of t. In the function shown in Figure 4.16, the dependence on r is shown explicitly and the dependence on t is implicitly given in the six functions $f_i(t)$. The values for the constants c_1 and c_2 are found from the boundary conditions (see Appendix G). The curves in Figure 4.16 show the radial dependence of v_r for the three different cases: t=197, t=401 and t=598 micro-sec (which correspond to Density Experiments #10, #14 and #18).

Discussion of Radial Velocity Results

The three curves in Figure 4.16 represent the radial velocities of the vortex at three different times and correspond to the experimental conditions of Density Experiments #10, #14 and #18 (see density curves in Figure 3.6, Chapter 3). The curves in Figure 4.16 were generated using the information in Tables L.1→L.6, Appendix L. The negative value of v_r indicates that the direction of this component of velocity is *inward*, towards the center. Figure 3.6 in Chapter 3 shows the time dependence of the vortex density which is increasing with time. Associated with this increase of the vortex density, is an inward convection of fluid. The rate of this convection is dependent on the magnitude of v_r, which is observed to be decreasing with time in Figure 4.16. This information on the time behavior of v_r is used in the following section to approximate the magnitude of the unsteady term of the Radial Momentum Equation. Figure 4.17 shows the plot of the vortex radial velocity distribution calculated for t=500 micro-sec (corresponding to Density Experiment #16). The values used to generate the curve in Figure 4.17 are tabulated in Appendix L (see Tables L.7→L.12). This information on the radial dependence of v_r is used in the following section to approximate the magnitudes of both the convection term and the viscous (normal stress) erm of the Radial Momentum Equation. Also, this information is used to evaluate the convection term of the Angular Momentum Equation.

4.2.4   Evaluation of Navier-Stokes Terms

By use of the quantities calculated in the previous sections of this chapter, it is now possible to evaluate the terms of the Radial Momentum Equation and the Angular Momentum Equation as given by the theory of the 2-D axisymmetric compressible free vortex in Section 1.2.1 (Chapter 1).
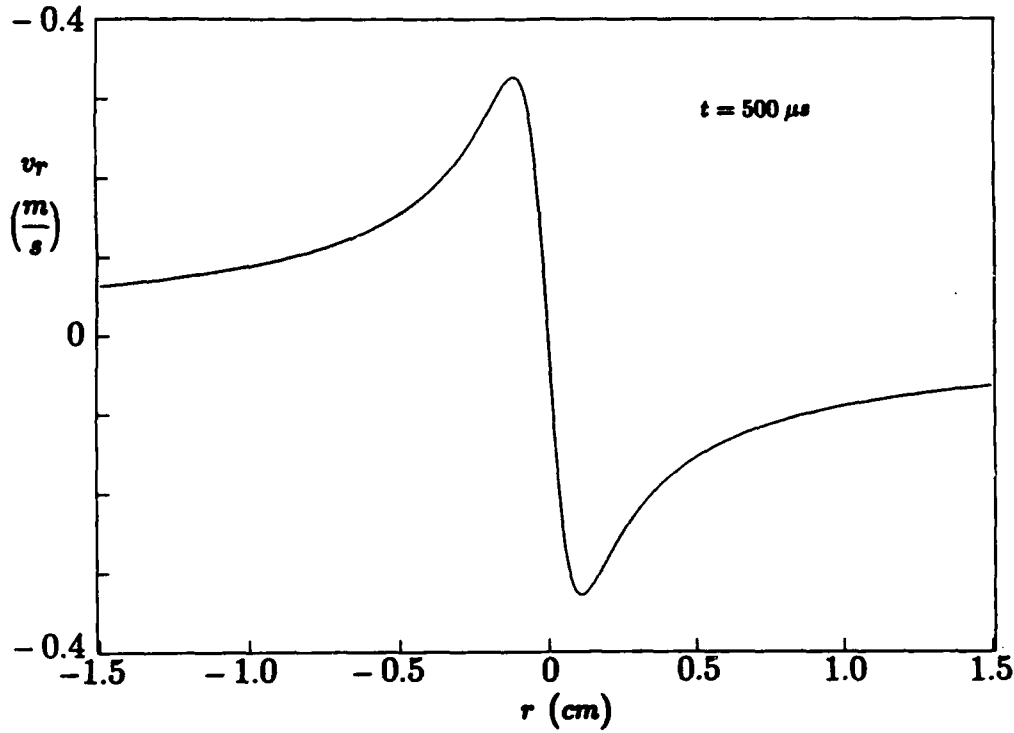
Figure 4.17: Vortex Radial Velocity Profile $v_r\,(r)$ at t=500 micro-sec.

The Radial Momentum Equation

The Radial Momentum Equation (see Equation 1.2) given by

$$\frac{\partial v_r\,(r,t)}{\partial t} + v_r\,(r,t)\,\frac{\partial v_r\,(r,t)}{\partial r}$$

$$+\frac{1}{\rho\,(r,t)}\frac{\partial P\,(r,t)}{\partial r} - \frac{[v_\phi\,(r,t)]^2}{r}$$

$$-\frac{2}{\rho}\left(\frac{\partial}{\partial r}\mu\frac{\partial v_r}{\partial r} + \frac{\mu}{r}\frac{\partial v_r}{\partial r} - \mu\frac{v_r}{r^2}\right) = 0\;, \qquad\qquad (4.10)$$

is written in terms of the four dependent variables:

$$P\,(r,t)$$

$$\rho\,(r,t)$$

$$v_\phi\,(r,t)$$

$$v_r\,(r,t)\;.$$

The first unsteady term in Equation 4.10, namely

$$\frac{\partial v_r(r,t)}{\partial t} ,$$

is neglected in the calculation of $v_\phi(r)$ at t=500 micro-sec (see Section 4.2.2). It is of interest to evaluate the magnitude of the unsteady term in the region of the vortex where the peak velocity v_ϕ occurs (core radius). The calculation of v_ϕ in Section 4.2.2 (see Figure 4.11) gives a value of r=.093 cm for the core radius of the vortex. The magnitude of this term at t=500 micro-sec can be approximated using the information in Appendix L, Table L.4, which gives the values of v_r at r=.095 cm for both t=401 and t=598 micro-sec (see also Figure 4.16). The difference in time t is $\Delta t = 197$ micro-sec and the corresponding difference in v_r is $\Delta v_r = -.07$ m/sec . A finite difference approximation of this term is given by

$$\frac{\Delta v_r}{\Delta t} = -359 \ m/sec^2 .$$

The second term in Equation 4.10

$$v_r(r,t)\frac{\partial v_r(r,t)}{\partial r} ,$$

is a convection term which is also neglected in the calculation of $v_\phi(r)$ at t=500 micro-sec. The magnitude of this term can be approximated using the information in Appendix L, Table L.10, which gives the values of v_r at t=500 micro-sec for r=.085 cm, r=.095 cm and r=.105 cm (see also Figure 4.17). A finite difference approximation of this convection term is then given by

$$v_r(r=.095)\frac{v_r(r=.105)-v_r(r=.085)}{\Delta r} = 16.3 \ m/sec^2 .$$

The third and fourth terms in Equation 4.10 are used in the calculation of $v_\phi(r)$ (Section 4.2.2). The magnitudes of these terms at r=.093 cm can be approximated using the information in Appendix K, Table K.2. Within this table, are the values of ρ, $\partial P/\partial r$ and v_ϕ at r=.096 cm, which are the results of the raw data calculations described in Section 4.2. Evaluation of these terms give

$$\frac{1}{\rho(r,t)}\frac{\partial P(r,t)}{\partial r} = 4.49 \times 10^7 \ m/sec^2$$

and

$$\frac{[v_\phi(r,t)]^2}{r} = 4.52 \times 10^7 \ m/sec^2 \ .$$

The last term in Equation 4.10

$$\frac{2}{\rho(r,t)} \left(\frac{\partial}{\partial r} \mu \frac{\partial v_r(r,t)}{\partial r} + \frac{\mu}{r} \frac{\partial v_r(r,t)}{\partial r} - \mu \frac{v_r(r,t)}{r^2} \right) \ ,$$

is a normal stress term, which is neglected in the calculation of v_ϕ. The magnitude of this term can be approximated by a finite difference method using the same three values of v_r that were employed for the evaluation of the second term above. The density ρ is known (see the evaluation of the third term above) and the kinematic viscosity μ is given by

$$\mu = 1.8 \times 10^{-5} \ m^2/sec \ .$$

From these considerations, a magnitude approximation of the normal stress term yields a value of $.411 \ m/sec^2$.

The above calculations allow comparisons to be made of the relative magnitudes of the terms of the Radial Momentum Equation. One can see from this comparison, that the terms which are neglected in the calculation of v_ϕ in Section 4.2.2, are indeed of little significance in this case.

The Angular Momentum Equation

The Angular Momentum Equation (see Equation 1.3) given by

$$\rho(r,t) r^2 \frac{\partial}{\partial t} \left(\frac{v_\phi(r,t)}{r} \right) + \rho(r,t) v_r(r,t) \frac{\partial}{\partial r} (r v_\phi(r,t))$$

$$- \frac{1}{r} \frac{\partial}{\partial r} \left[r^3 \mu \frac{\partial}{\partial r} \left(\frac{v_\phi(r,t)}{r} \right) \right] = 0 \ , \qquad (4.11)$$

is written in terms of the three dependent variables:

$$\rho(r,t)$$

$$v_\phi(r,t)$$

$$v_r(r,t) \ .$$

The first term in this equation

$$\rho(r,t)\, r^2 \frac{\partial}{\partial t}\left(\frac{v_\phi(r,t)}{r}\right) \ ,$$

is an unsteady term and is in units of angular momentum per unit volume per unit time (or torque per unit volume).

The second term

$$+\rho(r,t)\, v_r(r,t)\, \frac{\partial}{\partial r}\left(r v_\phi(r,t)\right) \ ,$$

is a compressible (convection) term (note that v_r would be zero in an incompressible fluid). This term represents the convection of angular momentum.

The third term

$$-\frac{1}{r}\frac{\partial}{\partial r}\left[r^3 \mu \frac{\partial}{\partial r}\left(\frac{v_\phi(r,t)}{r}\right)\right] \ ,$$

is a viscous (diffusion) term which represents the diffusion of angular momentum.

By setting t=500 micro-sec, one can evaluate the last two terms of Equation 4.11 using the calculated distributions of $v_\phi(r, t = 500\ \mu s)$ and $v_r(r, t = 500\ \mu s)$ from the previous sections; and using the density distribution $\rho(r, t = 500\ \mu s)$ from Experiment #16. These three quantities, plotted in Figures 4.5, 4.11 and 4.17, are replotted for positive values of r in Figures 4.18, 4.19 and 4.20. This information is substituted into the second and third terms of Equation 4.11 and numerical evaluations of these terms are made. After the evaluation of the second and third terms, the first term of Equation 4.11 can then be obtained by the condition that the sum of all three terms must be zero for all values of r. The results of these calculations are shown in Figure 4.21.

The peak values of the three curves in Figure 4.21 occur at $r \approx 0.8$ mm. The peak value of the viscous term is 10.4 $kg/m - sec^2$ and the peak value of the compressible term is -75.9 $kg/m - sec^2$. The peak value of the unsteady term

is found to be 65.5 $kg/m - sec^2$ which satisfies the condition that the sum of all three terms is zero at any point r. The positive value of the viscous term represents the outward viscous diffusion of angular momentum. The negative value of the compressible term represents the inward convection of angular momentum. The positive value of the unsteady term represents a net increase with time of angular momentum per unit volume. The curves in Figure 4.21 reveal the relative magnitudes of the competing effects of outward diffusion and inward convection of angular momentum inside the vortex. Thus, it is revealed in Figure 4.21 that the compressibility of the fluid in this case has a much larger influence than the viscosity on the behavior of the vortex, with the principle feature being a net increase with time of angular momentum per unit volume within the vortex. This growth of angular momentum density with time in the vortex is a primary result of the inward radial convection of fluid v_r, which in turn is only possible in a compressible fluid.

The vortex is in a stage of high compressibility during the first 1325 micro-sec of the vortex lifetime, during which the density variation decreases from its initial value of 9.8 down to a value of 1.5 (see Section 3.1, Chapter 3). Beyond this time, the corresponding inward radial convection of fluid v_r continues to decrease in magnitude as the density variation across the vortex vanishes (see Figure 4.16). A transition point would then be expected at a time t when the compressible term is equal in magnitude to the viscous term, resulting in the unsteady term becoming identically zero. After this transition, the viscous diffusion of angular momentum would then be expected to become the primary process. In this case, the viscous term would then become larger in magnitude than the compressible term and the unsteady term would as a result become negative in sign, which represents a net decrease with time of angular momentum per unit volume.

Summary of Observations

The initial state of the vortex is a result of the generating process. A free vortex is created that is initially highly evacuated and which is in a state of non-equilibrium. The vortex begins to collapse as fluid rushes towards its center. The angular momentum associated with the surrounding fluid is also moved further into the vortex during this collapsing process, which is purely a compressible effect. As a result, the vortex is in a period of compression, and is gaining in both mass density and angular momentum density, with time. The rate of growth of the mass density and the angular momentum density inside the vortex is dependent on the magnitude of v_r, which is decreasing with time as the density variation across the vortex vanishes. Eventually, the viscous effects would become larger in magnitude than the compressible effects as v_r approaches zero, and the vortex would begin to resemble that of a viscous incompressible vortex (see Section 4.2.2). At this point, there would be a transition in the behavior of the vortex as it transforms from a highly compressible vortex (in which the angular momentum density grows with time), to a diffusive vortex (in which the angular momentum density decays with time).
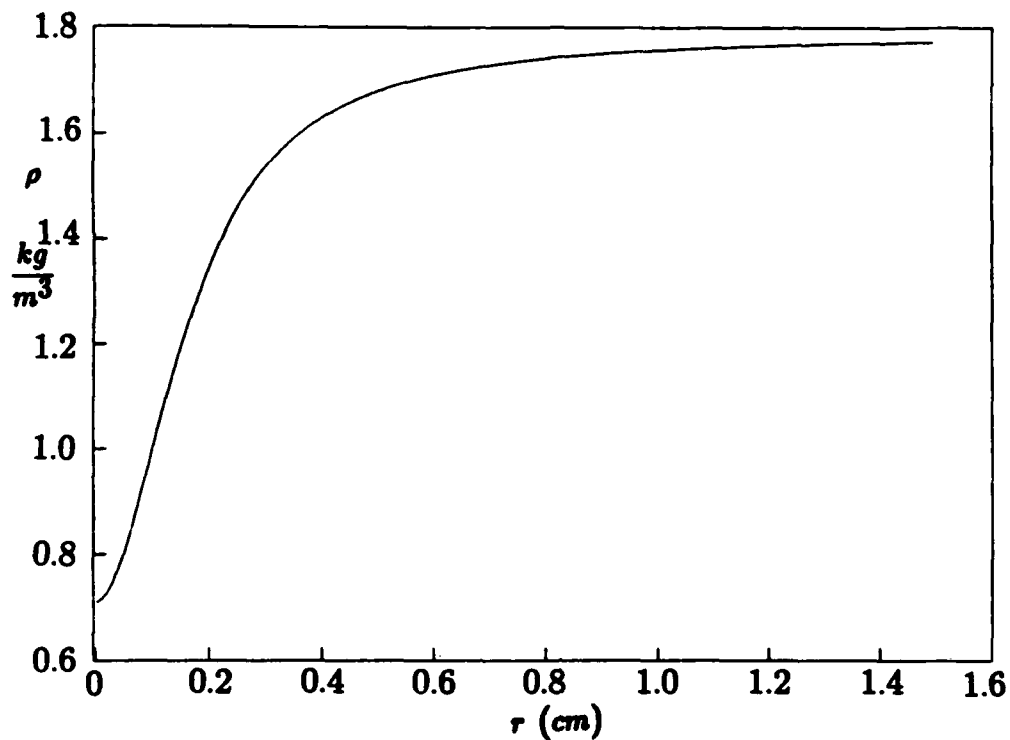
Figure 4.18: Radial Distribution of Vortex Density at t=500 micro-sec.
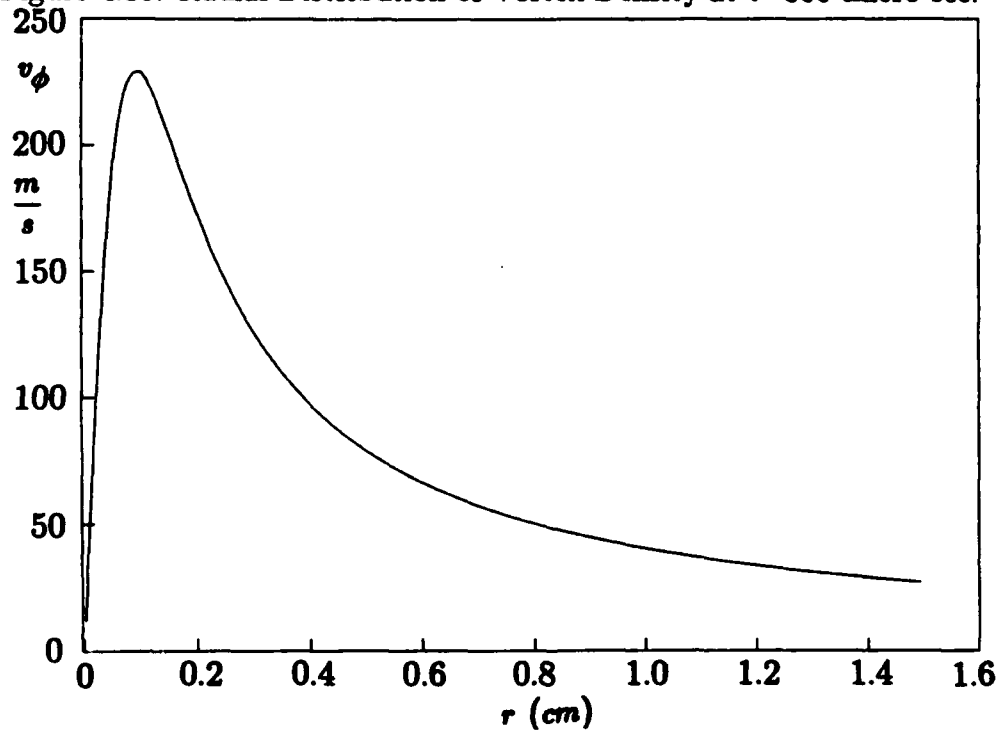
Figure 4.19: Radial Distribution of Vortex Circumferential Velocity at t=500 micro-sec.
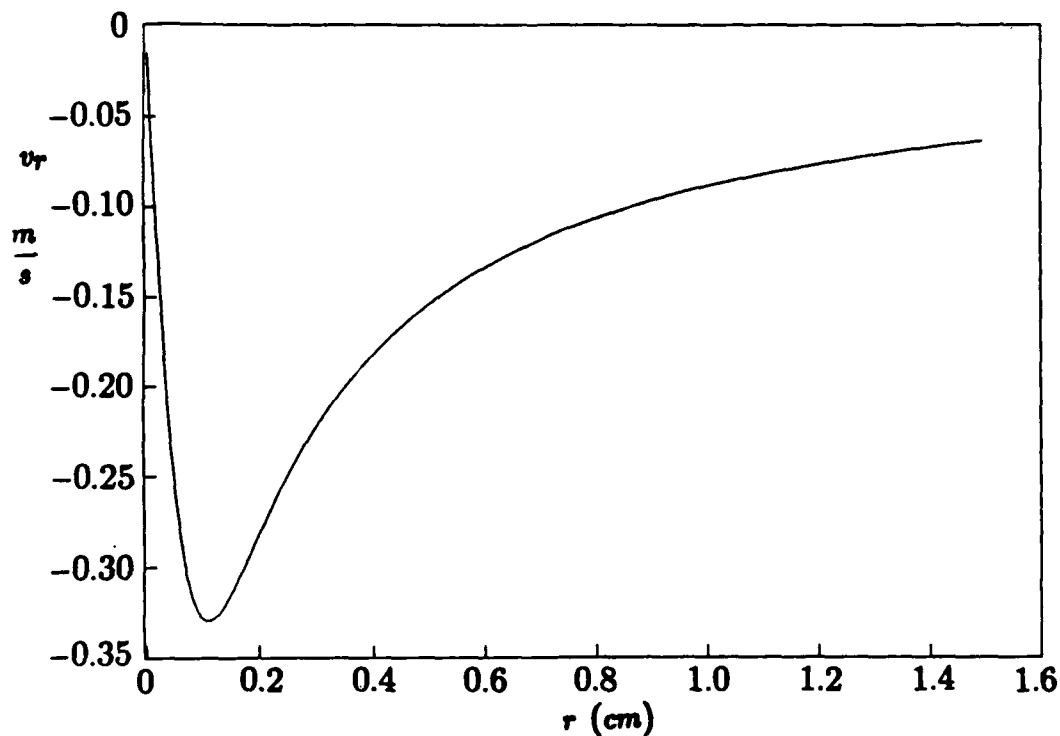
Figure 4.20: Radial Distribution of Vortex Radial Velocity at t=500 micro-sec.
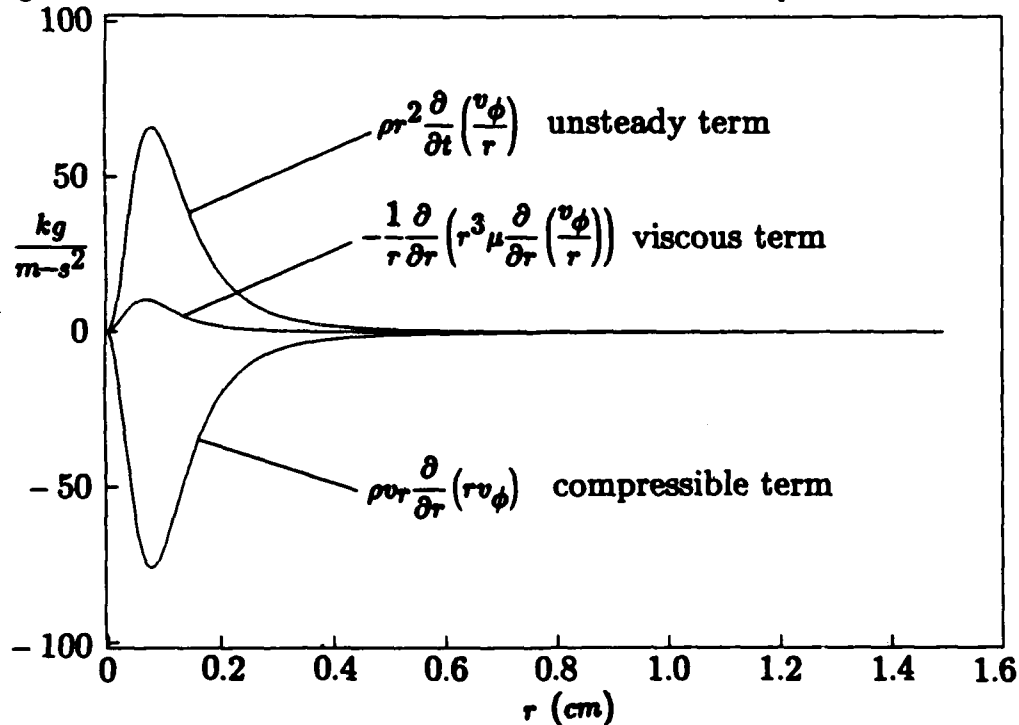
Figure 4.21: Evaluation of the Unsteady, Viscous and Compressible Navier-Stokes Terms.

Chapter 5

Overall Assessment and

Conclusions

As stated in Chapter 1 (Introduction), the objective of this thesis is the measurement and calculation of the various physical properties associated with a traveling compressible vortex, which is generated and convected by shock passage over an airfoil model. The results obtained led to certain observations of the structure and behavior of the vortex, some of which may possibly apply more generally to the description of compressible vortices.

The experimental and analytical results led to several observations of the physical structure and behavior of the vortex as follows:

(a) The measured radial density distribution of the vortex very closely fit a simple mathematical formula, which was a modified form of the well-known Cauchy function. Two parameters with opposing characteristics defined the shape of this density function; namely the well-depth $\Delta\rho$ and half-width Δr.

(b) The magnitude of the well-depth parameter of the density function was observed to decay exponentially with respect to vortex age.

(c) A vortex density radius, defined by the half-width parameter of the density function, was found to be ≈ 1.7 mm.

(d) A similarly defined vortex pressure radius was found to be ≈ 1.2 mm.

(e) A comparison of the conditions at the center of the vortex and at its outer boundary, showed a change in pressure by a factor of 3.4 and a change in density by a factor of 2.5.

(f) The pressures and densities inside the vortex were not found to exhibit a homentropic relationship.

(g) The radial distribution of the circumferential components of the velocities inside the vortex indicated a peak value of $v_\phi \approx 230$ m/sec at $r \approx .9$ mm, which also defined the radius of the vortex core.

(h) The radial distribution of temperature showed a sharp drop in value at the vortex center and a peak value occurred near r_{core}.

(i) The radial distribution of the radial components of the velocities inside the vortex reached a peak value of $\approx .3$ m/sec near r_{core}; and thus, the magnitude of the radial component of velocity was $\approx .1\%$ of the magnitude of the circumferential component.

(j) During the particular stage of the vortex in this study, the effect of compressibility of the fluid on the transport of angular momentum inside the vortex was found to be approximately an order of magnitude larger than the effects due to the viscosity of the fluid. In general, the primary effect of compressibility inside the vortex was an inward convection and subsequent compression of the rotating fluid. Since the transport of angular momentum out of the vortex by the process of diffusion was counteracted by the stronger process of inward convection, then the net effect of these two processes was an increase (with time) of angular momentum density inside the vortex.

The results of the experiments and subsequent analysis provided a physical characterization of the vortex under study in terms of its basic physical

properties and revealed a complex time-dependent internal structure, which is governed by the initial conditions and the competing effects of both compressibility (a convective process) and viscosity (a diffusive process). Some insight into the question of the role and relative magnitude of these effects on the internal structure and behavior of the vortex has been provided by this study and the effect of compressibility is found to be the dominant process of angular momentum transport inside the vortex. A question immediately arises pertaining to the generalization of this observation; namely: Does this behavior reflect the nature of compressible vortices in general? Also, the role of compressibility and viscosity on the transport of energy inside the vortex is still an open question. Lastly, the remarkable closeness-of-fit of a simple mathematical formula to the density data raises the question of the generality and physical significance of this empirical law.

Many new questions have been raised as a result of the observations in this study. In this vain, suggestions for extending this study in directions that may shed light on some of these questions are given in the following remarks.

Transport of Angular Momentum Inside Vortex

The primary conclusions of this study were based on the calculated relative magnitudes of the convective and diffusive terms of the *Angular Momentum Equation*, which showed that the effect of compressibility is the dominant process of angular momentum transport inside the vortex. As a suggestion for further research, the generality of this result may be tested by repeating the experiments of this study under different flow conditions.

Vortex Energetics

The role of compressibility and viscosity on the structure and behavior of the vortex is still not fully understood. What is missing from this analysis, is a full description of the energetics inside the vortex. As an extension of this study,

an analysis of the terms of the *Energy Equation* may be performed, which
would require information about the time-dependence of v_ϕ. This information
can be gained by repeating the pressure experiments; using multiple pressure
transducers at different locations along the vortex path.

Empirical Density Law of Compressible Vortices

The method of representation of data by equations used in this study was
primarily motivated by the convenience of using empirical information in this
form in the governing equations for the calculation of other properties. An-
other benefit of finding a simple mathematical formula to accurately represent
data, is the possibility that an exceptionally good fit, such as that found in
these density experiments, may be an indication that the function itself has
some physical significance; in this case to compressible vortices in general.
The generality of this function may be investigated in an extension of this
study (using the same shock tube apparatus and diagnostics) by repeating
the density experiments under varied flow conditions.

Computer Simulations

As a final suggestion for further research; solutions of the governing equations
found by computational methods may also help provide more insight into
the questions discussed above.

Appendix A

The Shock Tube

Begining with a brief treatment of shock tube theory (see Thompson [6] for a complete description of the theory), the actual experimental flow conditions both in the shock tube and in the test section are described including a boundary layer calculation.

A.1 Shock Tube Theory

A shock wave is a thin region of rapid state variation across which there is a flow of matter. Physically, shocks have a measurable thickness of the order of 10^{-6}m. Where a characteristic length becomes comparable to intermolecular dimensions, the continuum fluid models break down. This allows the treatment of a shock wave as an idealized *surface of discontinuity* in space. In general all fluid properties – pressure, velocity, density, etc. – are considered discontinuous across the shock surface. The flow of matter across the shock front must satisfy the inviscid gasdynamic conditions of balance for mass, momentum, and energy in the form of *jump conditions* (Thompson [6]) which

can be written in the following form:

$$\rho_1 u_1 = \rho_2 u_2$$

$$\rho_1 u_1^2 + P_1 = \rho_2 u_2^2 + P_2$$

$$c_p T_1 + \frac{u_1^2}{2} = c_p T_2 + \frac{u_2^2}{2} \, ,$$

where the subscripts 1 and 2 denote the properties of the fluid on opposite sides of the shock and the velocities u are relative to the shock.

In a shock tube, a traveling shock is generated at one end by a ruptured diaphram which initially separates the ambient gas in the tube from a higher pressure driver gas. The initial state of the gas in the test section and the tube is measured before the diaphram ruptures. The parameters P_1 and T_1 are most easily measured and completely define the initial state, which in this case corresponds to atmospheric conditions in the lab. After the shock is generated, its laboratory frame velocity u_{1l} or Mach number M_{1l} through the gas is measured by a time-of-flight method using two laser beams and detectors (see Appendix D). In this particular application of the shock tube, it is the flow behind the shock that is of interest. It is then convenient to write *jump conditions* relating the properties of this flow to the initial experimentally measured quantities P_1 , T_1 and M_{1l}. The most useful relations are summarized below:

$$\rho_1 = \frac{P_1}{RT_1}$$

$$c_1 = (\gamma RT_1)$$

$$M_{1l} = \frac{u_{1l}}{c_1}$$

$$P_2 = P_1 \frac{2\gamma M_{1l}^2 - (\gamma - 1)}{\gamma + 1}$$

$$T_2 = T_1 \frac{[(\gamma - 1) M_{1l}^2 + 2][2\gamma M_{1l}^2 - (\gamma - 1)]}{(\gamma + 1)^2 M_{1l}^2}$$

$$\rho_2 = \rho_1 \frac{(\gamma + 1) M_{1l}^2}{(\gamma - 1)^2 M_{1l}^2 + 2}$$

$$u_{2l} = \frac{2c_1}{\gamma + 1}\left(M_{1l} - \frac{1}{M_{1l}}\right)$$

$$c_2 = \left(\frac{T_2}{T_1}\right)^{\frac{1}{2}}$$

$$M_{2l} = \frac{u_{2l}}{c_2} = \frac{2\left(M_{1l}^2 - 1\right)}{[2\gamma M_{1l}^2 - (\gamma - 1)]^{\frac{1}{2}}\,[(\gamma - 1)\,M_{1l}^2 + 2]^{\frac{1}{2}}}$$

$$Re_{2l} = \frac{\rho_2 u_{2l} L}{\mu} \approx \frac{\rho_1 L}{\mu_2}\frac{2c_1\left(M_{1l}^3 + M_{1l}\right)}{(\gamma - 1)\,M_{1l}^2 + 2}\ .$$

These relations illustrate the shock tube's capability for independent variation of the Mach number M_{2l} and the Reynolds number Re_{2l} of the flow behind the shock. This useful, uniform, well-characterized flow behind the shock is eventually interrupted by the contact surface which separates the fluid particles of the test gas and driver gas and which travels behind the shock at the flow velocity u_{2l}. The useful flow time Δt in a test section that is a distance d from the diaphram (the initial position of the contact surface) is given by

$$\Delta t = d\left(\frac{1}{u_{2l}} - \frac{1}{u_{1l}}\right)\ .$$

A calculation of Δt for the shock tube described in Section 2.1.1 where $d = 6$ m and $M_{1l} = 2$ gives a value of 5.25 milli-sec.

The Mach number of the shock M_{1l} is determined by the initial pressure ratio P_4/P_1 at the diaphram between the test gas and the higher pressure driver gas and is given implicitly by the relation [6]

$$\frac{P_4}{P_1} = \frac{2\gamma_1 M_{1l}^2 - (\gamma_1 - 1)}{\gamma_1 - 1}\left[1 - \frac{\gamma_4 - 1}{\gamma_1 + 1}\frac{c_1}{c_4}\left(M_{1l} - \frac{1}{M_{1l}}\right)\right]^{-\frac{2\gamma_4}{\gamma_4 - 1}}\ ,$$

where the parameters of the test gas and driver gas are denoted by the subscripts 1 and 4 respectively. The appropriate pressure ratio must be attained at the instant of diaphram rupture in order to generate the required shock for a particular application. This is done in practice by preparing a diaphram according to empirically determined prescriptions of material type, thickness, hardness and depth of scribed grooves for weakening. For these experiments,

a Mach 2 shock wave is produced at atmospheric conditions by using a .040 inch thick aluminium diaphram (type 6061-T6) with $\approx$ .010 inch deep grooves machined into the surface in an X pattern. The driver section is pressurized to $\approx$ 600 psi at which point the diaphram ruptures. The ratio P_4/P_1 in this case is $\approx$ 40 and a Mach 2 shock is produced. For comparison, the theory predicts the generation of a Mach 2 shock given an initial pressure ratio of $P_4/P_1 \approx 34$.

A.2   Experimental Conditions

A.2.1   Shock Tube Flow

The shock tube is run with the driven section open to the laboratory atmosphere which is maintained at an average temperature of 293 ± 2 ($\pm 0.7\%$) degrees Kelvin. The atmospheric pressure varies from day to day in the laboratory and has an average value given by $P_1 = 760 \pm 10$ ($\pm 1.3\%$)mm Hg (or equivalently $14.7 \pm .2$ psi). Further calculations reveal the average speed of sound given by $c_1 = 343.3 \pm 1$ m/sec and the density given by $\rho = 1.205 \pm .025$ kg/m^3. The shock is started when the diaphram is ruptured during pressurization of the driver section. The pressure P_4, at which the diaphram ruptures, can be controlled by the depth of the two crossed grooves which are machined into the surface of the diaphram. In these experiments, the value of P_4 ranged from $585 \rightarrow 615$ psi (see Table C.2 in Appendix C). This breaking pressure varied by ± 2.5 % from an average value of about 600 psi. The speed of the shock is measured at about 5 m downstream from the diaphram using the apparatus described in Section 2.1.3 (Chapter 2). The average value of the shock Mach number for Experiments #1 $\rightarrow$ #21, is $1.995 \pm .006$ (see Appendix C) and varies by $\pm 0.3\%$.

A.2.2 Test Section Flow

The Mach number of the shock decreases with distance from the end of the shock tube as the shock expands in a cyllindrical fashion inside the test section. The pressure signals (see Figures E.2 through E.5 in Appendix E) reveal a pressure gradient in the flow resulting from this expansion. A corresponding density gradient also exists in the flow as seen in the interferograms (Appendix C). Both the shock and vortex convection speeds are measured by a time-of-flight measurement (see Appendix D). The Mach number of the shock is plotted as a function of the distance x from the entrance of the test section in Figure D.6 (Appendix D) and ranges in value from 2 to 1.36 as the shock expands. The vortex convection velocity is found to range in value from 179 to 189 m/sec under a wide range of shock tube conditions (see Table D.3 in Appendix D).

A.2.3 Boundary Layer Calculation

The thickness δ of the boundary layer behind the shock can be estimated by the relation [6]

$$\delta \sim \sqrt{\nu t} \, ,$$

where ν is the kinematic viscosity (1.8×10^{-5} kg/m-sec) and t is the time after shock passage. From the pressure response of the flow shown in Figure E.2 (Appendix E), the vortex is seen to arrive at the pressure transducer about $t=300$ micro-sec behind the shock. From these considerations, an estimated value for δ at the vortex location is about 50 microns, which is small compared to the inside dimensions of the shock tube (5 cm). From these considerations, it is not expected that the boundary layer would have an appreciable effect on the optical or pressure measurements of the vortex.

Appendix B

The Ruby Laser

The method of Double Exposure Holographic Interferometry (as described in Appendix C) requires a coherent light source to provide suitable object and reference beams for the technique. In the present application, the flow is changing rapidly and so the exposures must be made on a time scale that is very short, compared to the time scales characteristic of the flow, to prevent a time-averaging effect. A ruby laser is chosen as the light source for the experiments, mainly because of its good coherence properties and because of the short time duration of the pulses. This type of laser has a fairly large output energy and its wavelength is fairly well matched to the photographic materials available for holography. A brief description of the design and operation of this device is presented. (See Hariharan [32] for a complete treatment on the design of the ruby laser for holographic applications.)

B.1   Laser Design and Operation

A laser, in general, consists of an active medium for amplification of a certain wavelength of light and an optical cavity to provide feedback of the amplified light back into the medium. When the optical gain of the medium given by

the gain coefficient A becomes larger than the optical losses of the mirrors, then laser oscillation occurs. The small-signal power gain of the ruby is given by

$$G = e^{A(\nu)L} ,$$

where L is the length of the ruby rod (10 cm) and where $A(\nu)$ is the gain per unit length of the ruby after a population inversion is created by means of optical pumping with a flashlamp. The condition for laser oscillation is given by the relation

$$R_1 R_2 e^{2A(\nu)L} \geq 1 ,$$

where R_1 and R_2 are the power reflection coefficients of the two mirrors which make up the optical cavity. In this particular design the first mirror is 99.7% reflective at $6943\AA$ and the second mirror is an Ekalon (commercial name) resonant reflector consisting of 2 flat sapphire plates which together are about 60% reflective in a very narrow optical bandwidth. The beam is provided by the coherent light that escapes the cavity through the partially transmissive Ekalon during the oscillation. The distance D between the mirrors is 1 m. The longitudinal modes of this cavity have a frequency spacing given by the Free Spectral Range (FSR) which is related to the distance D by the relation

$$FSR = \frac{c}{2D} = 150 \, MHZ .$$

The coherence length Δl of the laser was found to be about 10 cm by changing the optical path length of the reference beam and monitoring the quality of the resultant holograms. The combination of the spectral selectivity of the Ekalon along with the practice of operating the laser close to *oscillation threshold* insures that the laser oscillates in only one mode and thereby produces a beam with sufficient coherence for holography. The laser also has a Pockels cell type Q-switch in the cavity which is a fast-acting optical shutter. The Pockels cell consists of a polarizer and a field-induced Birefringent crystal which is placed so that its principle axis is 45 degrees with respect to the direction of polarization of the beam. When a voltage is applied to the crystal, a phase shift of $\pi/2$ is produced between the transmitted components, thereby

rotating the polarization of the beam 45 degrees. After reflection from the end mirror, the return pass through the crystal results in total rotation of polarization by 90 degrees to that of the polarizer thereby blocking the beam from passing. When the voltage is quickly removed the Pockels cell allows the beam to pass. The Q-switch is necessary for allowing the energy in the ruby to be stored during flashlamp pumping. After the flashlamp has been on for about 1000 micro-sec, then the optical gain of the ruby reaches a peak value. It is at this time when the Q-switch opens and laser oscillation occurs producing a 10 nano-sec pulse of coherent light. Figure B.1 shows the time plots of the flashlamp current I and the corresponding laser gain coefficient A. The dashed line shows the immediate drop in A when the Q-switch opens at t=1000 micro-sec.
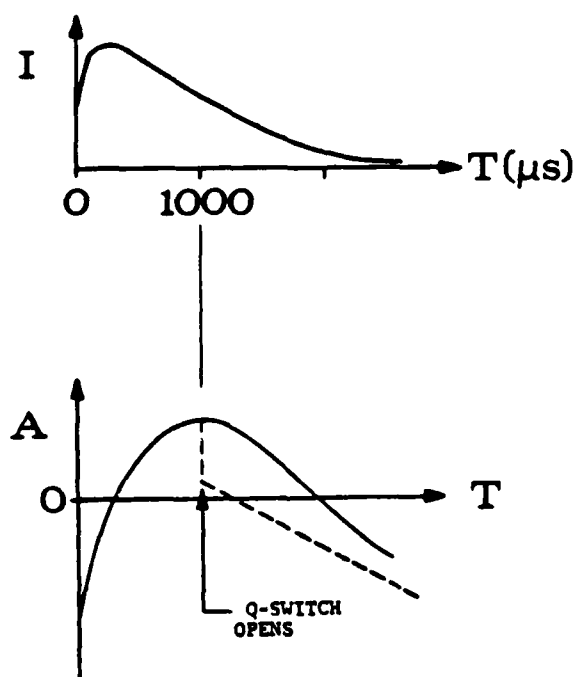
Figure B.1: Time Behavior of Flashlamp Current and Gain of Flashlamp Pumped Ruby.

Appendix C

Density Measurements
(Holography)

In standard Double Exposure Holographic Interferometry, interference between the wavefronts reconstructed by two holograms of the same fluid flow region takes place. The two holograms are recorded on the same photographic plate in two steps. Typically, the first exposure is made of the fluid at rest and the second is made during the flow conditions. The resultant interferogram allows the flow to be visualized and analyzed. Holographic interferometry is the primary diagnostic used in this study. A brief treatment of the theory is given, followed by a complete description of the experimental results and associated errors. (See references [30], [31] and [32] for complete treatments of this subject.)

C.1 Holography

C.1.1 Theory

The hologram is constructed by recording the interference pattern that occurs during the mixing of two beams of light. The time-varying electric field at any point of a linearly polarized light wave can be represented by

$$E(t) = \int_0^\infty a(\nu) e^{i(2\pi\nu t - \phi(\nu))} ,$$

where $a(\nu)$ is the amplitude and $a(\phi)$ is the phase of a component with frequency ν. If the light wave is of a single frequency then this becomes

$$E(t) = ae^{i(2\pi\nu t - \phi)} ,$$

which can be written as the product of a time varying factor and a factor which does not vary with time:

$$E(t) = ae^{-i\phi}e^{i2\pi\nu t} ,$$

where the factor

$$A = ae^{-i\phi}$$

is called the complex amplitude. The intensity I is given by

$$I = |A|^2 = AA^* ,$$

which represents the time average of energy per unit time per unit area at a point. Interference at a point of two waves is given by the superposition of electric fields

$$A_1 + A_2 = a_1 e^{-i\phi_1} + a_2 e^{-i\phi_2}$$

and the intensity of this interference is given by

$$I = |A_1 + A_2|^2$$

$$= |A_1|^2 + |A_2|^2 + A_1 A_2^* + A_1^* A_2$$

or equivalently

$$I = I_1 + I_2 + 2\left(I_1 I_2\right)^{\frac{1}{2}} \cos\left(\phi_1 - \phi_2\right)$$

$$= \langle I \rangle \left[1 + V \cos\left(\phi_1 - \phi_2\right)\right] ,$$

where $\langle I \rangle$ is the average intensity and V is the modulation of the intensity distribution, referred to as the *visibility* of the fringes and defined by

$$V = \frac{I_{max} - I_{min}}{I_{max} + I_{min}} = \frac{2\left(I_1 I_2\right)^{\frac{1}{2}}}{I_1 + I_2} \leq 1 .$$

If the polarization of the two light waves makes an angle θ, then

$$I = \langle I \rangle \left[1 + V \cos\left(\phi_1 - \phi_2\right) \cos\theta\right] .$$

All real wave-fields only have a finite degree of coherence. Both the spatial coherence and the temperal coherence of the light source must be considered. The actual bandwidth $\Delta\nu$ of the laser, with mean frequency ν_o, affects the coherence time $\Delta\tau$ of the radiation by the relation

$$\Delta\tau \approx \frac{1}{\Delta\nu} .$$

The coherence length Δl is defined by

$$\Delta l \approx c\Delta\tau \approx \frac{c}{\Delta\nu} = \frac{\lambda_o^2}{\Delta\lambda} ,$$

where c is the speed of light, $\Delta\lambda$ is the range of wavelengths and λ_o is the mean wavelength. It is necessary that the difference in path lengths from the light source to the point where interference occurs is less than the coherence length Δl.

C.1.2 Double Exposure Holographic Interferometry

In Figure 2.2 of Chapter 2, the optical arrangement for producing holographic interferograms is shown. The hologram is a photographic plate which records

the intensity distribution of light emerging on it. The object beam is collimated as it enters the test section and passes through the fluid-flow region. The reference beam does not pass through the test section. It is assumed that the changing conditions of the fluid-flow inside the test section are the only changing conditions of the optical system during both exposures of the hologram, so only the object beam is different in each case. During each of the two exposures, both the object and the reference beams simultaneously expose the holographic plate. This produces two different interference patterns and results in two holograms being recorded on the same plate. The intensity on the plate during the first exposure is given by

$$I_1(x, y) = |r(x, y) + o_1(x, y)|^2 \ ,$$

where

$$r(x, y) = r'(x, y) e^{-i\phi(x, y)}$$

represents the complex amplitude of the reference beam and where

$$o_1(x, y) = o'(x, y) e^{-i\phi_1(x, y)}$$

represents the complex amplitude of the object beam with no flow in the test section. After the plate is developed, the recorded image of fringes can be described by a transmittance function defined as the ratio of the light amplitude transmitted to that which is incident on the plate given by

$$T = T_o + T_1 I_1 + T_2 I_1^2 + \dots \ ,$$

where T_o is a background transmittance of the unexposed plate and T_1, T_2, etc. are properties of the photographic plate. Assuming the photographic process is linear, and neglecting T_o, then the transmittance can be written as

$$T \propto I_1 \ .$$

The intensity on the plate during the second exposure is given by

$$I_2(x, y) = |r(x, y) + o_2(x, y)|^2$$

where the reference beam has the same complex amplitude r(x,y) as that during the first exposure and the object beam's complex amplitude

$$o_2(x,y) = o'(x,y) e^{-i\phi_2(x,y)}$$

includes the new phase distribution $o_2(x,y)$ due to the presence of the flow. The resulting amplitude transmittance of the two superimposed holograms is given by

$$T(x,y) \propto I_1(x,y) + I_2(x,y) \ .$$

The hologram is reconstructed by illuminating it with the reference beam and results in a complex amplitude F given by

$$F(x,y) = r(x,y) T(x,y) \ .$$

In these experiments the region of the optical system containing the flow is imaged directly onto the plate during exposure resulting in an image-plane hologram and so

$$F(x,y) = T(x,y) \ ;$$

and the reconstructed intensity distribution is given by

$$I = |F(x,y)|^2 \ ,$$

which when expanded, contains a term that corresponds to the interference between the two object beams:

$$I \propto |o'(x,y)|^2 \left\{ 1 + V' \cos \left[\phi_1(x,y) - \phi_2(x,y) \right] \right\} \ ,$$

where V' is the actual modulation of the intensity distribution (or visibility) recorded on the plate and describes the distribution of fringes on the interferogram.

C.1.3 The Holographic Plate

The complex amplitude transmittance of the holographic plate can be represented as a polynomial and can be written as

$$T = T_o + \beta_1 E + \beta_2 E^2 + \cdots ,$$

where T_o is the transmittance of the unexposed plate, and β_1 and β_2 are the coefficients of the polynomial. The *exposure* E is defined by

$$E = \tau I \ ,$$

where τ is the exposure time and I is the intensity. When assuming linear response of the photographic process then the relation

$$T = \beta_1 E = \beta_1 \tau I$$

can be used where β_1 is the slope of the T-E curve that characterizes the photographic emulsion on the plate. Another parameter that characterizes the emulsion is the Modulation Transfer Function (MTF) which is defined as the ratio of the actual modulation of the plate to input modulation and is a function of the spatial frequency S. This can be written as

$$M(S) = \frac{V'(S)}{V(S)} \ .$$

C.2   Interferometry of Plane Flow Fields

The interpretation of interferogram fringes is greatly simplified in plane flows such as that in the test section. The fringe distribution is given by

$$1 + V \cos\left[\phi_1\left(x,y\right) - \phi_2\left(x,y\right)\right] \ ,$$

which at any point, the fringe shift S(x,y) can be found from the relation

$$S\left(x,y\right) = \frac{1}{2\pi}\left[\phi_1\left(x,y\right) - \phi_2\left(x,y\right)\right] \ .$$

This fringe shift is related to the change in optical path length by the relation

$$\lambda S\left(x,y\right) = \int_{S_1}^{S_2}\left[n_1\left(x,y,z\right) - n_2\left(x,y,z\right)\right]\,ds \ ,$$

where n_1 and n_2 are the initial and final distributions of index of refraction of the medium. In general, the integral cannot be inverted in the three dimensional case. Assuming the path $S_1 S_2$ is along the z axis and that the properties of the planer flow are independent of z, then the fringe shift is given by

$$\lambda S(x,y) = L[n_1(x,y) - n_2(x,y)] \ ,$$

where L denotes the distance spanned by the light beam in the direction of the ignorable coordinate z. Using the relation

$$n(x,y) - 1 = k\rho(x,y) \ ,$$

where k is the specific refractivity relating density ρ and refractive index n, the expression

$$\rho_1(x,y) - \rho_2(x,y) = \frac{\lambda}{kL} S(x,y)$$

directly relates the fringe shift distribution to the changes in the density distribution of the flow.

C.3 Refraction Error

In the previous analysis of interferometry of plane flow fields, the optical path length integral was simplified by the condition that the path $S_1 S_2$ of a light ray is along the ignorable z axis of the flow. When large density gradients in the x or y direction exist, then the light ray will be refracted from its original z direction and an error will occur in the location of the fringes. This refraction error can be analyzed by calculating the actual path of the ray. This can be done by making use of Fermat's principle which states that of the many possible paths for a light ray moving from one point to another, the path actually chosen is the one for which the transit time is stationary. The time (taken) t can be defined by

$$t = \int_{S_1}^{S_2} \frac{1}{V(S)} \, ds = \frac{1}{c} \int_{S_1}^{S_2} n(S) \, ds \ .$$

The ray will be allowed to refract in the y-z plane so that

$$ds = \sqrt{dy^2 + dz^2} = dz\sqrt{1 + \left(\frac{dy}{dz}\right)^2} \, .$$

The expression for t can be written as

$$t = \frac{1}{c}\int_{S_1}^{S_2} n\left(y\right)\sqrt{1 + \left(\frac{dy}{dz}\right)^2}\, dz \, .$$

The condition that this integral be stationary is satisfied by the ray equation [34] given by

$$\frac{d^2y}{dz^2} = \frac{1}{n\left(y\right)}\frac{dn\left(y\right)}{dy} \, .$$

In a gas medium, in non-resonant regions of the spectrum, the relation

$$n - 1 = k\rho \;\;, (n \approx 1)$$

can be used to give the result

$$\frac{d^2y}{dz^2} = k\frac{d\rho}{dy} \, ,$$

where $\frac{d^2y}{dz^2}$ is the local curvature of the ray path and where k is the specific refractivity defined by

$$k \equiv \frac{dn}{d\rho} \, .$$

If the density gradient is a constant, then

$$\frac{d\rho}{dy} = \frac{\Delta\rho}{\Delta y}$$

and the final deflection angle ε of a ray which spans the z distance L is given by

$$\varepsilon = \int_0^L \frac{d^2y}{dz^2}dz = k\frac{\Delta\rho}{\Delta y}\int_0^L dz = kL\frac{\Delta\rho}{\Delta y} \, .$$

The total displacement δ of the ray in the y direction can be approximated by the product of average deflection angle $\varepsilon/2$ and the distance L so that

$$\delta \approx \frac{1}{2}kL^2\frac{\Delta\rho}{\Delta y}$$

Experiment #	ε (miliradians)	δ (mm)
8	5.14	.128
10	5.21	.130
16	2.63	.066
21	2.98	.075

Table C.1: Fringe Refraction Error.

describes the error in the location of the fringe in the y direction. This error can be approximated for the case of the vortex using the parameters $\Delta\rho$ and Δr of the fitted vortex density functions (see Appendix H). The well-depth parameter $\Delta\rho$ and the half-width parameter Δr can be used in the relations

$$\varepsilon \approx kL\frac{\Delta\rho}{2\Delta r}$$

and

$$\delta \approx \frac{1}{2}kL^2\frac{\Delta\rho}{2\Delta r}$$

to calculate the deflection angle ε and the radial displacement δ. The ratio of the radial displacement of the fringe location and the total density radius of the vortex is then given by

$$\frac{\delta}{2\Delta r} \approx \frac{1}{2}kL^2\frac{\Delta\rho}{(2\Delta r)^2} \ .$$

These errors are calculated for the four cases: Experiments #8, #10, #16 and #21, using the density parameters given in Appendix H. The results of these calculations are given in Table C.1.

C.4   Interferograms #1→#21

The interferograms described in Section 2.2.1 are shown in Figures C.1, C.2, C.3, C.4, C.5, C.6 and C.7. These interferograms are the results of Experiments #1 through #21.   Interferograms #1 through #6 record the shock wave flow before the vortex is generated. Interferograms #7 through #21 show the vortex at sequential stages of development in approximately 50 micro-sec intervals. For each interferogram a close-up of the vortex is shown in the figures. The results of the evaluation of Interferograms #8 through #21 are given in Appendix I, Tables I.1→I.14. The plots of these data and the corresponding fitted curves are given in Appendix H, Figures H.1→H.14.
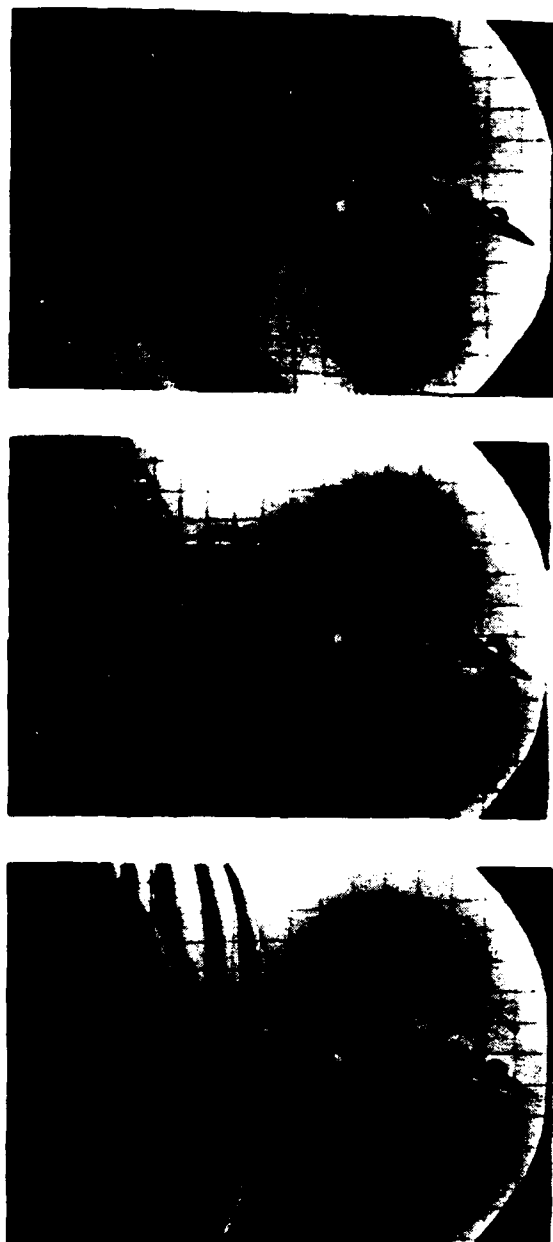
Figure C.1: Interferograms #1, #2 and #3.

Figure C.2: Interferograms #4, #5 and #6.
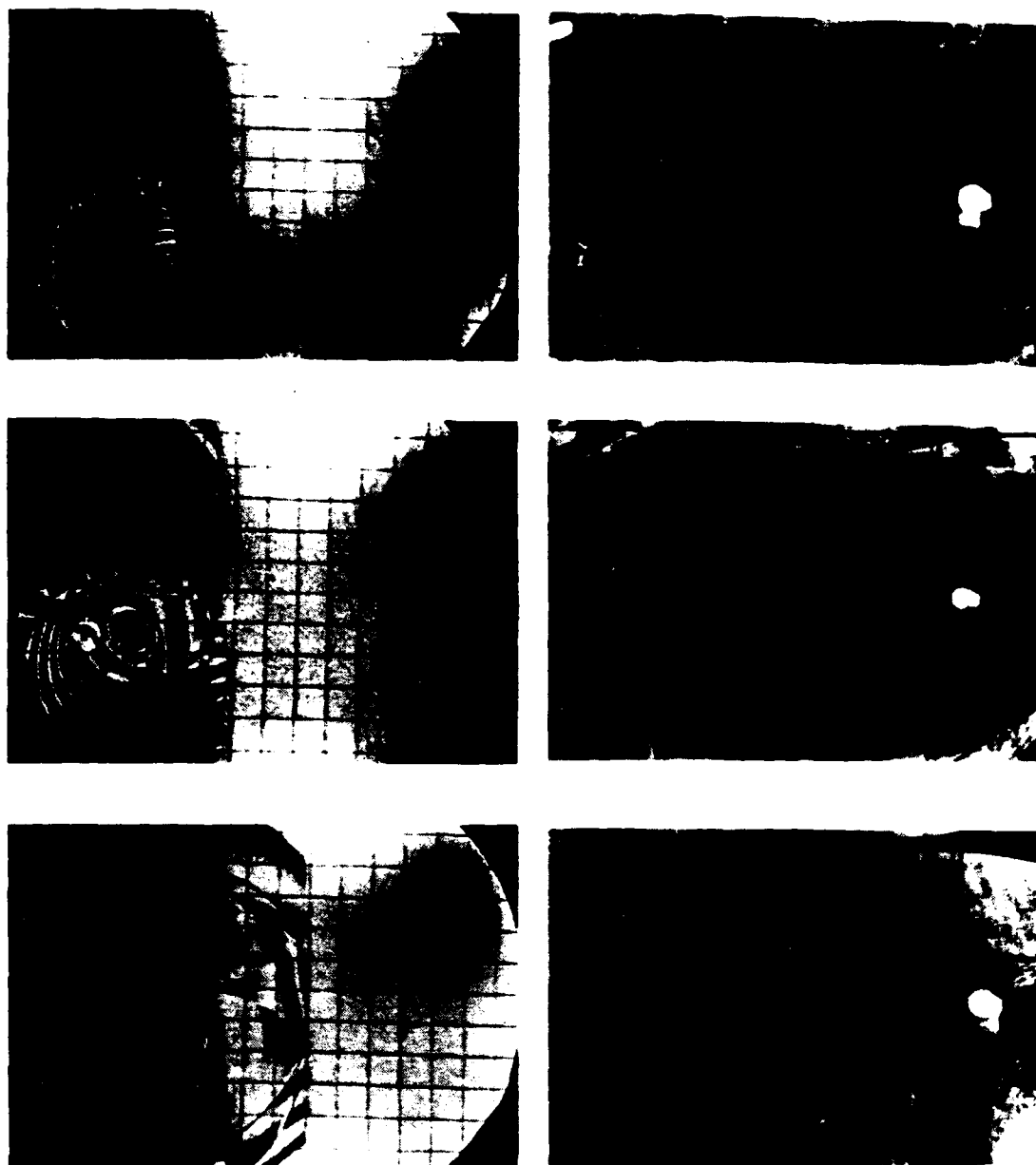
Figure C.3: Interferograms #7, #8 and #9 ; and Close-up of Vortex in Each Case.

Figure C.4: Interferograms #10, #11 and #12 ; and Close-up of Vortex in Each Case.
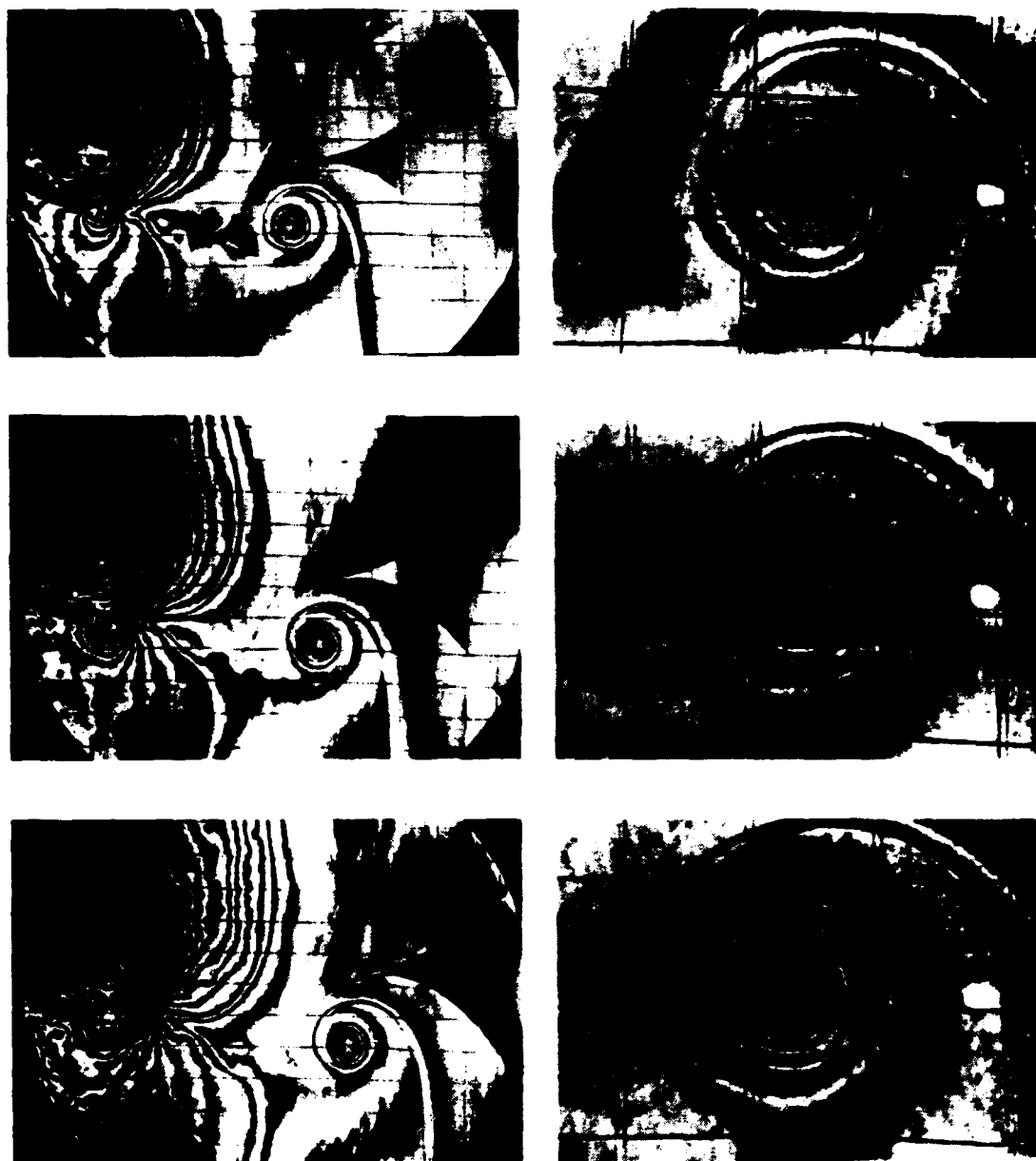
Figure C.5: Interferograms #13, #14 and #15 ; and Close-up of Vortex in Each Case.
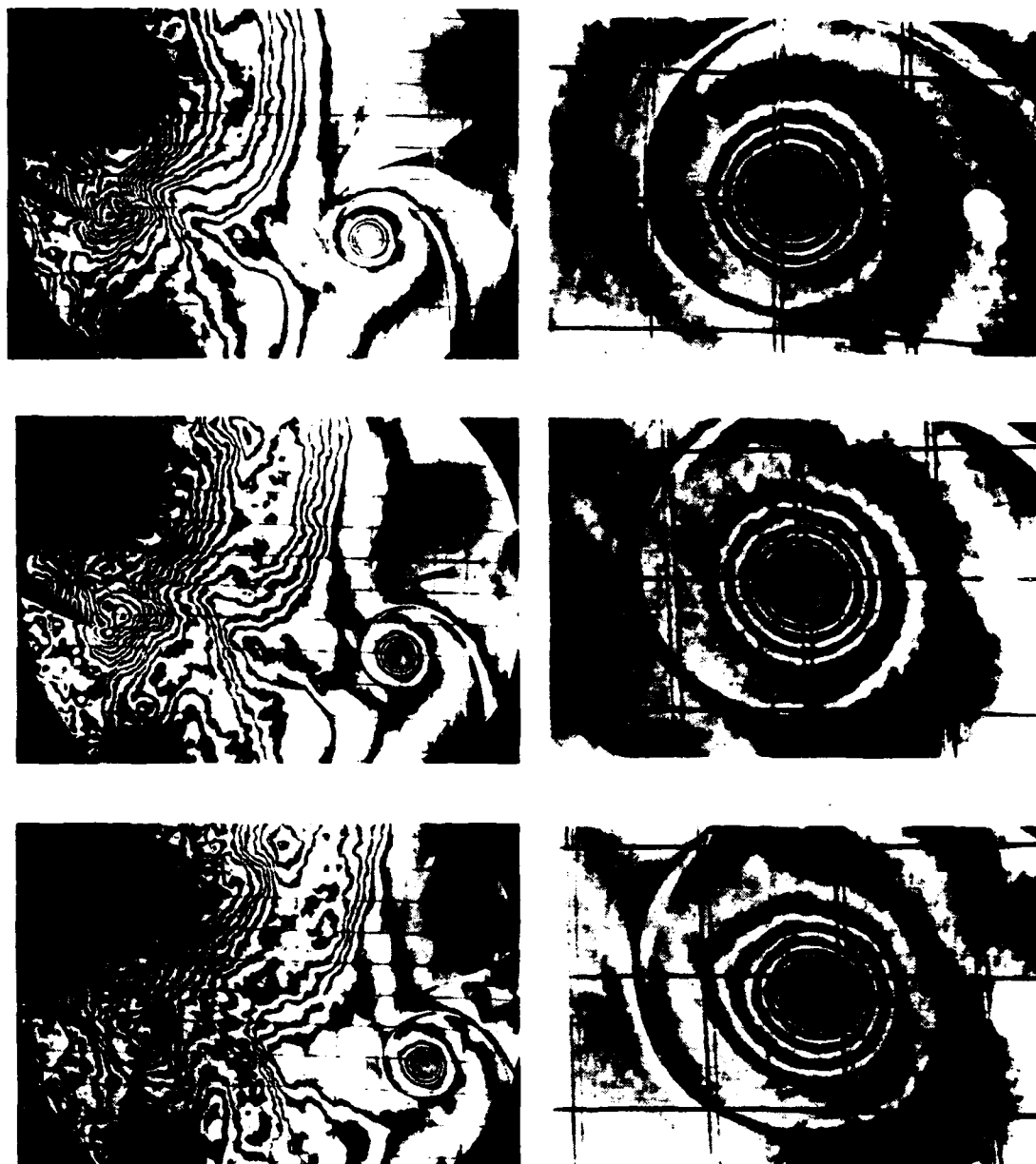
Figure C.6: Interferograms #16, #17 and #18 ; and Close-up of Vortex in Each Case.
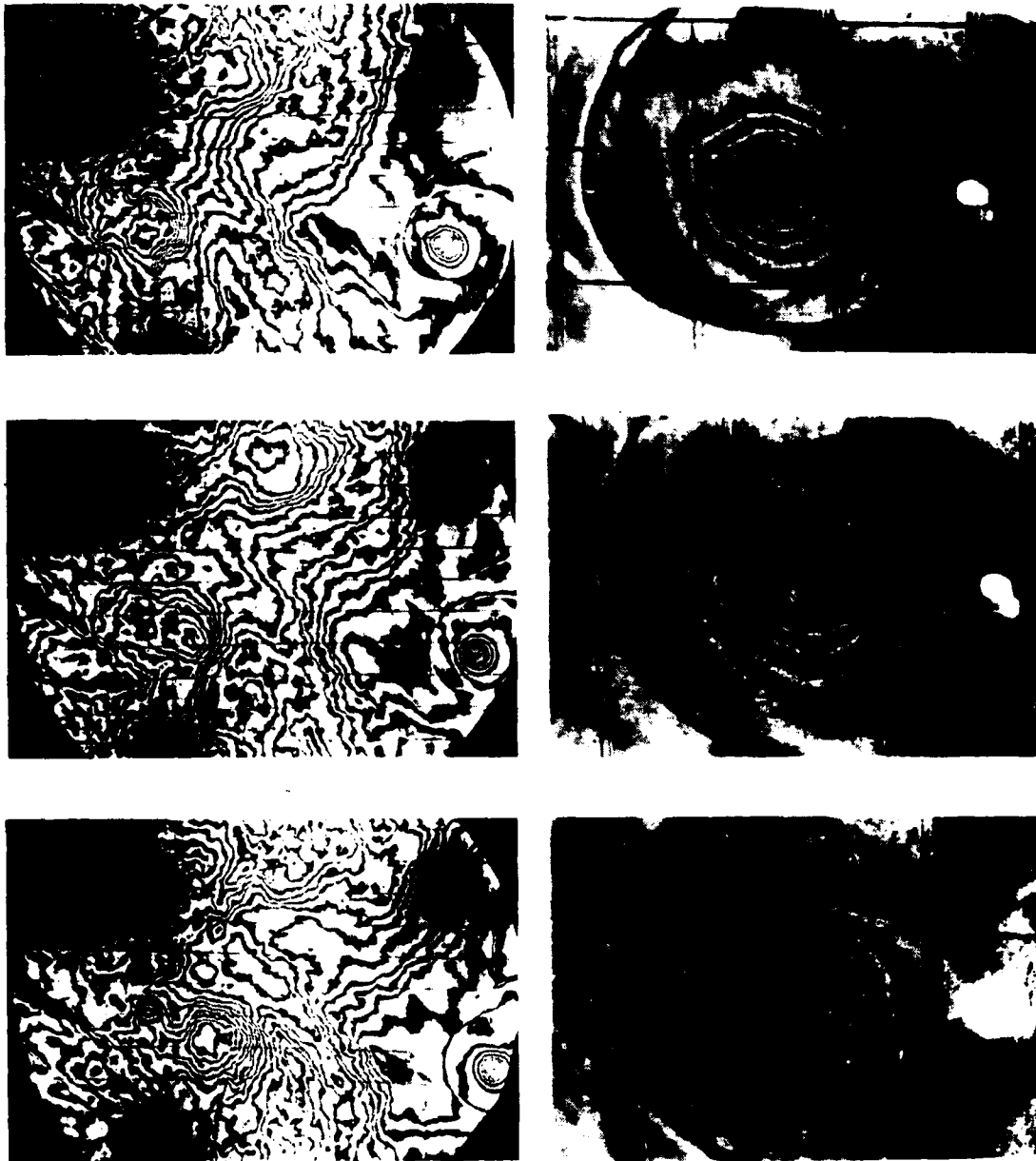
Figure C.7: Interferograms #19, #20 and #21 ; and Close-up of Vortex in Each Case.

C.5   2-D Flow Check

In order to check the two-dimensionality of the flow, an interferogram of the flow is made perpendicular to the vortex axis by rotating the test section about the axis of the shock tube by 90 degrees. Figure C.8 shows two interferograms made at the same DDG setting, and flow conditions, but with the collimated object beam parallel to the vortex axis in one case and perpendicular to the vortex axis in the second case. The straightness of the fringes in the second case represents the degree of two-dimensionality of the flow. The DDG setting for the laser pulse was 625 micro-sec and these conditions correspond closely to that of Interferogram #14. Since in the second case the flow expands in a cyllindrical fashion, the object beam spans different lengths of flow at different distances from the end of the shock tube up to a maximum of 65 cm, which is the distance between the windows containing the flow in this direction. The sensitivity of the interferogram in the second case is about 13 times that of the first case; and thus, a single fringe shift corresponds approximately to a change of only 1/260th of atmospheric density.

$$P_4 = 600 \; psi, \quad clock = 143.6 \; \mu s, \quad DDG = 625 \; \mu s$$
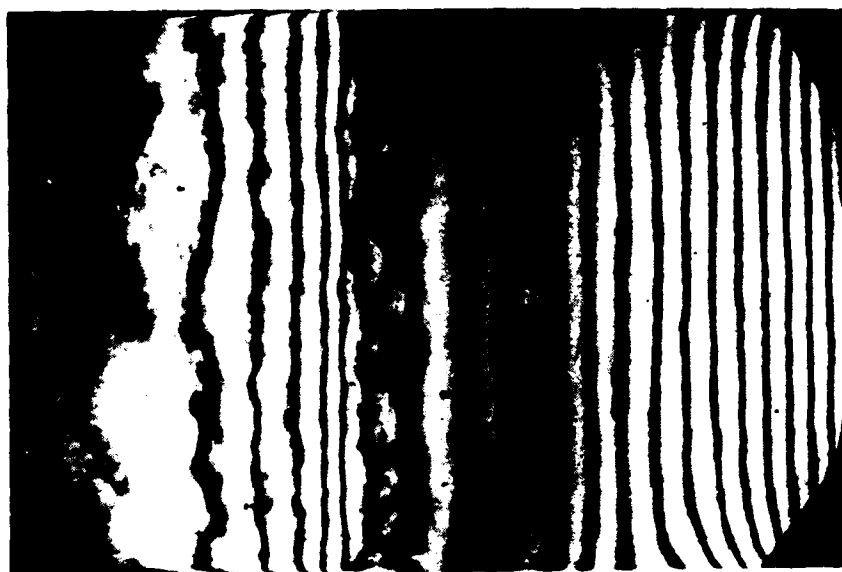
$$P_4 = 585 \; psi, \quad clock = 143.7 \; \mu s, \quad DDG = 625 \; \mu s$$

Figure C.8: Interferograms #22 and #23: 2-D Test of Flow.

C.6   Flow Repeatability Check

To check the repeatability of the flow conditions and the reliability of the
timing system, the two interferograms in Figure C.9 may be compared. The
shock tube conditions are given in each case. The DDG setting was determined
by several trials so that the center of the vortex can be seen in the location
of the crossed lines on the grid (which are scribed into the window). The
location of these crossed lines is described further in Appendix E. (These lines
mark the position of the hole which is later drilled into the window for the
mounting of the pressure transducer.) Comparison shows that the vortex in
both experiments is in the same location; and thus, the degree of repeatability
of the experiments is established.
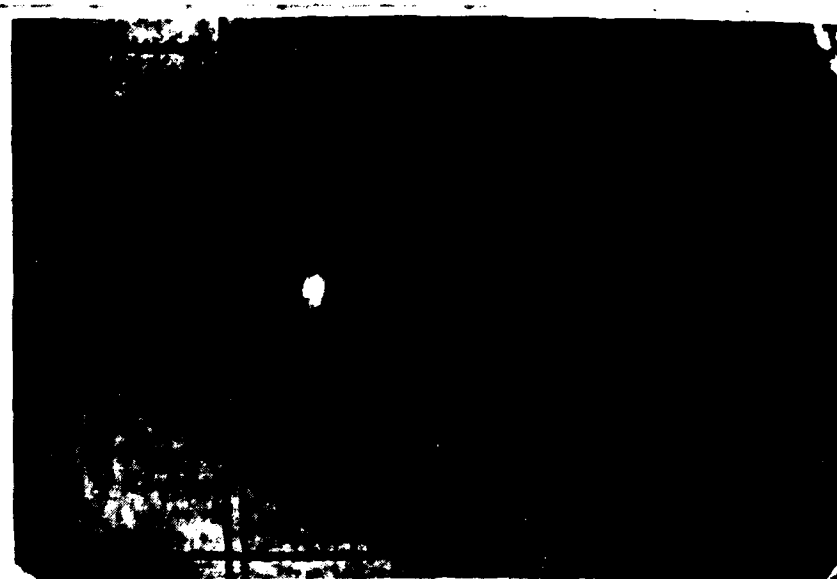
$$P_4 = 610 \ psi, \quad clock = 143.2 \ \mu s, \quad DDG = 770 \ \mu s$$
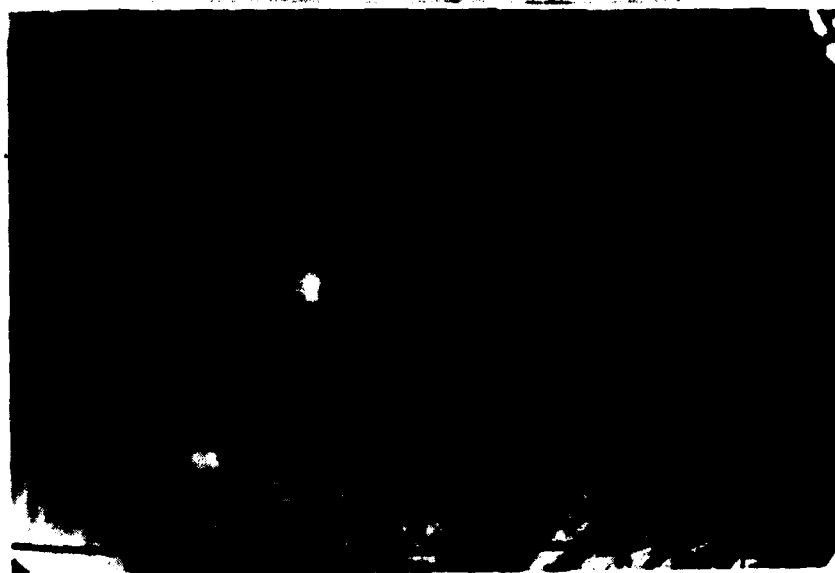
$$P_4 = 610 \ psi, \quad clock = 143.3 \ \mu s, \quad DDG = 770 \ \mu s$$

Figure C.9: Interferograms #24 and #25: Repeatability Test of Flow.

C.7 Determination of Vortex Age and Position

In order to determine the age of the vortex in each interferogram, a correction must be made to the preset delay time on the DDG to account for the slightly different speeds of the shocks in each case. The timing system is initiated by the shock and after a fixed time delay the laser is fired. The shock tube is fired once for each experiment and the shock tube flow conditions are recorded each time. These conditions are comprised of the diaphram breaking pressure P_4 and the shock speed V_s (as measured by the clock). The DDG setting for the timing of the delayed laser pulse (see Section 2.1.3, Chapter 2) is also recorded for each experiment. Table C.2 summarizes the essential information for each of Experiments #1 through #21. For each experiment, the first column indicates the experiment # and the second column identifies the holographic plate. The interferograms corresponding to these experiments are shown in Figures C.1 through C.7. The third and fourth columns in Table C.2 contain the values of the clock reading from the shock time-of-flight measurement system as described in Section 2.1.3 (Chapter 2) and the corresponding calculation of the shock velocity respectively. The average clock time recorded is 143.2 micro-sec and the average shock speed is 684.4 m/sec. The RMS deviation from the average value is .4 micro-sec and the corresponding shock speed deviation is 1.9 m/sec. The average shock Mach number is given by $1.995 \pm 0.3\%$. The total delay time of the laser pulse from the time of arrival of the shock at the shock sensing laser beam (see Section 2.1.3, Chapter 2) is the sum of the DDG setting and the Q-switch delay, both indicated in Table C.2. The Timing error Δt associated with the difference of the shock speed from the average value is given by

$$\Delta t = \left(clock - \overline{clock}\right) \left(\frac{total\ delay\ time}{clock}\right) ,$$

where the difference of the clock reading from the average value $\overline{clock} =$ 143.2 micro-sec is multiplied by the ratio of the total time delay and the clock reading. The values of Δt for the experiments are given in the last column of Table C.2. The RMS value of Δt for Experiments #1 through #21 is 4 micro-sec. For each experiment a corrected value of the total delay time is calculated by subtracting the timing error Δt. These corrected delay times are given in Table C.3 along with the x position of the shock and x-y coordinates at the vortex center as determined from Interferograms #1 through #21. Experiment #6 corresponds to the event of the vortex birth and for the analysis of the vortex, this is the zero reference time used for calculating the vortex age. The vortex age is then given by

$$t \, (vortex \, age) = (total \, corrected \, delay \, time) - 1460 \, microseconds \, .$$

The information in Table C.3 is used to plot the shock position and vortex trajectory in Figures C.10 and C.11. Figure C.10 shows the shock positions, the vortex trajectory relative to the shock tube test section and also a corresponding x-t plot of both the shock and vortex. Figure C.11 shows only the region of the test section where the vortex is convected and indicates the locations of the center of the vortex as determined from Experiments #6 through #21. From this detailed trajectory information, the position of the pressure transducer (also indicated in the figure) was determined. Also in Figure C.11 is an x-t plot of the shock and vortex in this region along with the straight-line best-fit to the points. The slopes of the best-fit lines give approximate velocities of both the shock and the vortex in this region of the test section. By this method the average vortex convection velocity is found to be 173 m/sec and the average shock velocity is found to be 498 m/sec. The speed of sound in air at room temperature (T=293 degrees K) is 343 m/sec; and thus, the calculated average Mach number of the shock is 1.43. (Other methods, described in Appendices D and E, are used to measure both the shock Mach number in the test section and the vortex convection velocity.)

Exp #	Plate #	Clock (μs)	Shock Speed (m/s) [+/- .5]	Clock-Clock (μs)	Speed-Speed (m/s)	DDG (μs) [+/- .01]	Q-Switch (μs) [+/- 1]	Total Time (μs) [+/- 1]	Total Time/Clock	Timing Error (μs)
1	493	142.8	686.3	-0.4	1.9	0.00	1065	1207.8	8.5	-3.4
2	499	143.9	681.0	0.7	-3.4	50.00	1065	1258.9	8.7	6.1
3	498	142.8	686.3	-0.4	1.9	100.00	1065	1307.8	9.2	-3.7
4	495	143.1	684.0	-0.1	0.4	150.00	1065	1358.1	9.5	-0.9
5	494	143.1	684.0	-0.1	0.4	200.00	1065	1408.1	9.8	-1.0
6	469	143.0	685.3	-0.2	0.9	250.00	1065	1458.0	10.2	-2.0
7	464	143.0	685.3	-0.2	0.9	300.00	1065	1508.0	10.5	-2.1
8	465	144.0	680.6	0.8	-3.8	350.00	1065	1559.0	10.8	8.7
9	463	143.9	681.0	0.7	-3.4	400.00	1065	1608.9	11.2	7.8
10	466	143.3	683.9	0.1	-0.5	450.00	1065	1658.3	11.6	1.2
11	462	142.9	685.8	-0.3	1.4	500.00	1065	1707.9	12.0	-3.6
12	467	143.1	684.0	-0.1	0.4	550.00	1065	1758.1	12.3	-1.2
13	459	142.8	686.3	-0.4	1.9	600.00	1065	1807.8	12.7	-5.1
14	470	143.0	685.3	-0.2	0.9	650.00	1065	1858.0	13.0	-2.6
15	460	143.1	684.0	-0.1	0.4	700.00	1065	1908.1	13.3	-1.3
16	472	143.4	683.4	0.2	-1.0	750.00	1065	1958.4	13.7	2.7
17	461	143.3	683.9	0.1	-0.5	800.00	1065	2008.3	14.0	1.4
18	473	143.2	684.4	0.0	0.0	850.00	1065	2058.2	14.4	0.0
19	474	143.2	684.4	0.0	0.0	900.00	1065	2108.2	14.7	0.0
20	475	142.8	686.3	-0.4	1.9	950.00	1065	2157.8	15.1	-6.0
21	476	143.1	684.0	-0.1	0.4	1000.00	1065	2208.1	15.4	-1.5
		*	**	***	****					*****

* $\overline{Clock}$: 143.2 μs

** $\overline{Speed}$: 684.4 m/s

*** rms (Clock-$\overline{Clock}$) : .4 μs

**** rms (Speed-$\overline{Speed}$) : 1.9 m/s

***** rms (Timing Error) : 4 μs

Table C.2: Experimental Conditions: Experiments #1→#21.

Exp #	Total Corrected Time (us) [+/- 1]	Shock Position X (cm) [+/- .02]	Center of Vortex	
			X (cm) [+/- .02]	Y (cm) [+/- .02]
1	1211.2	7.20		
2	1252.8	9.60		
3	1311.5	12.01		
4	1359.0	15.24		
5	1409.1	17.75		
6	1460.0	20.16	20.42	-1.39
7	1510.1	22.54	21.14	-1.21
8	1550.3	24.45	21.02	-1.29
9	1601.1	26.91	22.75	-1.34
10	1657.1	29.64	23.01	-1.36
11	1711.5	32.20	24.75	-1.47
12	1759.3	34.45	25.58	-1.56
13	1012.9		26.58	-1.71
14	1860.6		27.38	-1.01
15	1909.4		28.35	-1.90
16	1955.7		29.12	-1.97
17	2006.9		30.04	-2.05
18	2050.2		30.05	-2.12
19	2100.2		31.61	-2.24
20	2163.8		32.44	-2.39
21	2209.6		33.13	-2.43

Table C.3: Shock and Vortex Position; and Corrected Delay Time for Experiments #1→#21.
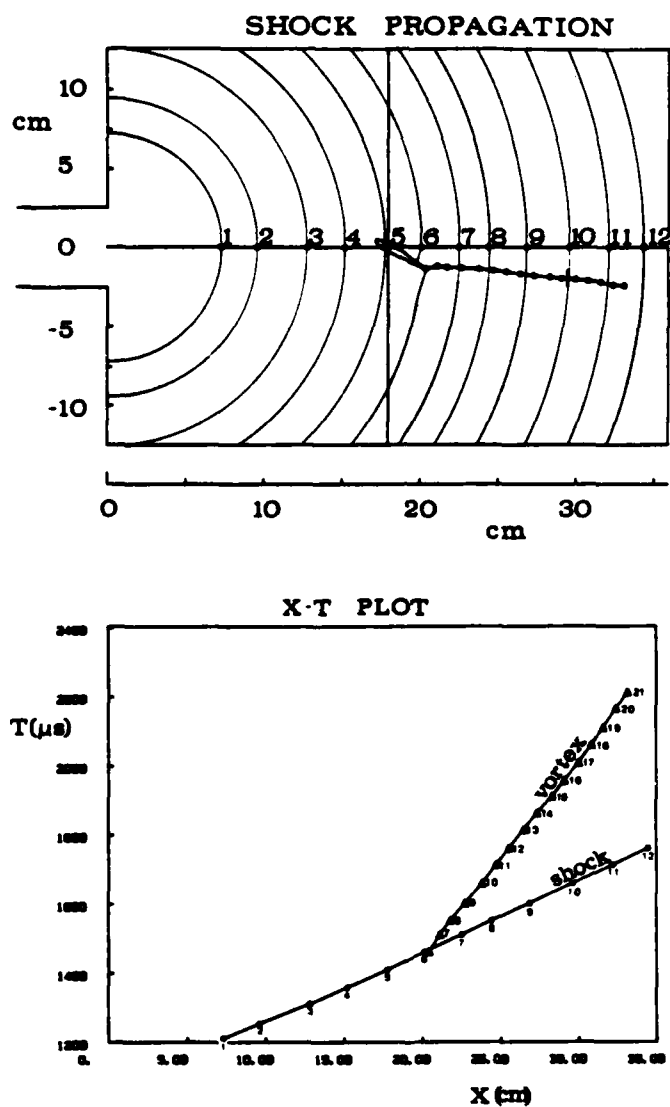
Figure C.10: Schematic Diagram Showing Position of Shock Along Centerline for Experiments #1→#12; and x-t Plot of Shock and Vortex Positions.
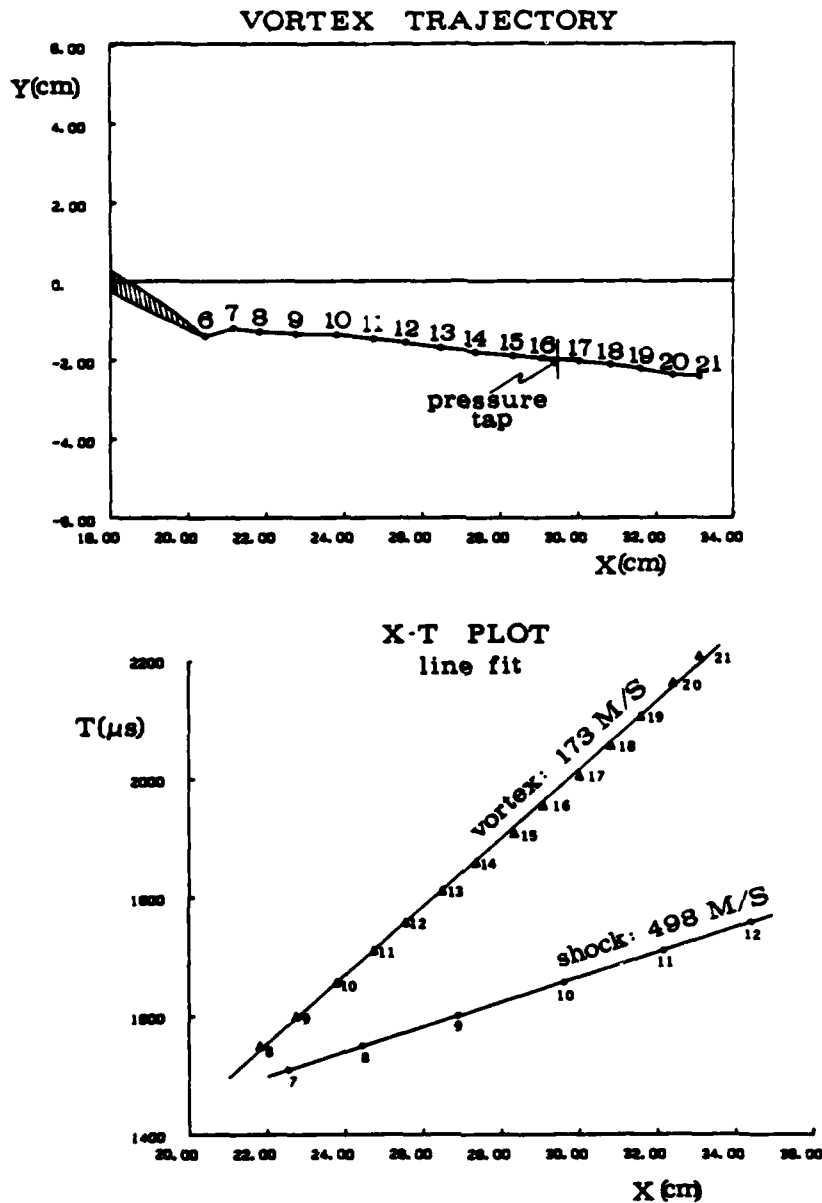
Figure C.11: Plot of Vortex Positions Along Trajectory for Experiments #6→#21; and Line-Fit to x-t data for Shock and Vortex.

Appendix D

Time-of-Flight Measurements

In Appendix C, values for the velocity of the expanding shock and the convection velocity of the vortex were calculated from information contained in the sequence of interferograms. These calculations are further supplemented by direct measurements of these velocities inside the test section using a time-of-flight method.

D.1 Apparatus and Method

The same type of apparatus used for shock speed measurements (in the shock tube) described in Section 2.1.3, is also used to measure the convection velocity of the vortex and the shock speed in the test section. This is a simple time-of-flight measurement using two parallel laser beams spaced a known distance apart which pass through the flow region. The actual positions of the laser beams relative to the vortex trajectory (Figure D.1) are 6.5 cm apart and pass through the flow where the vertical lines intersect the trajectory line in the figure. The beams are also perpendicular to the window. Each beam passes through the flow to a detector on the other side. As the shock or vortex arrives at each beam location in sequence, the density gradients of
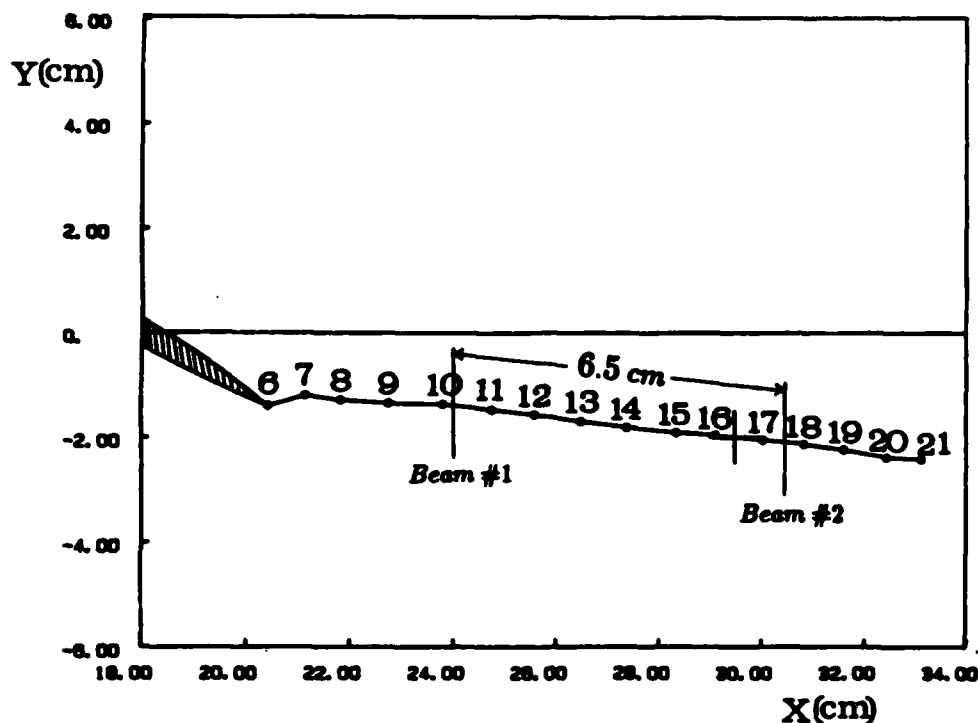
Figure D.1: Placement of Laser Beams Along Vortex Path for Shock and Vortex Time-of-Flight Measurements.

each deflect the beams and the light intensity level at the detectors decrease. The voltage output of the detectors is recorded on a dual trace oscilloscope and sample photographs of the traces are shown in Figure D.2, where the upper photograph is typical of those for measuring vortex speed and the lower one is typical of those for measuring shock speed. The upper photograph was taken at conditions very close to those which existed during the recording of Pressure Signal #3 shown in Figure E.4 (Appendix E). The measured vortex speed along the trajectory determined from this particular set of traces (upper photo Figure D.2) is found to be 180 m/sec ±2% . This speed was used to determine the transformation factor given by .018 cm/micro-sec, which is used in the transformation of the vortex time-response (Pressure Signal #3) into a spatial distribution (see Appendix E for further details).

D.2 Tabulation and Plots of Experimental Results

The results of several time-of-flight experiments at different running conditions are given in Tables D.2 and D.3. Table D.2 gives the measured velocity of the shock wave both before and after it enters the test section where the expansion causes it to slow down. (The Mach number of the shock in both cases is also given in this table.) Table D.3 gives the measured convection velocity of the vortex along with the initial speed of the shock that produced it. The information in these tables is summarized graphically in Figures D.3, D.4 and D.5. A graph of the expanded shock speed vs. initial shock speed is given in Figure D.3; a graph of the expanded shock Mach number vs. initial shock Mach number is given in Figure D.4; and a graph of the vortex convection velocity vs. the initial shock speed is given in Figure D.5.

These results are supplimented by additional information, in the form of x-t coordinates of the shock wave, gained by the following methods:

- Computer simulations of the test section flow yield x-t information about the shock, from which shock velocities and Mach numbers can be calculated.

- The interferograms (see Appendix C) also yield x-t information about the shock wave in this region of the test section.

Table D.1 gives the x-t coordinates of the shock along the x axis as obtained from Interferograms #1 through #12 (see Table C.3, Appendix C); the Mach number of the shock is calculated at each interval corresponding to a position x. Also in Table D.1, are supplimentary values of shock Mach number at different x positions which were obtained from computer simulations (see Moon [35]). Figure D.6 shows both an x-t plot of the shock and a plot of the shock Mach number vs. x position using the information in Table D.1. Also contained in Figure D.6, are the supplimentary results from the computer

Mach no. of expanding shock from experimental data:

Exp.#	x (cm)	t(mic-s)	MACH NO.
1	7.28	1211.2	1.624
2	9.60	1252.8	1.625
3	12.81	1311.5	1.533
4	15.24	1359.0	1.476
5	17.75	1409.1	1.418
6	20.16	1460.0	1.372
7	22.54	1510.1	1.385
8	24.45	1550.3	1.392
9	26.91	1601.1	1.426
10	29.64	1657.1	1.396
11	32.20	1711.5	1.364
12	34.45	1759.3	1.374

Mach no. of expanding shock from computer simulation:

x (cm)	MACH NO.
3.7	1.955
7.4	1.670
11.1	1.585
16.28	1.465
21.09	1.405

Table D.1: Expanding Shock x-t Coordinates and Mach Number From Interferograms and Computer Simulations.

simulations of the expanding shock; these points are indicated by the triangular symbols. The shock Mach number in the region of the pressure transducer is shown to be about 1.4 in Figure D.6. These results are further supported by pressure measurements across the shock, from which the shock Mach number can be calculated (see Section E.5, Appendix E). This information is used in determining a *density reference* for evaluation of the interferograms (see Section 2.3, Chapter 2).
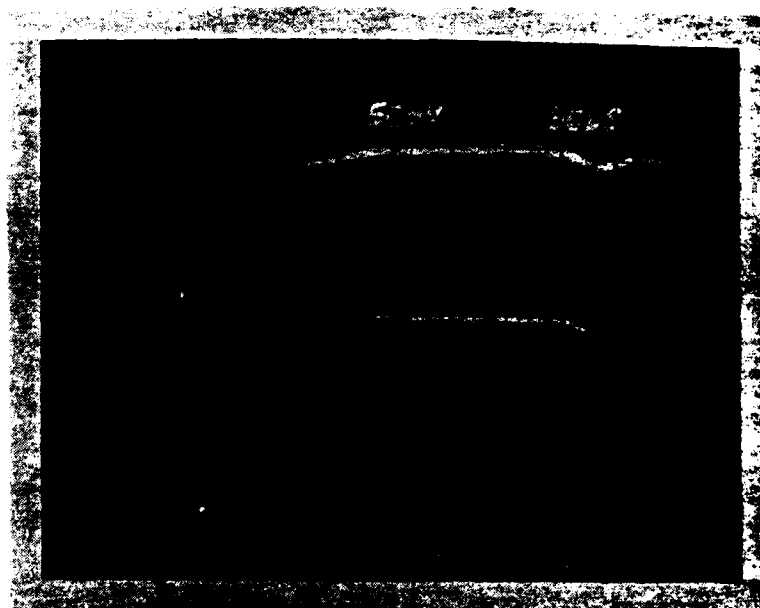
$$P_4 = 580 \ psi, \quad clock = 143.7 \ \mu s$$
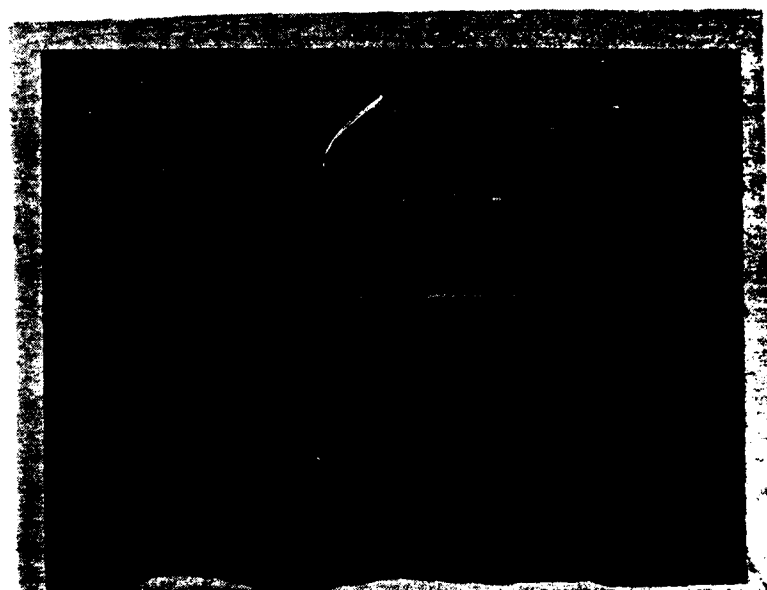
$$P_4 = 590 \ psi, \quad clock = 143.5 \ \mu s$$

Figure D.2: Time-of-Flight Signals Recorded on Oscilloscope Photos.

LASER MEASUREMENT OF SHOCK VELOCITY BEFORE AND AFTER EXPANSION

P4 (PSI)	clock (mic-s)	initial shock		expanded shock	
		v (M/S)	Mach no.	v (M/S)	Mach no.
---	-----	-----	-----	-----	-----
610	141.9	690.6	2.012	463.5	1.350
610	142.2	689.2	2.008	471.0	1.372
610	142.5	687.7	2.003	466.5	1.359
610	142.7	686.8	2.001	463.2	1.349
590	142.8	686.3	1.999	464.5	1.353
590	143.5	682.9	1.989	467.4	1.361
580	143.8	681.5	1.985	460.3	1.341
570	144.2	679.6	1.980	466.5	1.359
570	144.3	679.1	1.978	465.4	1.356

Table D.2: Expanding Shock Time-of-Flight Data Before and After Expansion.

VORTEX VELOCITY MEASUREMENT

initial shock speed (M/S)	resultant vortex speed (M/S)
------	------
672.15	180.39
673.54	179.39
674.00	181.56
675.86	182.67
677.26	183.62
679.14	183.01
680.56	185.70
681.03	184.40
685.79	183.18
686.76	189.14

Table D.3: Vortex Time-of-Flight Data.
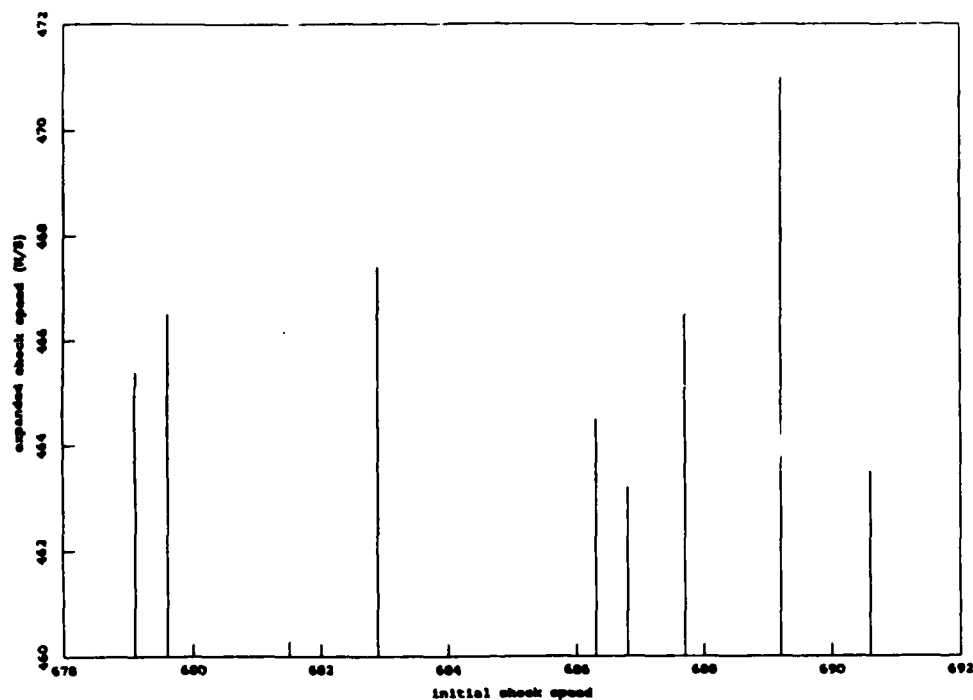
Figure D.3: Expanded Shock Speed Vs. Initial Shock Speed.
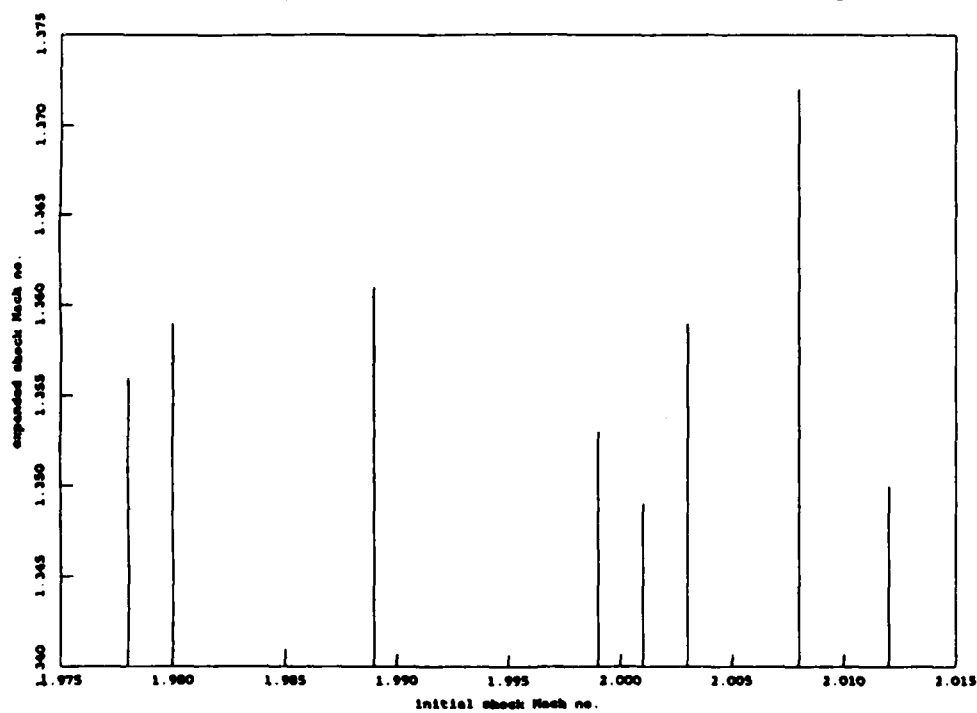
Figure D.4: Expanded Shock Mach Number Vs. Initial Shock Mach Number.
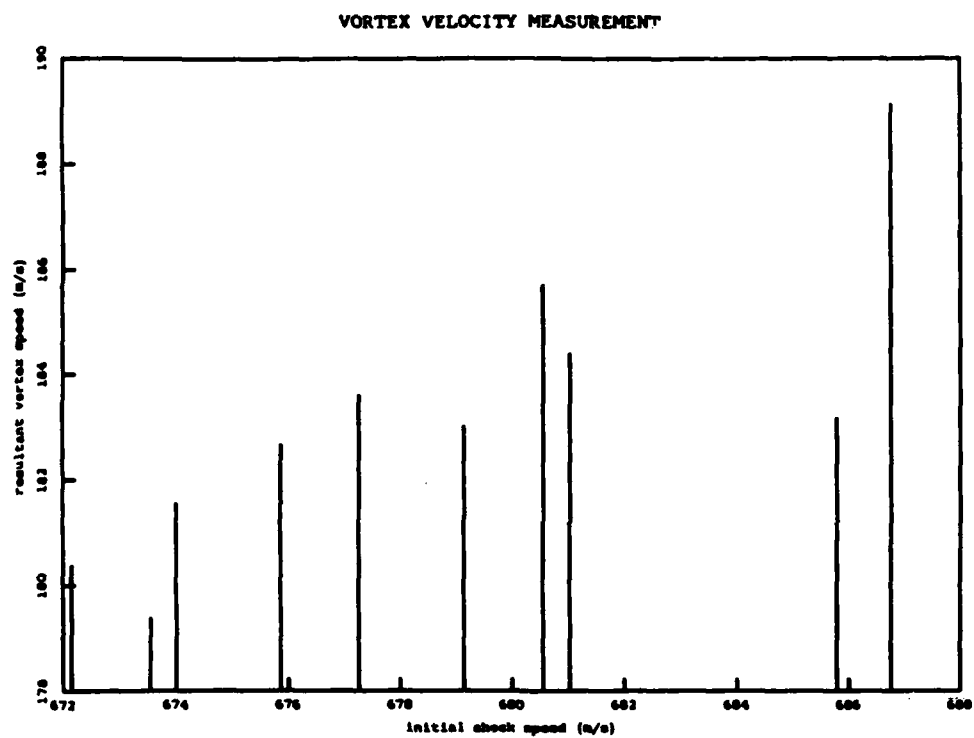
Figure D.5: Vortex Convection Velocity Vs. Initial Shock Speed.

x-t PLOT OF EXPANDING SHOCK

MACH NO. OF EXPANDING SHOCK VS. POSITION
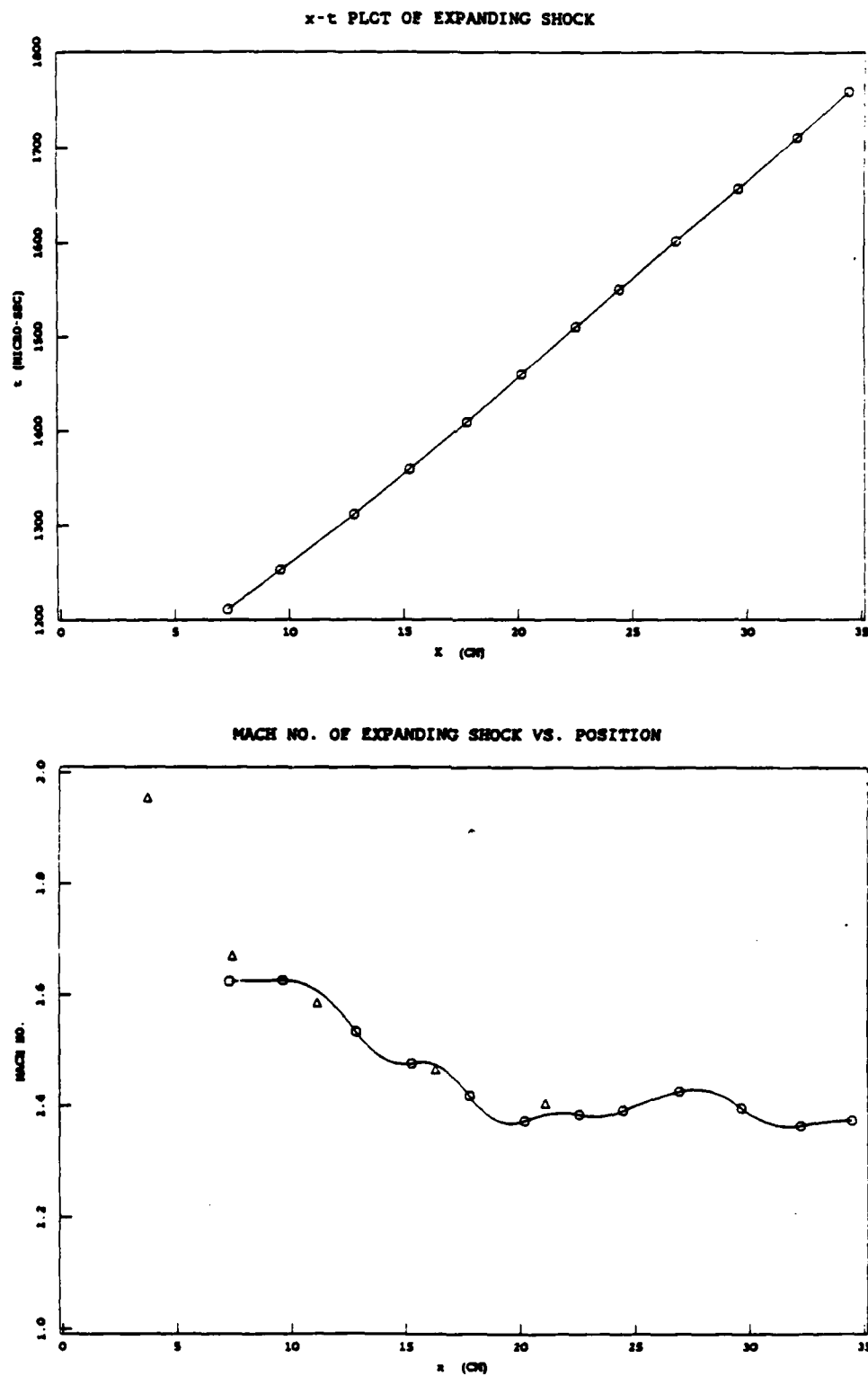
Figure D.6: x-t Plot of Expanded Shock and Plot of Mach Number of Expanded Shock Vs. x Position.

Appendix E

Pressure Measurements

E.1 The Pressure Transducer

The pressure transducer used in the experiments described in Section 2.1.4 is a solid state device which incorporates a diffused four-arm Wheatstone bridge on the surface of a silicon diaphram. These devices have a high natural frequency and low hysteresis which make them suitable for recording the unsteady pressure response of a traveling vortex. The transducer used is a type XCQ-080-50 made by Kulite Semiconductor Products, Inc. The rated pressure for this gauge is 50 psi; with a sensitivity of 1.89 mv/psi which was determined during calibration at the factory. The diameter of the cylindrical transducer package is .080 inches and the pressure sensitive area is .028 inches (.7 mm) across. The transducer was mounted such that the pressure sensitive diaphram was flush with the inside window surface.

143

E.2   Supporting Electronics

The supporting electronics for the pressure measurements consisted of a 5 volt DC power supply to provide the excitation voltage and an amplifier with a 50 khz bandwidth to amplify the signal from the transducer. The amplified signal is sent directly to an oscilloscope and the gain of the amplifier (approximately 100) is adjusted so that a one volt change on the scope trace represents a 5 psi change in pressure.

E.3   Transducer Positioning

The pressure transducer must be placed along the trajectory of the traveling vortex. The center of the vortex passes over the transducer and a pressure response in time is recorded on the oscilloscope. It is important to verify that the location of the transducer in the window coincides with the position of the center of the vortex at some delay time t. This was accomplished by first scratching a new vertical line which crosses a horizontal line of the grid, as shown in Figure E.1. As shown in the interferograms in Figure E.1 the intersection of these lines is observed to coincide with the center of the vortex at t=770 micro-sec. A hole is drilled into the window at this location for mounting the transducer. The experimental conditions corresponding to the interferogram in Figure E.1 are given in the figure caption.

E.4   Oscilloscope Photographs

Samples of the pressure response of the vortex are shown in the oscilloscope photographs in Figures E.2, E.3, and E.4. An additional oscilloscope photograph shown in Figure E.5 represents the pressure response of only the shock wave as it passes by the transducer. The three vortex pressure signals
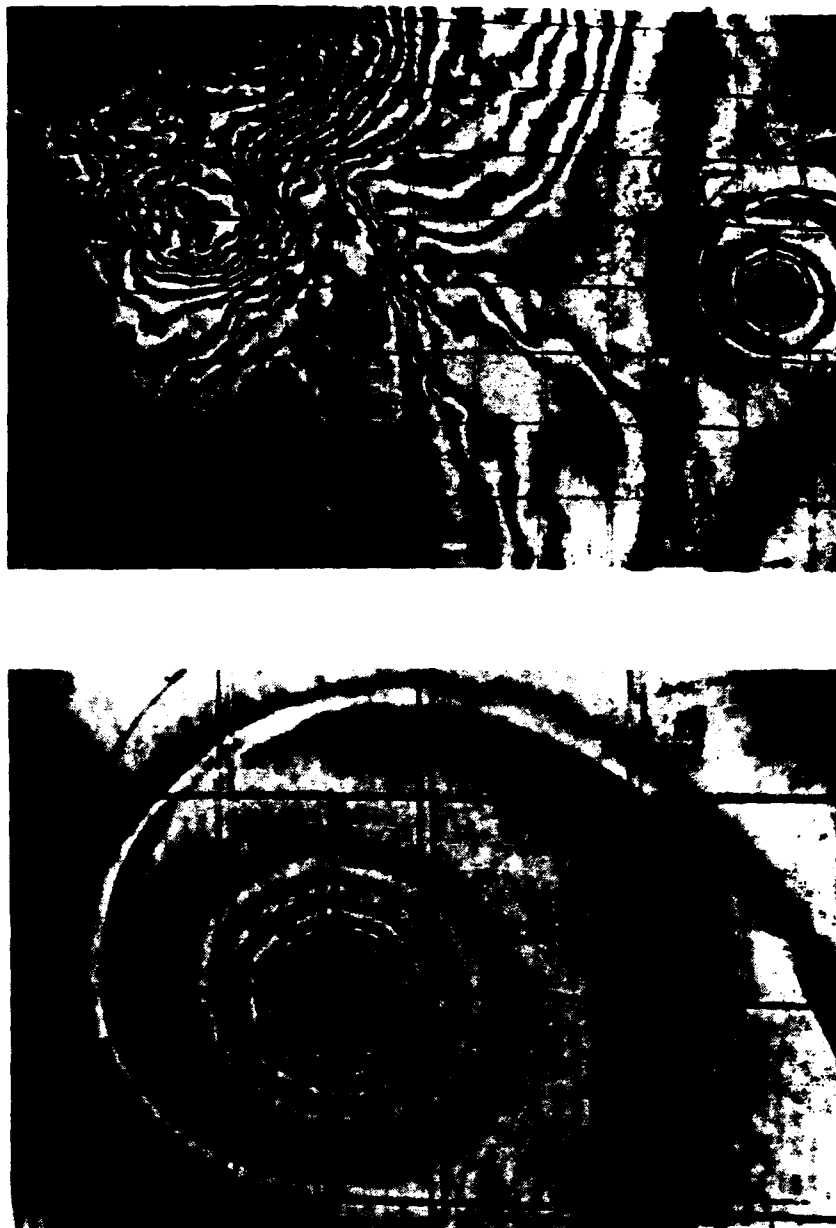
Figure E.1: Transducer Positioning Verification Photographs. Experimental Conditions: $P_4 = 610$ psi, clock=143.1 micro-sec, DDG=770 micro-sec. Upper interferogram shows vortex position relative to scribed crossed lines on window where the pressure transducer is later mounted. Lower interferogram shows close-up of vortex at same location.

(numbered 1 → 3 in the captions) are made under the following experimental conditions:

(a) Signal #1: $P_4 = 610$ psi, clock=143.3 micro-sec

(b) Signal #2: $P_4 = 585$ psi, clock=144.2 micro-sec

(c) Signal #3: $P_4 = 595$ psi, clock=143.7 micro-sec

In each case the upper photograph represents the pressure response of the whole shock generated flow including the convected vortex. The time scale is 100 micro-sec/division and the sensitivity is 5 psi/division. The initial sharp pressure rise is due to the passage of the shock. This is followed by a fairly constant rate of decreasing pressure and then the arrival of the vortex is observed about 300 micro-sec behind the shock. The lower photograph shows the same signal in an expanded time scale (10 micro-sec/division) and sensitivity (2.5 psi/division) in order to reveal the details of the vortex only.

Pressure Signal #4 shown in Figure E.5 was made under the following experimental conditions: $P_4 = 585$ *psi* and clock=144.2 micro-sec. The upper photograph represents the pressure response of the shock generated flow without the vortex generator (airfoil model) in place. The time scale is 100 micro-sec/division and the sensitivity is 5 psi/division. As in the other photos, an initial sharp pressure rise due to the passage of the shock is observed, followed by a fairly slow rate of decreasing pressure; but in this case, note the absence of the vortex. The lower photograph shows the same signal in an expanded time scale (2 micro-sec/division) and sensitivity (2.5 psi/division) in order to reveal the details of the shock wave only. The shock wave passing over the transducer very closely approximates a step-function pressure signal and is used to characterize the step-response of the pressure measurement system. This information is used in the deconvolution process of the vortex pressure signal (see Section E.6).
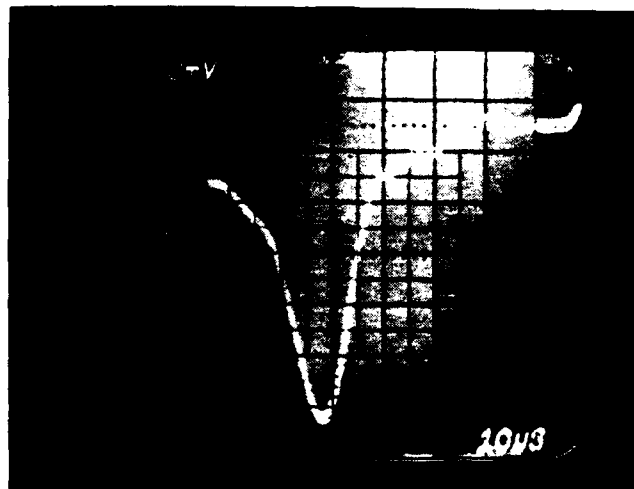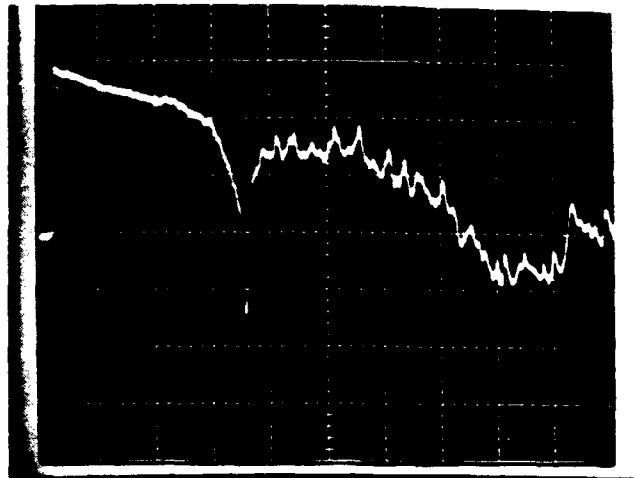
Figure E.2: Oscilloscope Photographs: Pressure Signal #1.
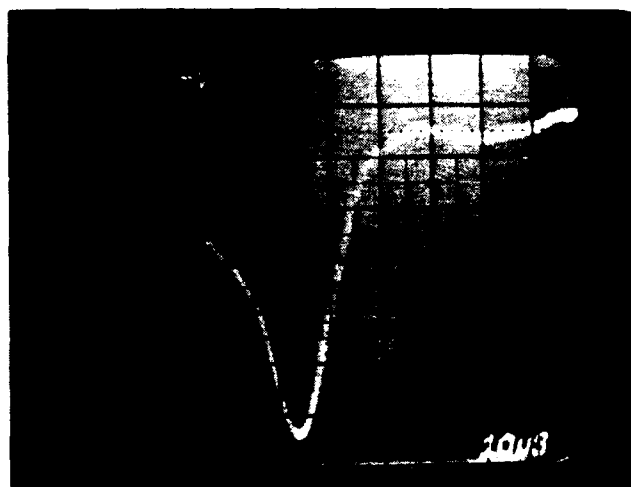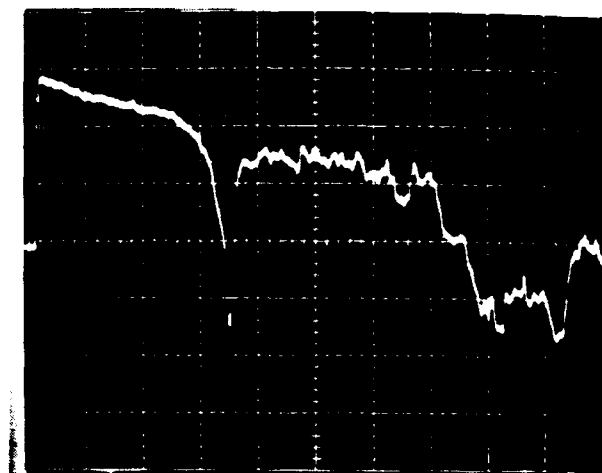
Figure E.3: Oscilloscope Photographs: Pressure Signal #2.
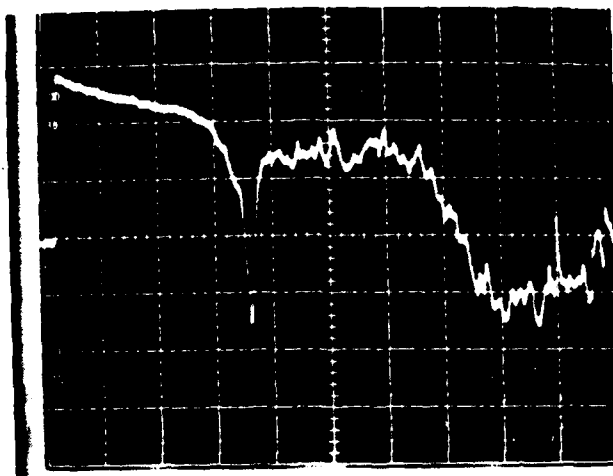
Figure E.4: Oscilloscope Photographs: Pressure Signal #3.
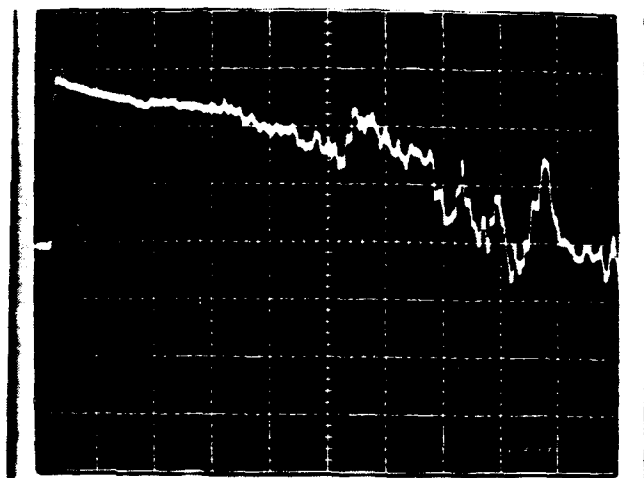
Figure E.5: Oscilloscope Photographs: Pressure Signal #4.
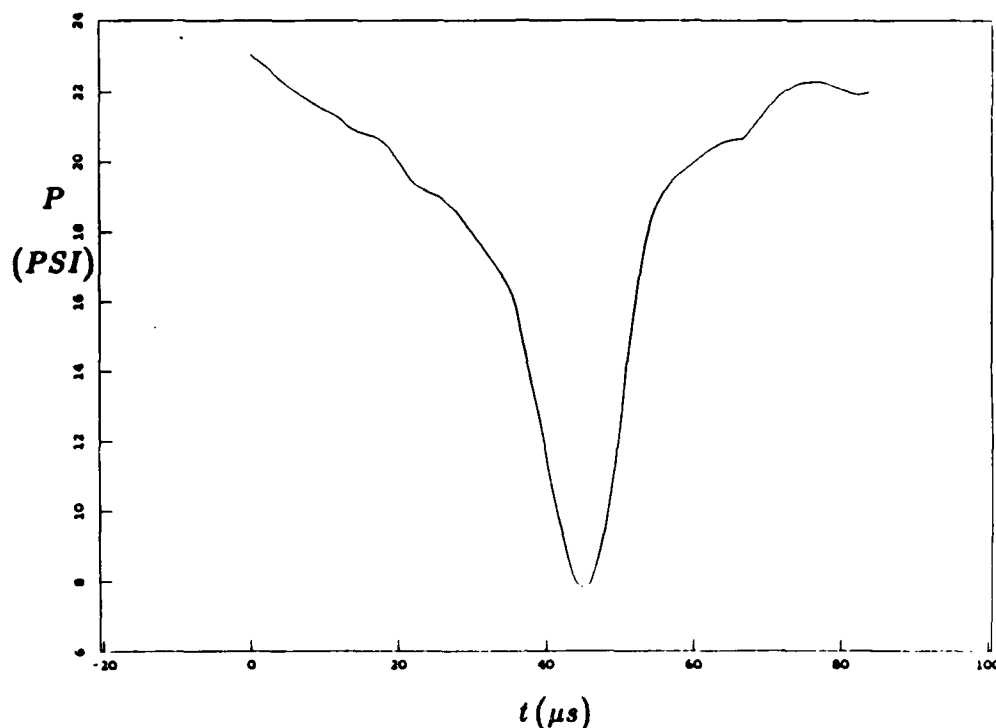
Figure E.6: Digitization of Vortex Pressure Signal #3.

E.5 Digitization of Pressure Signal

The pressure traces are digitized by hand using a digitizing tablet. The oscilloscope photograph is first enlarged so that the trace on the photograph is approximately the same size as the tablet. This insures that the trace is accurately resolved. The cursor guide is placed on the center of the trace as the trace is followed by hand. The initial set of coordinates are not equally spaced but are close enough so that a spline-fit to this data set yields an accurate set of equally spaced points representing the digitized pressure response of the vortex. The result of the spline-fit to the original coordinates entered into the computer from Pressure Signal #3 shown in Figure E.4 is plotted in Figure E.6. During this digitizing process the voltage and time scales are referenced to the divisions in the photographs and a conversion is made from voltage to pressure according to the calibration factor (5 psi/volt) given in Section E.2. The pressure is referenced from the part of the signal before the shock arrives,

which represents the ambient atmospheric conditions of the laboratory. The temperature of the air in the tube before arrival at the shock was $T_2 = 22$ degrees C and the pressure was 770 mm Hg or equivalently 14.7 psi. The signal in Figure E.5 resulting from the shock, shows a pressure increase of about 15 psi behind the shock. The shock strength is given by

$$\frac{P_2}{P_1} = 2.02 \ ,$$

which, according to the shock relations (see Appendix A) for a plane shock wave, corresponds to a shock Mach number of 1.37. This value of shock Mach number, calculated from the measured pressure ratio across the shock, is in close agreement with the results of the direct measurements of shock velocity described in Appendix D (see Figure D.6). This information is used in the evaluations of the interferograms (see Section 2.3, Chapter 2), in which the region of the flow behind the shock serves as a *density reference*. The density directly behind the shock can be calculated with the knowledge of the shock Mach number; using the shock relations given in Appendix A.

E.6   Deconvolution of Pressure Signal

As the traveling vortex passes over the pressure transducer, it induces a response in the form of a voltage which changes in proportion to the pressure. Since the pressure changes rapidly with time, the limited time-response of the system affects the accuracy of the oscilloscope trace to represent the actual pressure changes that have occurred. The measuring system can be characterized by its step-function response and this information can then be used to deconvolve the pressure signal.

E.6.1 Theory

The actual pressure changes associated with the traveling vortex over the transducer can be represented by a function of time $P_1(t)$. The signal or response of the system to these pressure changes can be represented as a Filtered function of time $P_2(t)$ which in Filter theory is given by:

$$P_2(t) = \int_{-\infty}^{\infty} I(t-\tau) P_1(\tau) \, d\tau = I(t) * P_1(t) \; ,$$

where I(t) is the impulse-response of the system defined by

$$I(t) = \frac{d}{dt} A(t) = A'(t) \; ,$$

where A(t) is the step-response of the system and is closely approximated by the signal that occurs with the arrival of the shock wave at the transducer location (see Figure E.5). The vortex pressure signal $P_2(t)$ is then given by

$$P_2(t) = A'(t) * P_1(t) \; .$$

The Convolution Theorem gives (see reference [36])

$$P_2(f) = T(f) P_1(f) \; ,$$

where $P_2(f)$ is the Fourier Transform of $P_2(t)$ and where $T(f)$ is the Fourier Transform of $A'(t)$ (often referred to as the transfer function of the system). So it follows that

$$P_2(f) / T(f) = P_1(f) \; .$$

Taking the Inverse Fourier Transform of $P_1(f)$ gives the original unfiltered signal $P_1(t)$ associated with the vortex pressure changes. This process by which $P_1(t)$ is obtained is called *deconvolution* or *inverse filtering*. The signals to be analyzed are sampled at discrete points equally spaced in time. The Discrete Fourier Transforms (DFT) and the Inverse Discrete Fourier Transforms (IDFT) must be computed for the deconvolution process. These operations are defined by [36]:

$$DFT \quad P_2(f) = N^{-1} \sum_{t=0}^{N-1} P_2(t) \, e^{-i2\pi(f/N)t}$$

$$DFT \quad T(f) = N^{-1} \sum_{t=0}^{N-1} A'(t)\, e^{-i2\pi(f/N)t}$$

$$IDFT \quad P_1(f) = \sum_{f=0}^{N-1} \frac{P_2(f)}{T(f)} e^{i2\pi(f/N)t}$$

E.6.2 Procedure

For the deconvolution of the pressure signal it is necessary to calculate the Fourier Transform of both the pressure signal and the impulse-response. Then an Inverse Fourier Transform of the ratio of these results is calculated to reveal the inverse-filtered signal $P_1(t)$. The Fast Fourier Transform algorithm (FFT) is used for these computations (see reference [36]) which are done on a digital computer.

The signal to be processed is the digitized vortex pressure response $P_2(t)$, which is plotted in Figure E.6. In order to use the FFT algorithms, the signal must be sampled at equal intervals of time. As shown in Figure E.7, the signal is sampled by 85 points which correspond to intervals that are 1 micro-sec apart. This particular sampling rate (1 MHZ) can resolve frequency components of the signal up to 500 khz, which is more than sufficient to re-solve the true vortex signal. Tables E.1 and E.2 contain the actual values of pressure in psi units spanning a range of time from 0 to 84 micro-sec in 1 micro-sec steps. This information is plotted in Figure E.7. These tables also contain the transformed values of these same sampled pressure points $P_2(r)$, which are used in the raw data calculations in Chapter 4. The trans-formation factors given in Table E.1 transform these points into a spatial pressure distribution given in units of N/m^2 (in .018 cm steps). The zero ref-erence for the spatial distribution is taken at the minimum value of pressure and is defined as the center of the vortex. Figure E.8 shows a plot of the digitized shock pressure response $A(t)$ (pressure signal #4) shown in Figure E.5. This signal is sampled at the same rate as $P_2(t)$ at 12 points. The Impulse Pressure Response $A'(t)$ is plotted in Figure E.9 and is computed

by a first-difference algorithm. The FFT algorithm is then used on the two sampled responses $P_2(t)$ and $A'(t)$ which yield the frequency spectra of these signals given by $P_2(f)$ and $T(f)$ respectively. The FFT results are given in Figure E.10, which is a plot of the power spectra of $P_2(f)$, $T(f)$ and the ratio $\frac{P_2(f)}{T(f)}$. The Inverse FFT is then performed on this ratio which yields the final result $P_1(t)$, which is plotted in Figure E.11. In Figure E.12 both $P_1(t)$ and $P_2(t)$ are plotted for comparison. The individual points in the plot are the sampled points of $P_2(t)$ that were originally plotted in Figure E.7 and the solid line in this plot represents a cubic-spline fit to the deconvolved signal points of $P_1(t)$. Inspection of Figure E.12 reveals that the major effect of the deconvolution process is a 10 percent additional drop in pressure at the vortex center. This corrected pressure signal is then transformed into a spatial distribution by the Galilean transformation factor .018 cm/micro-sec which is derived from direct measurements of the vortex velocity (see Appendix D). In Figure E.13 both $P_2(r)$ (the original vortex pressure distribution used for raw data calculations) and $P_1(r)$ (the deconvolved vortex pressure distribution) are plotted and compared. The solid line in Figure E.13 represents the original unprocessed pressure data and the points in the plot represent the discrete deconvolved pressure information.

E.6.3 Remarks About Transducer Dimensions

The entire deconvolution process corrected for the limited time-response of the system, which was characterized by an approximation of the step-response of the system using the signal from the passing shock wave. The physical size of the transducer also has an effect on the accuracy of the data since it averages the pressure over the aperture of its width. This effect, combined with the effect of the time-response of the transducer and supporting electronics, contributes to the total error of the signal. It is difficult to separate these effects. The pure aperature spreading effect of the pressure distribution due to the physical dimensions of the transducer could be determined
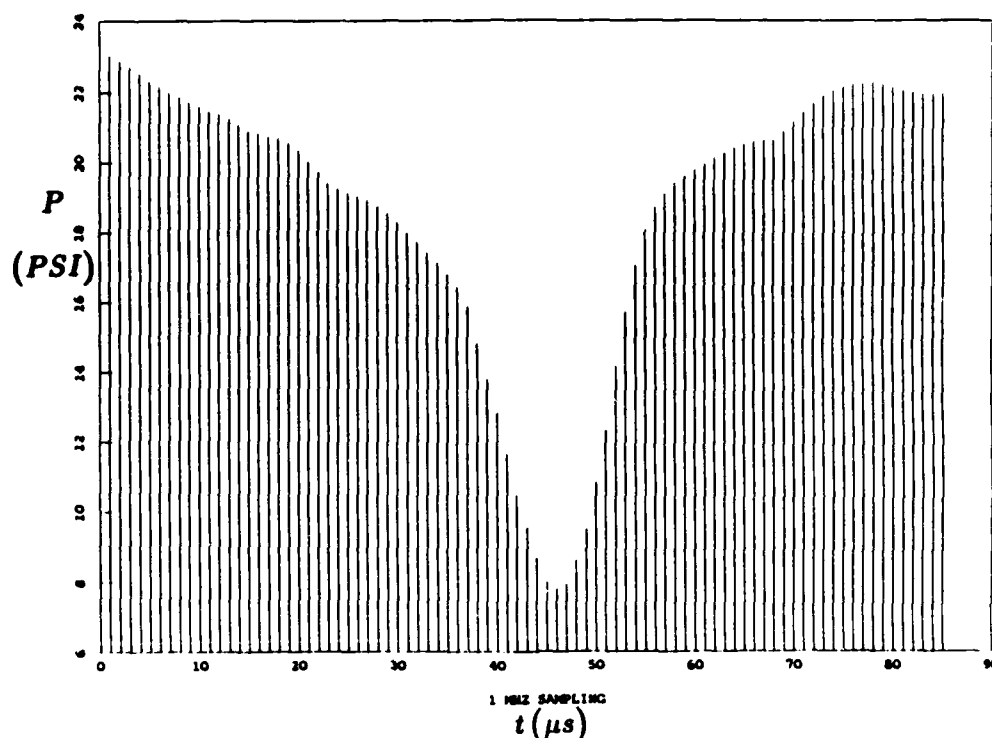
Figure E.7: 1 MHZ Sampling of Pressure Signal #3.

by the step-response analysis method only if the system had unlimited time-response. Also, the pure time-response of the system could be determined independently by the step-response analysis method only if the transducer was infinitesimally small.   Since the shock wave signal itself contains both these spatial and time domain effects, then the deconvolution process may then partially correct for both effects. The operative width of the transducer is approximately 0.7 mm. If the system had unlimited time-response, then only the effect of the transducer size would be seen and a signal would occur with a rise time of about 1.4 micro-sec as the shock passes by at a speed of 500 m/sec; thus, the spreading of the signal is due mostly to the limited time-response of the transducer as opposed to its physical size (see Pressure Signal #4, Figure E.5).
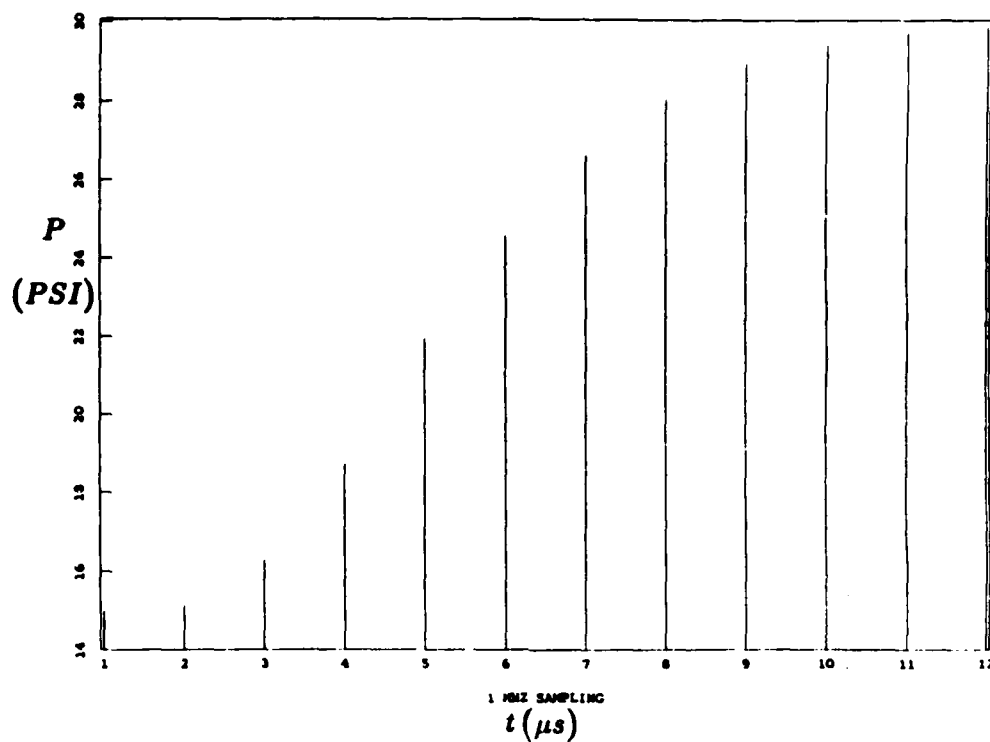
Figure E.8: 1 MHZ Sampling of Pressure Signal #4.
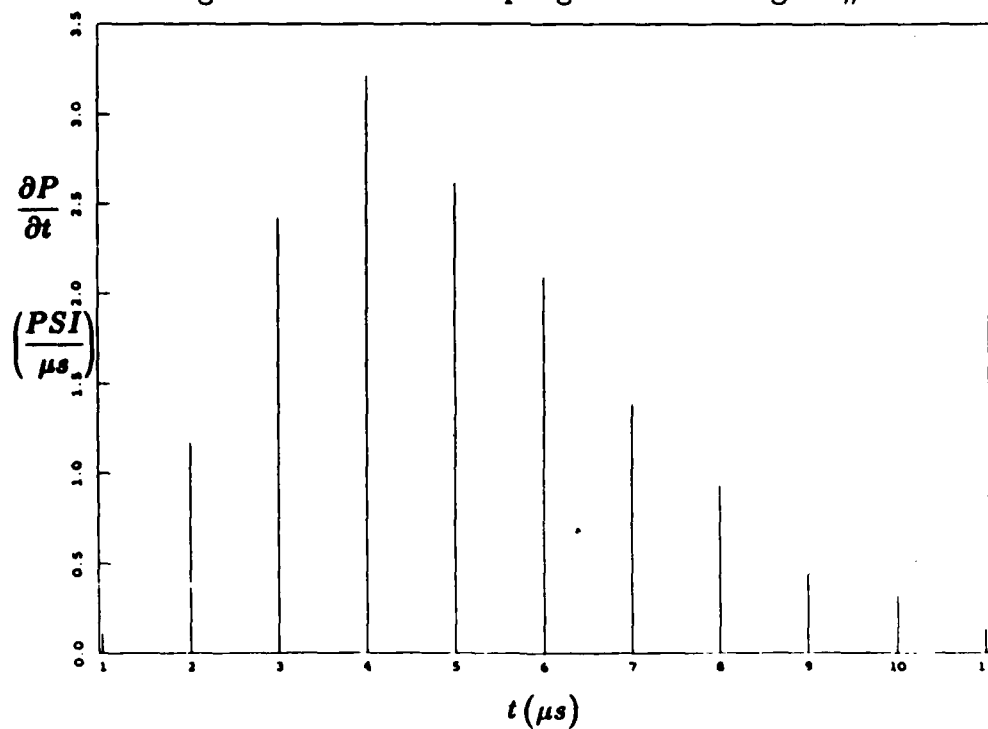
Figure E.9: Approximation of Impulse Pressure Response.

PRESSURE DATA SAMPLED AT 1 MICROSECOND INTERVALS (VORTEX)

t(micro-s)	P(psi)		CM	N/M^2
-----	----------		-------	--------
0	23.06877		0.810	159059.1
1	22.89439	TRANSFORMATION:	0.792	157856.8
2	22.73813	t->r : .0180 cm/micro-s	0.774	156779.4
3	22.55391		0.756	155509.2
4	22.35178	P->P : 6895 N/M^2/PSI	0.738	154115.5
5	22.18188		0.720	152944.0
6	22.03187		0.702	151909.7
7	21.88905		0.684	150925.0
8	21.75342		0.666	149989.8
9	21.62602		0.648	149111.4
10	21.51064		0.630	148315.8
11	21.39502		0.612	147518.6
12	21.27928		0.594	146720.6
13	21.09132		0.576	145424.6
14	20.92726		0.558	144293.4
15	20.84855		0.540	143750.7
16	20.77961		0.522	143275.4
17	20.72079		0.504	142869.8
18	20.58317		0.486	141920.9
19	20.37637		0.468	140495.0
20	20.07797		0.450	138437.6
21	19.76309		0.432	136266.5
22	19.43670		0.414	134016.0
23	19.26998		0.396	132866.5
24	19.16022		0.378	132109.7
25	19.06720		0.360	131468.3
26	18.95789		0.342	130714.6
27	18.77330		0.324	129441.9
28	18.58871		0.306	128169.1
29	18.30822		0.288	126235.1
30	18.01242		0.270	124195.6
31	17.73384		0.252	122274.8
32	17.43378		0.234	120205.9
33	17.12862		0.216	118101.8
34	16.82456		0.198	116005.3
35	16.46084		0.180	113497.5
36	15.91607		0.162	109741.3
37	14.83230		0.144	102268.7
38	13.80935		0.126	95215.47
39	12.83051		0.108	88466.37
40	11.68249		0.090	80550.78
41	10.48747		0.072	72311.10
42	9.56520		0.054	65952.06
43	8.68382		0.036	59874.94
44	8.00552		0.018	55198.06
45	7.82053		0.0	53922.55
46	7.76915		-0.018	54947.29

Table E.1: Digitized Raw Pressure Signal and t→r Transformation.

t(micro-s)	P(psi)		CM	N/M^2
47	8.64044		-0.036	59575.83
48	9.52338		-0.054	65663.71
49	10.84715		-0.072	74791.10
50	12.34971		-0.090	85151.25
51	14.18946		-0.108	97836.33
52	15.72848		-0.126	108447.8
53	17.06426		-0.144	117658.0
54	18.10448		-0.162	124830.4
55	18.72176		-0.180	129086.5
56	19.11525		-0.198	131799.6
57	19.41758		-0.216	133884.2
58	19.62469		-0.234	135312.2
59	19.79001		-0.252	136452.1
60	19.95552		-0.270	137593.3
61	20.12363		-0.288	138752.4
62	20.29173		-0.306	139911.4
63	20.42717		-0.324	140845.3
64	20.54176		-0.342	141635.4
65	20.60919		-0.360	142100.3
66	20.64198		-0.378	142326.4
67	20.67477		-0.396	142552.5
68	20.92297		-0.414	144263.8
69	21.17996		-0.432	146035.8
70	21.45937		-0.450	147962.3
71	21.70764		-0.468	149674.1
72	21.92583		-0.486	151178.6
73	22.06986		-0.504	152171.6
74	22.17297		-0.522	152882.6
75	22.24795		-0.540	153399.6
76	22.26383		-0.558	153509.1
77	22.27970		-0.576	153618.5
78	22.23445		-0.594	153306.5
79	22.15669		-0.612	152770.3
80	22.07943		-0.630	152237.6
81	22.00590		-0.648	151730.6
82	21.93237		-0.666	151223.6
83	21.94523		-0.684	151312.3
84	21.97783		-0.702	151537.1

Table E.2: (Continuation) Digitized Raw Pressure Signal and t→r Transformation.
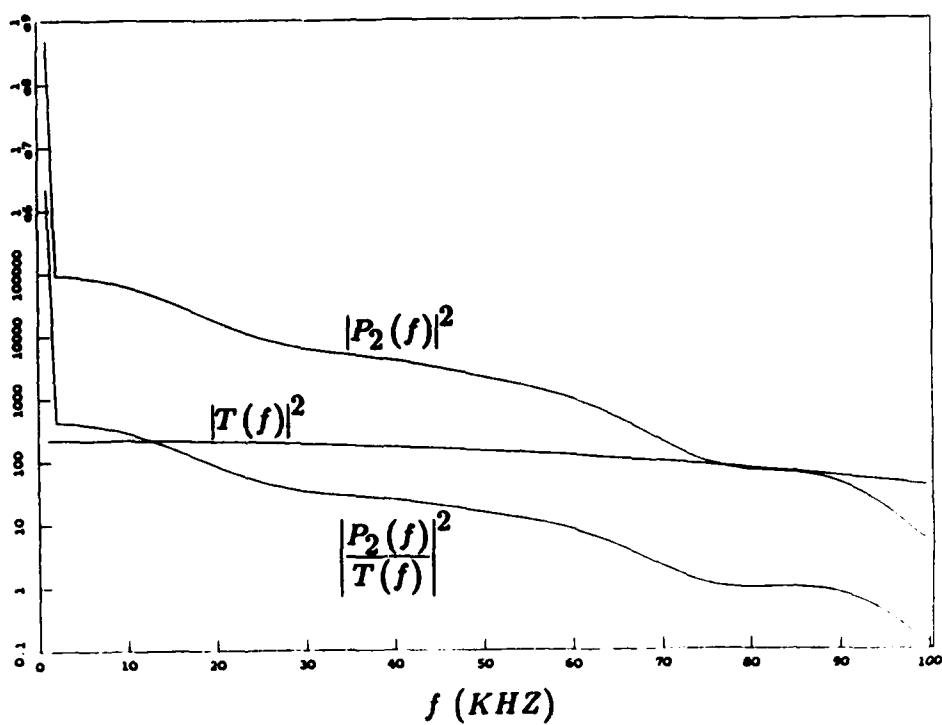
Figure E.10: Power Spectra From FFT Processing.
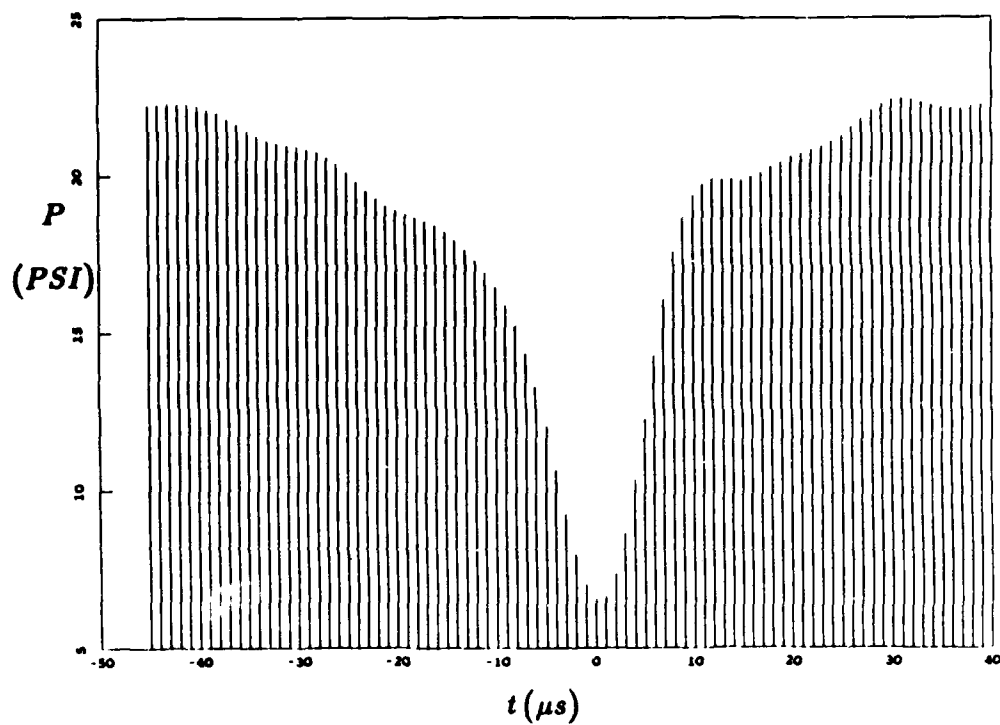
Figure E.11: Deconvolved Pressure Response.

ORIGINAL SIGNAL, (*), and DECONVOLVED SIGNAL, (solid line)
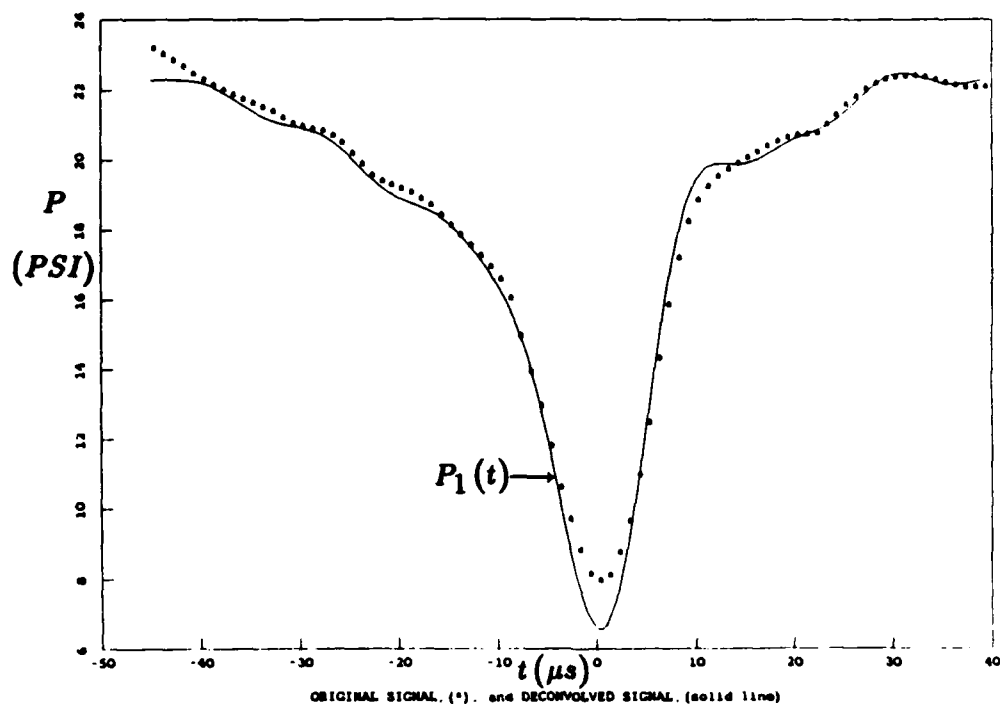
Figure E.12: Superposition of Deconvolved Pressure Response and Original Signal.
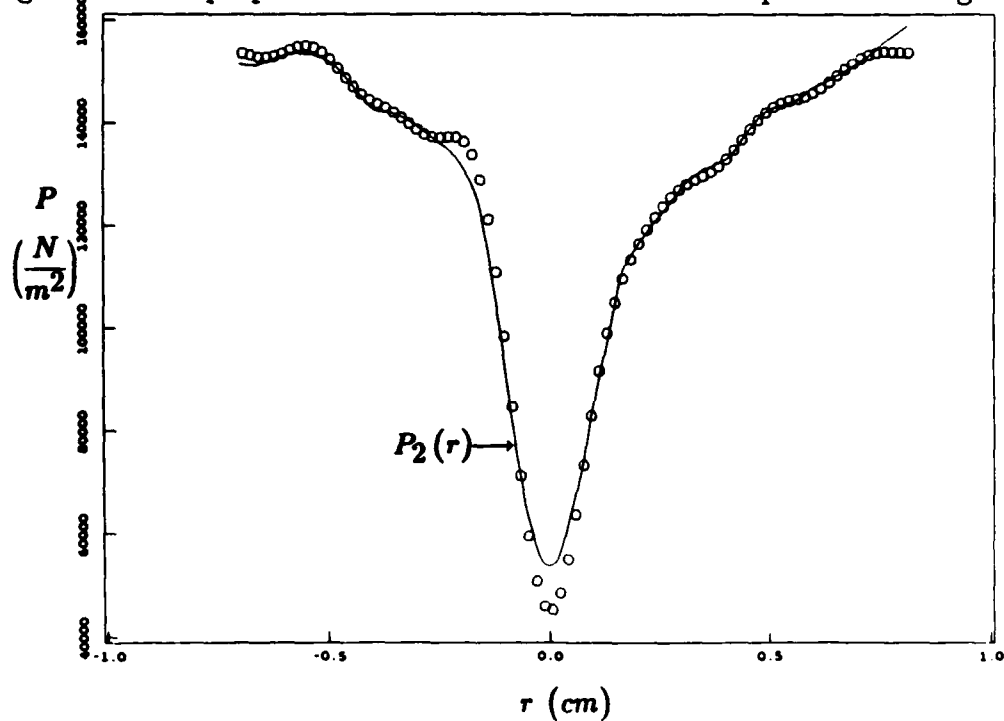
Figure E.13: Radial Distribution of Pressure by Transformation of Deconvolved Pressure Response and Original Signal.

E.7 Curve Fitting and Model Testing

The 85 points which represent the corrected spatial pressure distribution $P_1(r)$ (plotted in Figure E.13) are tabulated in Tables E.3 and E.4. These tables also contain the results of the best-fit model which was found using the curve fitting routine described in Appendix F. A modified form of the Cauchy distribution (described in Chapter 3) is used to approximate the pressure data in the form of a mathematical formula. This results in a compact and convenient form of the data which is then used in further calculations of additional physical properties of the vortex. The points and the fitted curve are plotted in Figure 3.9, Chapter 3. The RMS value of the residuals, which indicates the closeness-of-fit, is given in the tables. A homentropic model of the vortex (described in Chapter 3) was also tested for closeness-of-fit in Tables E.5 and E.6 in order to investigate a possible homentropic relationship between the density and the pressure in the vortex. The results contained in these tables are plotted in Figure 3.10, Chapter 3. The RMS value of the residuals in this test is given in the tables.

LEAST SQUARES CURVE FIT TO PRESSURE DATA

RMS(DIFF)=6601 N/M^2

r (cm)	P(data)	P(model)	DIFF	(DIFF)^2
0.8130080	153702.0	149919.0	-3783.060	14311600.
0.7950739	153771.0	149821.0	-3949.860	15601400.
0.7771400	153818.0	149717.0	-4100.980	16818100.
0.7592060	153789.0	149606.0	-4182.640	17494500.
0.7412719	153615.0	149487.0	-4127.910	17039600.
0.7233380	153229.0	149359.0	-3870.450	14980400.
0.7054039	152583.0	149222.0	-3361.700	11301000.
0.6874700	151670.0	149074.0	-2595.750	6737920.
0.6695360	150529.0	148914.0	-1614.450	2606460.
0.6516020	149255.0	148742.0	-512.875	263041.0
0.6336679	147974.0	148556.0	581.531	338179.0
0.6157340	146815.0	148354.0	1538.590	2367270.
0.5978000	145878.0	148134.0	2256.160	5090240.
0.5798659	145194.0	147895.0	2700.700	7293800.
0.5619320	144720.0	147633.0	2913.550	8488760.
0.5439980	144334.0	:47347.0	3012.830	9077130.
0.5260639	143871.0	147033.0	3161.800	9996960.
0.5081300	143163.0	146687.0	3524.580	12422700.
0.4901959	142087.0	146306.0	4218.450	17795300.
0.4722620	140611.0	145883.0	5272.140	27795500.
0.4543280	138799.0	145414.0	6615.140	43760100.
0.4363940	136803.0	144891.0	8088.420	65422600.
0.4184600	134821.0	144306.0	9485.111	89967296.
0.4005259	133044.0	143648.0	10604.50	112455000.
0.3825919	131595.0	142907.0	11311.40	127949000.
0.3646579	130499.0	142067.0	11568.30	133825008.
0.3467240	129672.0	141111.0	11439.60	130864000.
0.3287900	128948.0	140019.0	11070.60	122558000.
0.3108560	128133.0	138763.0	10629.40	112985000.
0.2929220	127056.0	137311.0	10255.60	105177000.
0.2749880	125620.0	135625.0	10005.70	100115000.
0.2570539	123806.0	133655.0	9849.090	97004608.
0.2391200	121664.0	131340.0	9676.500	93634704.
0.2211859	119243.0	128604.0	9361.111	87630392.
0.2032520	116542.0	125354.0	8812.701	77663696.
0.1853179	113444.0	121476.0	8031.920	64511800.
0.1673840	109715.0	116835.0	7119.240	50683600.
0.1494500	105037.0	111276.0	6239.700	38933900.
0.1315159	99105.3	104643.0	5538.130	30670900.
0.1135820	91752.4	96806.4	5053.980	25542800.
0.09564801	83072.7	87732.2	4659.550	21711400.
0.07771400	73506.5	77602.3	4095.810	16775700.
0.05978000	63849.2	66977.8	3128.570	9787950.
0.04184600	55170.6	56947.6	1777.060	3157940.

Table E.3: Least Squares Best-Fit Curve to Deconvolved Data.

r (cm)	P(data)	P(model)	DIFF	(DIFF)^2
0.02391200	48650.2	49094.0	443.793	196952.0
0.00597799	45359.4	45078.8	-280.563	78715.3
-0.01195600	46039.1	45906.7	-132.367	17521.1
-0.02989000	50925.7	51361.6	435.883	189994.0
-0.04782400	59671.8	60134.8	462.996	214365.0
-0.06575800	71384.1	70518.8	-865.359	748847.0
-0.08369200	84774.5	81071.4	-3703.110	13713000.
-0.1016260	98392.6	90889.3	-7503.350	56300300.
-0.1195600	110886.0	99557.6	-11328.00	128324000.
-0.1374940	121227.0	106983.0	-14244.40	202902000.
-0.1554280	128868.0	113241.0	-15627.30	244212000.
-0.1733620	133770.0	118476.0	-15293.90	233904000.
-0.1912959	136337.0	122846.0	-13490.00	181981008.
-0.2092300	137254.0	126501.0	-10753.10	115629992.
-0.2271640	137297.0	129568.0	-7728.910	59736100.
-0.2450979	137146.0	132155.0	-4991.340	24913500.
-0.2630319	137258.0	134347.0	-2910.470	8470830.
-0.2809660	137819.0	136216.0	-1602.450	2567860.
-0.2989000	138784.0	137819.0	-964.547	930351.0
-0.3168339	139963.0	139201.0	-762.047	580715.0
-0.3347680	141137.0	140399.0	-737.219	543492.0
-0.3527019	142154.0	141444.0	-709.750	503745.0
-0.3706359	142989.0	142359.0	-630.031	396939.0
-0.3885700	143737.0	143164.0	-573.047	328383.0
-0.4065040	144567.0	143876.0	-691.078	477589.0
-0.4244379	145644.0	144508.0	-1135.420	1289180.
-0.4423719	147055.0	145072.0	-1983.340	3933650.
-0.4603059	148768.0	145576.0	-3191.310	10184500.
-0.4782400	150623.0	146029.0	-4593.660	21101698.
-0.4961740	152386.0	146437.0	-5948.690	35386900.
-0.5141079	153808.0	146806.0	-7001.660	49023200.
-0.5320420	154703.0	147141.0	-7562.300	57188300.
-0.5499760	155007.0	147445.0	-7561.770	57180300.
-0.5679100	154786.0	147723.0	-7063.330	49890600.
-0.5858439	154226.0	147977.0	-6249.480	39056100.
-0.6037780	153565.0	148209.0	-5355.530	28681700.
-0.6217120	153029.0	148423.0	-4606.170	21216800.
-0.6396460	152775.0	148620.0	-4154.950	17263600.
-0.6575800	152843.0	148801.0	-4041.970	16337500.
-0.6755139	153169.0	148969.0	-4200.270	17642200.
-0.6934480	153615.0	149124.0	-4490.440	20164000.

Table E.4: (Continuation) Least Squares Best-Fit Curve to Deconvolved Data.

VORTEX RADIAL PRESSURE PROFILE

RMS(DIFF)=11107 N/m^2

r (cm)	EXP.DATA P (N/m^2)	DENSITY (kg/m^3)	HOMENTROPIC MODEL P (N/m^2)	(DIFF)	(DIFF)^2
8.130080	153702.0	1.744160	157355.0	3653.000	13344410
7.950738	153771.0	1.742290	157119.0	3348.000	11209105
7.771399	153818.0	1.740290	156867.0	3049.000	9296402
7.592060	153789.0	1.738160	156598.0	2809.000	7890481
7.412720	153615.0	1.735880	156311.0	2696.000	7268416
7.233378	153229.0	1.733440	156003.0	2774.000	7695076
7.054039	152583.0	1.730830	155674.0	3091.000	9554282
6.874700	151670.0	1.728020	155321.0	3651.000	13329802
6.695360	150529.0	1.725010	154941.0	4412.000	19465744
6.516018	149255.0	1.721760	154533.0	5278.000	27857284
6.336678	147974.0	1.718250	154092.0	6118.000	37429924
6.157340	146815.0	1.714460	153617.0	6802.000	46267204
5.978000	145878.0	1.710360	153102.0	7224.000	52186176
5.798658	145194.0	1.705910	152545.0	7351.000	54037200
5.619318	144720.0	1.701070	151939.0	7219.000	52113960
5.439980	144334.0	1.695800	151281.0	6947.000	48260808
5.260640	143871.0	1.690040	150562.0	6691.000	44769480
5.081298	143163.0	1.683740	149778.0	6615.000	43758224
4.901958	142087.0	1.676840	148918.0	6831.000	46662560
4.722620	140611.0	1.669250	147975.0	7364.000	54228496
4.543280	138799.0	1.660880	146938.0	8139.000	66243320
4.363938	136803.0	1.651630	145794.0	8991.000	80838080
4.184598	134821.0	1.641380	144529.0	9708.000	94245264
4.005259	133044.0	1.629990	143127.0	10083.00	101666888
3.825920	131595.0	1.617310	141570.0	9975.000	99500624
3.646579	130499.0	1.603130	139835.0	9336.000	87160896
3.467240	129672.0	1.587240	137898.0	8226.000	67667080
3.287899	128948.0	1.569380	135731.0	6783.000	46009088
3.108560	128133.0	1.549250	133300.0	5167.000	26697890
2.929220	127056.0	1.526510	130569.0	3513.000	12341170
2.749880	125620.0	1.500760	127496.0	1876.000	3519376
2.570538	123806.0	1.471540	124035.0	229.000	52441
2.391200	121664.0	1.438360	120136.0	-1528.000	2334784
2.211858	119243.0	1.400650	115751.0	-3492.000	12194065
2.032520	116542.0	1.357860	110830.0	-5712.000	32626944
1.853180	113444.0	1.309430	105335.0	-8109.000	65755880
1.673840	109715.0	1.254920	99248.8	-10466.20	109541408
1.494500	105037.0	1.194150	92585.0	-12452.00	155052304
1.315160	99105.3	1.127320	85413.6	-13691.69	187462528
1.135820	91752.4	1.055380	77881.5	-13870.39	192401824
0.9564801	83072.7	0.980284	70234.9	-12837.80	164809232
0.7771400	73506.5	0.905294	62829.9	-10676.60	113989824
0.5978000	63849.2	0.835118	56118.6	-7730.598	59762140
0.4184600	55170.6	0.775619	50602.1	-4568.500	20871192
0.2391200	48650.2	0.732989	46751.7	-1898.500	3604302

Table E.5: Homentropic Test of Deconvolved Pressure Data.

r (cm)	EXP.DATA P (N/m^2)	DENSITY (kg/m^3)	HOMENTROPIC MODEL P (N/m^2)	(DIFF)	(DIFF)^2
0.0597799	45359.4	0.712401	44923.6	-435.797	189919
-0.1195600	46039.1	0.716583	45293.3	-745.801	556219
-0.2989000	50925.7	0.744968	47824.8	-3100.898	9615572
-0.4782400	59671.8	0.793877	52277.5	-7394.301	54675684
-0.6575800	71384.1	0.857630	58247.9	-13136.20	172559840
-0.8369200	84774.5	0.930017	65245.1	-19529.39	381397408
-1.016260	98392.6	1.005500	72776.7	-25615.89	656174272
-1.195600	110886.0	1.079830	80419.3	-30466.70	928219968
-1.374940	121227.0	1.150230	87853.2	-33373.79	1113810e3
-1.554280	128868.0	1.215100	94867.4	-34000.60	1156040e3
-1.733620	133770.0	1.273790	101343.0	-32427.00	1051510336
-1.912960	136337.0	1.326230	107232.0	-29105.00	847101056
-2.092298	137254.0	1.372720	112532.0	-24722.00	611177280
-2.271640	137297.0	1.413760	117270.0	-20027.00	401080736
-2.450978	137146.0	1.449890	121487.0	-15659.00	245204288
-2.630320	137258.0	1.481700	125235.0	-12023.00	144552528
-2.809659	137819.0	1.509710	128561.0	-9258.000	85710568
-2.989000	138784.0	1.534410	131515.0	-7269.000	52838360
-3.168339	139963.0	1.556230	134142.0	-5821.000	33884040
-3.347680	141137.0	1.575570	136481.0	-4656.000	21678336
-3.527019	142154.0	1.592740	138568.0	-3586.000	12859397
-3.706360	142989.0	1.608030	140434.0	-2555.000	6528025
-3.885700	143737.0	1.621690	142107.0	-1630.000	2656900
-4.065040	144567.0	1.633930	143610.0	-957.000	915849
-4.244379	145644.0	1.644920	144965.0	-679.000	461041
-4.423718	147055.0	1.654820	146188.0	-867.000	751689
-4.603058	148768.0	1.663760	147295.0	-1473.000	2169729
-4.782400	150623.0	1.671860	148300.0	-2323.000	5396329
-4.961740	152386.0	1.679210	149214.0	-3172.000	10061585
-5.141078	153808.0	1.685910	150047.0	-3761.000	14145122
-5.320418	154703.0	1.692020	150809.0	-3894.000	15163237
-5.499760	155007.0	1.697600	151507.0	-3500.000	12250001
-5.679100	154786.0	1.702730	152147.0	-2639.000	6964321
-5.858438	154226.0	1.707430	152736.0	-1490.000	2220100
-6.037778	153565.0	1.711760	153278.0	-287.000	82369
-6.217120	153029.0	1.715760	153779.0	750.000	562500
-6.396460	152775.0	1.719450	154243.0	1468.000	2155024
-6.575798	152843.0	1.722870	154672.0	1829.000	3345241
-6.755138	153169.0	1.726040	155071.0	1902.000	3617604
-6.934480	153615.0	1.728980	155441.0	1826.000	3334276

Table E.6: (Continuation) Homentropic Test of Deconvolved Pressure Data.

Bibliography

[1] J.D. JACKSON. *Classical Electrodynamics*, pages 681–682. John Wiley and Sons, 1975.

[2] E.J. GRATH, P.J.E. PEEBLES, R.M. SEDNER, and R.M. SONEIRA. The Clustering of Galaxies. *Sci. Am.*, 237:76–80, November 1977.

[3] H.J. LUGT. *Vortex Flow in Nature and Technology.* John Wiley and Sons, 1983.

[4] M. MANDELLA and D. BERSHADER. Detailed Structure of a Free Compressible Vortex in Uniform Motion. In *Thirty-Ninth Meeting of the American Physical Society, Division of Fluid Dynamics*, November 23-25 1986.

[5] M.J. MANDELLA and D. BERSHADER. Quantitative Study of the Compressible Vortex: Generation, Structure and Interaction with Air-foils. In *AIAA 25th Aerospace Sciences Meeting*, January 1987.

[6] P.A. THOMPSON. *Compressible-Fluid Dynamics*, pages 633–635. McGraw-Hill, 1972.

[7] D. KUCHEMANN. Report on the I.U.T.A.M. Symposium on Concentrated Vortex Motions. *J. Fluid Mech.*, 21 (part 1): 1–20, 1965.

[8] M.G. HALL. The Structure of Concentrated Vortex Cores. *Progress in Aeronautical Sciences*, 7:53–109, 1965.

[9] D. KUCHEMANN and J WEBER. Vortex Motions. *ZAMM*, 45:457–474, 1965.

[10] S.N. BROWN. The Compressible Inviscid Leading Edge Vortex. *J. Fluid Mech.*, 22:17–32, 1965.

[11] L.N. HOWARD and D.L. MATTHEWS. On the Vortices Produced in Shock Diffraction. *J. Appl. Phys.*, 27:223–231, 1956.

[12] W. MERZKIRCH. Theoretische und Experimenelle Untersuchungen an einer Instationaren Wirbelstromung. *Z. Flugw.*, 12:395–401, 1964.

[13] J.M. BURGERS. A Mathematical Model Illustrating the Theory of Turbulence. *Adv. Appl. Mech.*, 1:171–199, 1948.

[14] N. ROTT. On the Viscous Core of a Line Vortex. *ZAMP*, 9:543–553, 1958.

[15] N. ROTT. On the Viscous Core of a Line Vortex II. *ZAMP*, 10:73–81, 1959.

[16] L.M. MILNE-THOMSON. *Theoretical Hydrodynamics*, pages 353–354. Macmillan New York, 1968.

[17] G.I. TAYLOR. On the Dissipation of Eddies. *Aero. Res. Comm.*, R and M No. 598, 1918.

[18] H. LAMB. *Hydrodynamics*. 6th ed. Dover, New York, 1945.

[19] G.I. TAYLOR. Recent Work on the Flow of Compressible Fluids. *J. Lond. Math. Soc.*, 5:224–240, 1930.

[20] L.M. MACK. The Compressible Viscous Heat-Conducting Vortex. *J. Fluid Mech.*, 8:284–292, 1960.

[21] W.G. VINCENTI and C.H. KRUGER. *Introduction to Physical Gas Dynamics*, pages 22–23. Krieger Publishing Co., 1982.

[22] W.R. VON KARMAN, and T. SEARS. Airfoil Theory for Non-Uniform Motion. *J. Aeronautical Sciences*, 5:379–389, 1938.

[23] M.A. HOLLINGSWORTH and E.J. RICHARDS. *A Schlieren Study of the Interaction Between a Vortex and a Shockwave in a Shock Tube*. Technical Report No. 17985, Aeronautical Research Council, Nov. 1955.

[24] M.A. HOLLINGSWORTH and E.J. RICHARDS. *On the Sound Generated by the Interaction of a Vortex and a Shockwave.* Technical Report No. 18257, Aeronautical Research Council, Feb. 1956.

[25] D.S. DOSANJH and T.M. WEEKS. Interaction of a Starting Vortex as Well as a Vortex Street With a Traveling Shock Wave. *AIAA Journal,* 3:216–223, 1965.

[26] G.E.A. MEIER. *Transonic Noise Generation by Duct and Profile Flow.* Technical Report, European Research Office of the U.S. Army, April 1984.

[27] R. TIMM. *Schallentstehung bei der Wechselwirkung von Wirbeln mit einer Tragflugelumstromung.* Technical Report No. 80, Max Planck Institut fur Stromungsforschung, 1985.

[28] H.M. LENT. *Schallentstehungsmechanismen in Transsonischen Stromungen beim Auftreffen von Wirbeln auf eine Profilvorderkante.* Diplomarbeit, Max Planck Institut fur Stromungsforschung, 1986.

[29] M.J. MANDELLA and D. BERSHADER. Holographic Interferometric Studies of Shock-Generated Vortex Flows. In *37th Annual Meeting of the Div. of Fluid Dynamics, Providence, RI, November 18-20,* 1984.

[30] C.M. VEST. *Holographic Interferometry.* Wiley-Interscience, 1979.

[31] R.J. COLLIER, C.B. BURCKHARDT, and L.H. LIN. *Optical Holography,* pages 11–12. Academic Press, 1971.

[32] P. HARIHARAN. *Optical Holography: Principles, Techniques and Applications,* pages 89–90. Cambridge University Press, 1986.

[33] G. BLENDSTRUP, D. BERSHADER, and P. LANGHOFF. Recent Results of Resonant Refractivity Studies for Improved Flow Visualization. In *Shock Tubes and Waves,* pages 258–265, 12th International Symposium on Shock Tubes and Waves, 1979.

[34] M. BORN and F. WOLF. *Principles of Optics,* page 122. Pergamon Press, 1985.

[35] Y.J. MOON. Numerical Simulation by TVD Schemes of Complex Shock Reflections From Airfoils at High Angle of Attack. In *AIAA 25th Aerospace Sciences Meeting*, January 1987.

[36] R.N. BRACEWELL. *The Fourier Transform and its Applications.* McGraw-Hill, 1978.

[37] A.G. WORTHING and J. GEFFNER. *Treatment of Experimental Data.* Wiley and Sons.

[38] J. PENDER. *Parametric Oscillation in Sodium Flames.* PhD Thesis, Stanford University, Dept. of Applied Physics, 1987.

[39] J.B. SCARBOROUGH. *Numerical Mathematical Analysis.* John Hopkins Press, 1962.

[40] W.J. McCROSKEY. Unsteady Airfoils. *Annual Review of Fluid Mechanics.* (M. VanDyke, et al, Ed.), Vol. 14, 285-311, 1982.

[41] H. TIJDEMAN and R. SEEBASS. Transonic Flow Past Oscillating Airfoils. Ibid. Vol. 12, 181-222, 1980.

[42] Summary Notes of the Workshop on Blade Vortex Interactions. NASA-Ames Research Center. Notebooks I and II. October 29-31, 1984.

ADDENDUM

BRIEF ASSESSMENT OF RECENT LITERATURE
ON BLADE-VORTEX INTERACTIONS

Since the blade-vortex interaction is the principal application for the results of the present study, one may ask about the current status of BVI research. Currently, it is a most active field of study, a substantial amount of which has been stimulated by the interest of ARO. The high degree of complexity is well-known and stems from the basic 3-D non-steady character of the flow field. Superimposed on these features are compressibility effects associated with the transonic nature of the flow around advancing rotor tips; and also dissipative behavior associated with the vortex structure as well as the role of viscous/turbulent boundary layers in the BVI. Classical vortex theory applied to BVI also has difficulties with the application of the Kutta condition. Basic modifications are required in order to apply theory. Somehow, one must incorporate the phenomena just mentioned to yield the aerodynamic performance, transient and vibratory pressure loading and the generation of acoustic radiation. As we know, the theoretical approach has, of necessity, been supplemented by other studies; and the totality of recent and current investigations has indeed resulted in an increased level of understanding of BVI.

In a somewhat oversimplified way, studies of BVI can be characterized by either one or a combination of the following categories: (1) theoretical, (2) computational, (3) experimental -- large scale or flight, (4) experimental -- basic laboratory studies. Recent activity has included all these categories. In this brief overview, reference will be made to those studies which are especially relevant to the work proposed here.

A program which complements the Stanford vortex interaction investigation is that being pursued by Dr. G. Meier and associates in Göttingen.[1,2,3] They have investigated the interaction of a Karman vortex street with a suitable profile in a transonic tunnel; and also the interaction of single vortices with an airfoil, using a shock tube. The special emphasis in their work is on the generation of sound. Measurements were made by pressure devices and Mach-Zehnder interferometry, including a special method for digital fringe analysis

The Göttingen group reports several interesting results, but the inference is evident that further confirmation, analysis and understanding are in order. Some principal points of interest are:

(1) In all the studies (including the BVI investigations to date here at Stanford), it is clear that lateral displacement of the vortex path from the stagnation streamline of the airfoil flow is a prime parameter. Head-on or nearly head-on "collisions" produce major changes in vortex configuration, associated with very strong transient pressure loading on the airfoil. What needs further assessment is the role of the boundary layer in the BVI.[4] Meier feels that the latter plays an important role in the wind-tunnel case. The Stanford work has shown that viscosity plays a relatively minor role in the structure of the free vortex. Further, the stagnation region boundary layer in either the wind tunnel or shock tube case will be very narrow in high Reynolds number flows; so the effect of the boundary layer may not be a major one, unless one assumes that the secondary vortex is necessarily an outgrowth of a separated boundary layer. Again, this feature is part of the basic question of the role of viscosity/turbulence in the BVI.

(2) The generation of acoustic waves following head-on BVI is observed. *These waves are generated by successive pressure decreases and increases at or near the stagnation region during BVI.*

(3) Theoretical models for calculation of the vortex paths tend to show them following the streamlines - approximately. These models, based on potential theory, do not show good agreement with experiment, however. (Recent work at Stanford has shown that the vortex trajectory is very sensitive to the lateral displacement parameter mentioned in (1) above, and to the angle of attack as well.

A central function of the experimental studies such as those at Göttingen and Stanford is to provide reference results to the numerical/CFD programs for code validation purposes. Clearly, CFD will have to continue to be a principal approach to this complex problem. During the past four years, several techniques for

performing finite-difference calculations on flows containing concentrated vorticity have been reported in the literature; see, for example, the paper by Fujii and Kutler.[5] More recently, Srinivasan and McCroskey[6] have used a "vortex-fitting" method in which the structure of the vortex is specified as a perturbation, while its path develops as part of the solution. (Presumably, this approach could make use of some of the experimental results for free-vortex structure reported by Mandella and Bershader.[7]) These authors used three different computational approaches based, respectively, on the thin-layer Navier-Stokes, the Euler and the transonic small-disturbance (TSD) methods. A significant inference from comparison of the results of the several approaches is that viscous effects are small except for strong interactions outside the scope of the assumptions made. Important physical deductions: (i) the changing angle of attack resulting from the downwash to upwash switch in the interaction, (this phenomenon has also been observed in the Stanford experiments); (ii) in subsonic flow, lift and pitching moment were more sensitive to vortex position than was the instantaneous pressure distribution; (iii) for the transonic case, the presence of the shock produces greater sensitivity to these quantities, accompanied by a curious non-steady interaction between vortex and shock wave.

An underlying question in much of the work relates to the limitations of the 2-D formulation. In this connection, Srinivasan et al[8] point out that for subcritical flow, 3-D effects are of minor importance but the opposite is true for supercritical flow. This study also related to the experiments of Caradonna, Laub and Tung[9] in which a revolving rotor with two blades in a wind tunnel stream encountered a tip vortex generated upstream by an NACA 0015 wing at angle of attack. These experiments were three-dimensional, of course; further, the blade rotation introduces important time-lag effects which are not simulated by BVI with a stationary airfoil. A proper analysis also requires a detailed knowledge of the structure of the interacting vortex.

Three-dimensional approaches have also been used by Strawn and Caradonna[10], and by Strawn and Tung.[11] The former study developed a program using a finite-difference procedure to solve a conservative formulation of the full-potential equation (FPR code) with application to unsteady rotor flowfields. Results obtained for C_p as a function of chord fraction with rotor azimuthal angle as parameter were compared with the experimental findings of reference 9; and also with those obtained by Tung and Chang[12], who implemented a non-conservative formulation of the potential equation. All three sets of results are generally in close

173

agreement, although in the near super-critical case there is some difference as to whether a small shock exists on the rotor or whether the shock has collapsed. These and other studies also confirm the importance of unsteadiness in the shock motion.

In reference 11, the authors build on the analysis of the previous reference to include the effect of rotor wakes on the aerodynamic loading, especially the blade vortex interaction. Some comparison was made with experiment, and realistic results were obtained, including cases of supercritical flows.

On the experimental side, the overwhelming body of previous work has dealt with incompressible vortex flows or vortices on fixed-wing aircraft, especially at high angles of attack. A paper of interest is that of Kaykayoglu and Rockwell[13] who looked at the mechanism of a wedge-type edge interaction with a periodic system of vortices in terms of instantaneous pressure fields in a water flow. They used hydrogen bubble and dye injection techniques, and recorded the flow visualization simultaneously with pressure records, so the two sets of information could be correlated. Major observations are, again, similar in some respects -- but not all -- to what has been seen in air at higher velocities. Near head-on interaction produced distortion or splitting of the primary vortex, secondary vortex formation and shedding from the tip and an upwash to downwash direction switch.

Differences which have been observed in the preliminary compressible flow BVI at studies at Stanford very likely are related to the compressibility factor. Among the few studies exploring this feature is that of D.W. Moore[14] who examines the vortex ring formed by diffraction of a shock wave at the open end of a shock tube. He finds that the speed of the vortex is slowed down by compressibility effects. This type of configuration obeys a local similarity theory, which is different from vortex behavior in the BVI. In Moore's formulation, the entropy is constant across the vortex, whereas the free vortices in the Stanford experiments[15] (no similarity behavior) show a substantial radial variation of entropy. If the pressure distribution be regarded as the forcing function, then the density distribution, and, in that sense, the compressibility is indeed a function of the entropy variation. Thus, the compressibility here is different in nature from that reported by Moore. The basic lesson to be learned from these considerations is that the the vortex analysis where compressibility is present must supplement the classical aerodynamic approach with gasdynamic guidelines.

It is worth noting that modeling of BVI based on experiments with shock-tube

generated vortices can also make use of CFD methods. Yang, Lombard, and Bershader[16] have treated both unsteady 1-D flows and also 2-D shock diffraction phenomena by a time-dependent upwind high resolution scheme applied to the Euler equations. Flow structures included Mach shocks, contact surfaces and vortices. Another example was mentioned in the main proposal, namely the work of Yee and her colleagues in using a TVD scheme - Euler solver.[17] It is anticipated that such work will be extended to the shock-tube BVI studies.

This brief overview of some selected work relating to BVI confirms that much has been learned about the nature of the phenomenon. Other results must still be considered empirical until a deeper understanding is obtained. However, there is now a more substantial framework than existed even at the beginning of this decade to which can be attached guidelines for the continuing research in the subject. The Stanford group plans to make full use of this existing body of knowledge in implementing the research program outlined on page 17(a) of the main proposal.

REFERENCES (ADDENDUM)

1. Timm, R., "Schallenstehung bei der Wechselwirkung von Wirbeln mit einer Tragflügelumströmung," Mitteilungen No. 80, Max Planck Inst. für Strömungsforschung, Göttingen, W. Germany, 1985.

2. Meier, B.E. and Timm, R., "Unsteady Vortex Airfoil Interaction," AGARD CP-386, Paper 16, AGARD Symposium on Unsteady Aerodynamics, May, 1985.

3. Meier, G.E., "Vortex-Airfoil Interaction and Application of Digital Fringe Analysis," Final Tech. Rep't., Contract DAJA 37-81-C-0251, Max Planck Inst. für Strömungsforschung, Göttingen, W. Germany, 1986.

4. Doligalski, T. and Walker, J., "The Boundary Layer Induced by a Convected Vortex," Jour. Fl. Mech., Vol. 139, p. 1-28, 1984.

5. Fujii, K. and Kutler, P., "Numerical Simulation of the Viscous Flow Over Three-dimensional Complicated Geometries," AIAA Paper 84-1550, 1984.

6. Srinivasan, G. and McCroskey, W., "Numerical Simulations of Unsteady Airfoil-Vortex Interactions," Vertica, Vol. 11, No. 1/2, P. 3-28, 1987.

7. Mandella, M. and Bershader, D., 1987: see reference 6 on page 28 of main proposal.

8. Srinivasan, G., McCroskey, W., and Baeder, J., "Aerodynamics of Two-Dimensional Blade-Vortex Interaction," AIAA Jour., Vol. 24, No. 10, p. 1569-1576, 1986.

9. Caradonna, F., Laub, G., and Tung, C., "An Experimental Investigation of the Parallel Blade-Vortex Interaction," Paper 4, Tenth European Rotorcraft Forum, The Hague, Netherlands, 1984.

10. Strawn, R. and Caradonna, F., "Conservative Full-Potential Model for Unsteady Transonic Rotor Flows," AIAA Jour., Vol. 25, No. 2, p. 193-198, 1987.

11. Strawn, R. and Tung, C., "The Prediction of Transonic Loading on Advancing Helicopter Rotors," NASA Tech. Mem. 88238, USAVSCOM, 1986.

12. Tung, C. and Chang, I., "Rotor Transonic Computation with Wake Effect," Fourth Internat. Conf. on Applied Numerical Modeling, Paper D-23, Taiwan, 1984.

13. Kaykayoglu, R. and Rockwell, D., "Vortices Incident Upon a Leading Edge: Instantaneous Pressure Fields," Jour. Fl. Mech., Vol. 156, p. 439-461, 1985.

14. Moore, D., "The Effect of Compressibility on the Speed of Propagation of a a Vortex Ring," Proc. Royal Soc. London, A 397, p. 87-97, 1985.

15. Bershader, D., "Shock Tube Studies of Vortex Structure and Behavior," Proceedings of the 16th International Symposium on Shock Tubes and Waves, VCH Verlagsgesellschaft, Aachen, W. Germany, 1987, (in press).

16. Yang, J., Lombard, C., and Bershader, D., "Numerical Simulation of Transient Inviscid Gas Flows in a Shock Tube," AIAA Jour., Vol. 25, No. 2, p. 245-251, 1987.

17. Yee, H., "Upwind and Symmetric Shock-Capturing Schemes," NASA Tech. Mem. 89464, May, 1987.

END
FiLMED
9/88
DTIC